From microstructure to subsurface characterization. Spectral information from field scale time domain induced polarization.

Johansson, Sara

2016

Document Version:
Publisher's PDF, also known as Version of record

From microstructure to subsurface characterization

Spectral information from field scale time domain induced polarization

Licentiate Thesis

Sara Johansson
Division of Engineering Geology
Lund University
Sweden

ISBN 978-91-7623-673-4 (print)
ISSN 978-91-7623-674-1 (pdf)
ISRN LUTVDG/(TVTG-1036)/1-99/(2016)

2016-01-26

LUND
UNIVERSITY

Abstract

A large variety of subsurface infrastructure projects of different types can gain valuable information from tomographic measurements of subsurface physical properties. With resistivity and time domain spectral induced polarization (IP), the distributions of the conductive and capacitive properties of the subsurface are obtained. Technical developments of time domain IP equipment and new inversion algorithms have led to the possibility of collecting large amounts of data and invert for spectral IP parameters. In this way, much more information about the subsurface can be extracted from a single measurement compared to what was possible previously. It is well-known that spectral IP effects arise through redistribution of ions at the pore scale, and that spectral IP parameters can be linked to microscale surface chemical and structural properties. However, much remains to be known about how to analyse and interpret spectral IP parameters from field scale time domain IP measurements. Therefore, the main objective of this licentiate thesis is to focus on these issues.

In soils contaminated with free phase non-aqueous phase liquids (NAPLs), the contaminant phase affects the microgeometry inside the pore spaces of the soil. The results from paper I show that different configurations of the NAPL phase likely affect the spectral IP response of the soil in different ways. This is exemplified by measurements at a field site, where IP responses are absent in the NAPL source zone. In contrast, elevated IP responses are observed in the degradation zone, where the NAPL probably is configured as isolated droplets in the pore space. In order to investigate probable sources to observed varying IP responses in a Cretaceous limestone bedrock, the measured spectral IP parameters were compared with the investigations of the microstructure and composition of thin sections in paper II. Several characteristics that can affect the measurements were found, such as presence of certain minerals and varying texture of the limestone. However, more research is needed in order to understand the polarization mechanisms in limestones. Although most previous research has been carried out in sand- and claystones, there is a great potential to reveal textural and structural properties in any kind of bedrock by measurements of spectral IP parameters.

Sammanfattning

Många olika sorters underjordiska infrastrukturprojekt kan gagnas av den värdefulla information som tomografiska mätningar av markens fysiska egenskaper kan ge. Resistivitet och tidsdomän spektral inducerad polarisation (IP) ger en bild över markens distribution av konduktiva och kapacitiva egenskaper. Teknisk utveckling av mätutrustning för tidsdomän IP och nya inversionsalgoritmer har medfört möjligheter till att samla in stora datamängder och invertera för spektrala IP parametrar. På detta sätt kan mycket mer information om marken utvinnas från en och samma mätning, jämfört med vad som varit möjligt tidigare. Det är välkänt att spektrala IP effekter uppstår genom omfördelning av joner på porskalenivå, och att spektrala IP parametrar kan kopplas samman med ytkemiska och strukturella egenskaper på mikroskala. Dock behövs forskning om hur spektrala IP parametrar från fältskaleundersökningar med tidsdomän IP bör analyseras och tolkas. Det huvudsakliga målet med denna licentiatavhandling är därför att fokusera på dessa problem.

I non-aqueous phase liquids (NAPL) förorenade jordar påverkar föroreningsfasen mikrogeometrin i jordens porsystem. Resultaten från artikel I visar att olika konfigurationer av NAPL-fasen sannolikt påverkar den spektrala IP-responsen i jorden på olika sätt. Som exempel på detta förekom inga IP responser i källzonen på en undersökt fältlokal. Dock observerades förhöjda IP responser i nedbrytningszonen, där NAPL-fasen sannolikt är distribuerad som isolerade droppar i porsystemet. För att undersöka sannolika källor till de varierande IP responser som observerades i en kalkstensberggrund kombinerades de uppmätta spektrala IP parametrarna med undersökningar av mikrostrukturen och sammansättningen i tunnslip i artikel II. Flera egenskaper som kan påverka mätningarna identifierades, t.ex. förekomst av vissa mineraler och varierande textur i kalkstenen. Dock krävs mer forskning för att förstå hur polariseringsmekanismerna fungerar i kalkstenar. Trots att mycket forskning har fokuserat på sand- och lerstenar finns det en stor potential att mätningar av spektrala IP parametrar kan användas för att undersöka textur och strukturella egenskaper i alla sorts bergarter.

Preface

This project is part of the Geoinfra-TRUST framework (http://trust-geoinfra.se/). Funding for the work was provided by Formas - The Swedish Research Council for Environment, Agricultural Sciences and Spatial Planning, (ref. 2012-1931), BeFo - Swedish Rock Engineering Research Foundation, (ref. 331), SBUF - The Development Fund of the Swedish Construction Industry, (ref. 12719) and Sven Tyréns Stiftelse.

I would like to thank my main supervisor Torleif Dahlin and my assisting supervisors Charlotte Sparrenbom and Håkan Rosqvist for all help, support and commitment during this work.

A special thanks also to Gianluca Fiandaca for great collaboration, your help and dedication as well as many rewarding discussions.

I am also grateful to Johan Lindgren and Leif Johansson for teaching me how to prepare thin sections and use the Scanning Electrone Microscope.

I would like to thank my fellow PhD students at Engineering Geology for interesting and enjoyable collaborations and discussions, and for a friendly and supportive working environment.

Thank you Mats Svensson for encouraging me to initiate my PhD studies.

Last but not least, thanks to all current and former colleagues and collaboration partners at Lund University and Tyréns, my family and friends for cheering me on.

List of appended papers

Sara Johansson has performed the major parts of the data analysis, interpretation and writing of papers I and II. The survey designs and field work were planned and performed as group activities. The data processing and inversions were made by Sara Johansson with help from Gianluca Fiandaca. The analyses of thin sections were made by Sara Johansson with help from Charlotte Sparrenbom and Anders Lindskog.

Paper I

Johansson, S., Fiandaca, G. and Dahlin, T.

Influence of non-aqueous phase liquid configuration on induced polarization parameters: Conceptual models applied to a time-domain field case study.

Special issue: Advances in IP, Journal of Applied Geophysics, Volume 123, December 2015, Pages 295–309

Paper II

Johansson, S., Sparrenbom, C., Fiandaca, G., Lindskog, A., Olsson P.I, Dahlin, T. and Rosqvist, H.

Investigations of a Cretaceous limestone with spectral induced polarization and scanning electron microscopy

Submitted for publication (Geophysical Journal International)

Contents

Chapter 1: Introduction

In many different kinds of infrastructure projects, there is a need to obtain an image of the underground. Knowledge of rock properties are for example important during the planning of underground construction of tunnels, when questions about e.g. mechanical stability and risk of ground water flow arise. Other infrastructure projects deal with remediation of contaminated soils and search for methods to image extensions of contaminant plumes or the success of in situ remediation efforts. Drilling is a well-established method where detailed point information about the subsurface can be obtained, but there is a risk of missing important information in between the boreholes. Infrastructure projects often gain a better view of the investigated ground when drilling is combined with geophysical methods. Depending on the geophysical methods used, the variations in subsurface physical properties can often be linked to variations in geological or groundwater chemical properties. Whether the infrastructure project deals with geotechnical, environmental or other issues, most fields working with soils, rocks and groundwater can benefit from knowledge that geophysical methods can provide.

Among physical properties of geological materials, electrical resistivity is the property that varies the most. The resistivity of earth materials vary from less than 1 Ωm (e.g. magnetite ores, certain clays) to more than 10^8 Ωm (e.g. marble and quartzite). The variations in resistivity are however large within each soil or rock type, which means that there is a large overlap in the resistivity range between different materials, and thus, it is not always possible to discriminate between them with resistivity alone.

To enhance the possibilities to discriminate between different materials or structures in the subsurface, the Induced Polarization (IP) effect can be measured simultaneously with the resistivity measurements. The IP effect is a measure of the ability of the soil to become polarized under the influence of an electric field, and the polarization properties of geological materials differ from the conductive properties measured with resistivity. During the polarization, energy is stored in the soil and one can make the analogy between electric

potential energy (as stored kinetic energy) (Marshall & Madden 1959; Powers 1997). In time domain, the decay of the potential after the current interruption corresponds to the conversion of the stored energy back to electrical energy. It is known that the IP effect has a dispersive nature, meaning that the amount of polarization of the soil varies with the frequency (or time duration) of the injected current.

The existence of the IP effect has been known since the early 1900s, when it was discovered that sulfide mineralization gave rise to remnant potentials in the subsurface after the interruption of the transmitted current. Later, it was observed that many other geological materials also give rise to similar effects, however often weaker in magnitude. Although IP measurements early on were mostly used for mineral prospecting, they have more recently been applied for a wider range of investigations including landfill investigation (e.g. Dahlin et al. 2010), rock quality assessment (e.g. Magnusson et al. 2010) and estimations of hydraulic conductivity (e.g. Slater & Lesmes 2002).

The mechanisms behind the IP effect and its spectral behavior are not yet fully understood, which limits the interpretational possibilities of the method. A lot of research has been carried out in the laboratory in order to connect the IP signals to material properties. This research is mainly carried out in the frequency domain, and the samples are often carefully and homogeneously prepared. In this way, it has been possible to relate the spectral IP response to a range of different petrophysical and chemical properties in the samples. The laboratory research has also served as a basis for some physical understanding about and modelling of different physical mechanisms behind the observed IP effect.

In the field, time domain measurements have a number of practical advantages over frequency domain measurements; they are more time efficient, robust and already common as pre-investigation methods in industry (Dahlin & Leroux 2012). However, in terms of interpretation of subsurface IP responses it is not straight forward to move from the relationships established with frequency domain laboratory measurements to time domain field results.

1.1 Motivation and Aim

This licentiate thesis has been carried out under the TRUST project (Transparent Underground Structure, http://trust-geoinfra.se), which is a large

geotechnical R&D project in Sweden comprising partners from both academia and industry. The main aim of the sub-project *TRUST 2.1 – Geoelectrical Imaging for Site Investigations for Urban Underground Structure* is to adapt the DCIP instrumentation, data collection, processing and inversion methods to more robust and efficient imaging in technically challenging urban environments.

New inversion algorithms, which enable extraction of a considerably larger amount of information from time domain decay curves compared to previously are emerging. In the TRUST 2.1 project, the AarhusInv software is developed, which inverts for the shape of the decay curves instead of the integral chargeability. The advantages with this approach are several, some of the most important being:

1. The possibility to extract spectral information from the IP decays
2. Inverted chargeability which is less dependent upon measurement settings
3. Enhanced possibility to compare between IP data collected in time- and frequency domain

Collection of large quantities of good quality data is however not enough in order to increase the applicability of the method in infrastructure projects; the extracted physical properties need to be interpretable in order to be useful. The main aim of this PhD project is therefore to increase the understanding of how to interpret inverted spectral IP parameters. Previous research has shown that spectral IP mechanisms are related to microgeometrical surface properties in the ground in contrast to resistivity which is a bulk parameter. Inverted spectral IP parameters therefore have a great potential for revealing information that cannot be obtained with resistivity alone.

The main objective of this work lies in connecting resistivity and spectral IP parameters to variations in geotechnical and environmental properties of the subsurface. The best way to move in this direction is to increase the overall physical understanding of spectral IP; without such an understanding of the signals, the results from one site might not be applicable to another. As a starting point, the knowledge of spectral IP behavior obtained from the laboratory should be transferred to field scale time domain IP to the largest possible degree. The main problem herein lies in the scale and the heterogeneity of most geological materials - most quantitative research has been done on homogeneous granular samples that rarely occur in the field.

Since the IP effects occur at the microscale, the microgeometry of the natural subsurface is important to consider.

Although a lot of experience, empirical relationships and physical understanding about IP spectra can be derived from the results of laboratory studies, there is still a general lack of understanding about the spectral IP responses of composite and heterogeneous geological materials. For example, more research is needed on:

1. The effect of micro- and macrogeometrical heterogeneities on the spectral IP response
2. Increased understanding of high-frequency polarization mechanisms (i.e. the Maxwell-Wagner effect)
3. Understanding of spectral IP responses caused by the superposition of different IP mechanisms

All of the above mentioned research questions are related to each other and important to consider when spectral IP parameters from field data are to be interpreted. However, all of these research needs cannot be met here.

1.2 Objectives

The first objective of this licentiate thesis is to achieve an understanding of the physical mechanisms governing spectral induced polarization based on previous research. The second objective is to investigate how to analyze spectral induced polarization parameters from field scale time domain IP measurements. More specifically, the objective is to investigate if the distribution of contaminants in soils can be imaged with time domain spectral IP, exemplified by free phase dense non-aqueous phase liquids (DNAPLs). Furthermore, if spectral IP parameters can be used to obtain information of varying bedrock properties.

1.3 Limitations and Outline

The overall methodology of this PhD project is to work on different scales and with different techniques (e.g. both spectral time and frequency domain IP, together with analysis of soil and rock samples with methods used in other

research fields). The limitations of the work carried out for the current licentiate thesis is to measure, process, invert and analyze field scale direct current resistivity and time domain induced polarization (DCIP) data, with the main focus on the data analysis. The data analysis include considerations of the quality and spectral content of time decays as well as theoretically supported interpretations with support in reliable conditions of microgeometrical properties. The types of investigated subsurfaces are limited to granular soil contaminated with non-aqueous phase liquids (paper I) and characterization of limestone bedrock (paper II). The former application is an area of large environmental significance and also an area where more research is needed (e.g. Kemna et al. 2012). Bedrock characterization (paper II) is also of interest in many environmental projects, and variations in limestone have not been extensively investigated with IP previously.

The outline of this Licentiate thesis is as follows: chapter 2 gives a background description of the IP parameters measured with different techniques, while models commonly used to extract spectral information from time- and frequency domain IP data are described in chapter 3. Chapter 4 gives a theoretical background on the current knowledge of physical IP mechanisms, and previous research and common applications are briefly described in chapter 5. The methodologies used in the work carried out in this thesis will be presented in chapter 6, while the main results are summarized in chapter 7. Chapter 8 contain discussions and conclusions of the work carried out as well as an outlook on planned future research.

Chapter 2: Induced Polarization Measurements and Parameters

The IP measurements performed in this licentiate thesis have been carried out in the time domain. However, a lot of previous knowledge about IP interpretation has been gained with frequency domain complex resistivity measurements (also referred to as spectral induced polarization measurements). Therefore, both techniques and the respective measured IP parameters are described in this chapter.

2.1 Time-domain Induced Polarization

Time-domain induced polarization (TDIP) is measured during the transmission of current pulses into the ground. A typical current waveform is shown in Figure 1.1., consisting of a cycle of square waves with alternating polarity and separated by current off times. Also shown in Figure 1.1. is the potential reading in one of the measurement channels. Apparently it takes a certain time for the potential to reach its maximum value during the current transmission. Likewise it also takes time for the potential to drop to zero after the interruption of the current transmission. This charge and discharge behavior of the ground is the basis for TDIP measurements.

While the resistivity is calculated from the maximum potential reading during the transmission of the current pulses, TDIP is a measure of how the potential declines after the current pulse has been interrupted. Figure 1.2 show a typical potential decay curve. Immediately after the current has been switched off, the

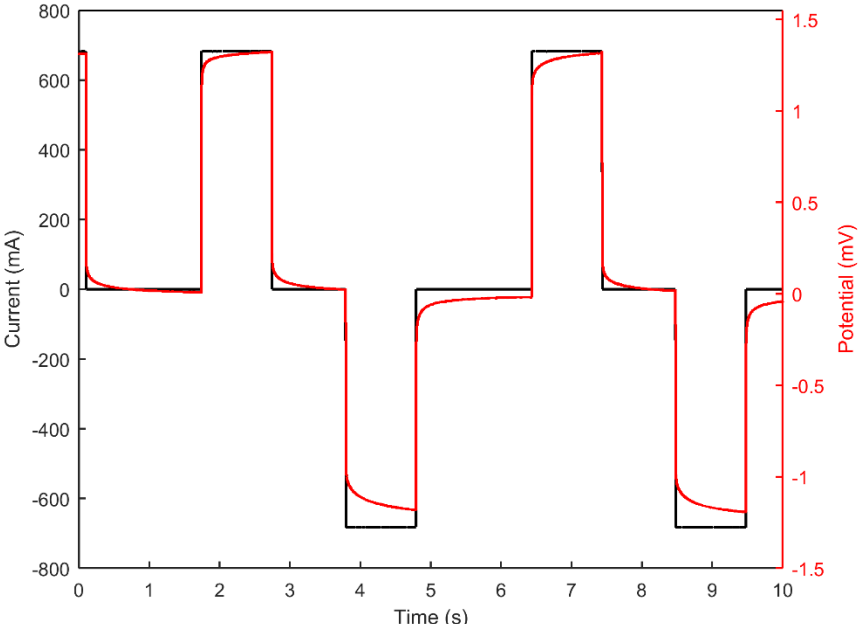

Figure 1.1. Typical current waveform (black) and potential response (red) in TDIP measurements.

potential drops to a so-called secondary response level, thereafter the shape of the potential decay curve is generally logarithmic (Sumner 1976).

The traditional measure of TDIP is a parameter called chargeability. The intrinsic chargeability was defined by Seigel (1959) as the magnitude of the secondary potential V_s to the primary potential V_p of the transmitted current wave:

Intrinsic chargeability $$m_0 = \frac{V_s}{V_p} \qquad (1.1)$$

Due to practical difficulties in measuring V_s immediately after the current interruption, the chargeability has traditionally been calculated through integration of the area beneath the decay curve during a defined time window:

Integral chargeability $$m_i = \frac{1}{t_2 - t_1} \int_{t_1}^{t_2} \frac{V_t}{V_p} dt \qquad (1.2)$$

where V_t is the potential reading at time t.

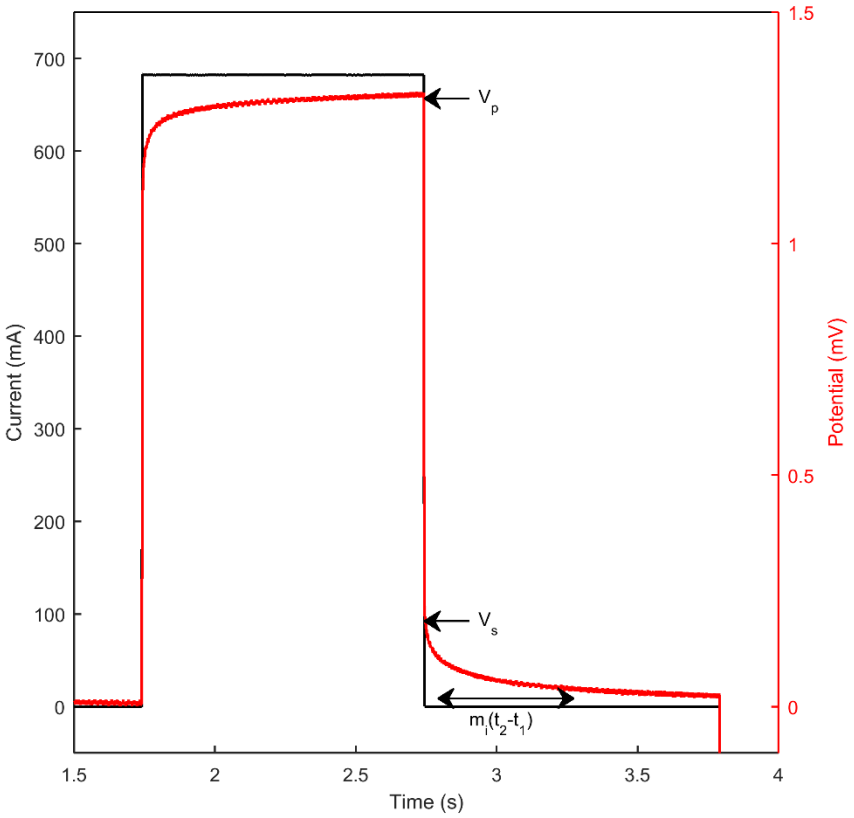

Figure 1.2. Illustration of the measures used to calculate the intrinsic or integral chargeability.

In practice, a discrete integration method is used with potential readings recorded in logarithmically spaced time gates (Sumner 1976). Both the gating and the duration of the current pulses and off times have an important and inevitable effect on the magnitude of the integral chargeability. It is therefore often ambiguous to compare chargeability values between different materials in a similar manner as for example electrical resistivity. While resistivity is a material parameter, integral chargeability is highly dependent on measurement settings.

2.2 Complex Resistivity

Like DCIP, complex resistivity (CR) is a geophysical method used to measure the response of geological materials to transmitted electric. The main difference between the two methods is that the CR method works in the frequency domain. Instead of using square wave current pulses, a continuous alternating current is transmitted to the sample during CR measurements. The potential over the sample is measured and the phase- and amplitude shifts between the transmitted current and the received potential sinusoids are calculated (Figure 1.3). The alternating current frequency is swept through a range of frequencies, typically between at least 0.1-100Hz, resulting in spectra of amplitude- and phase values (Butler 2005; Sumner 1976).

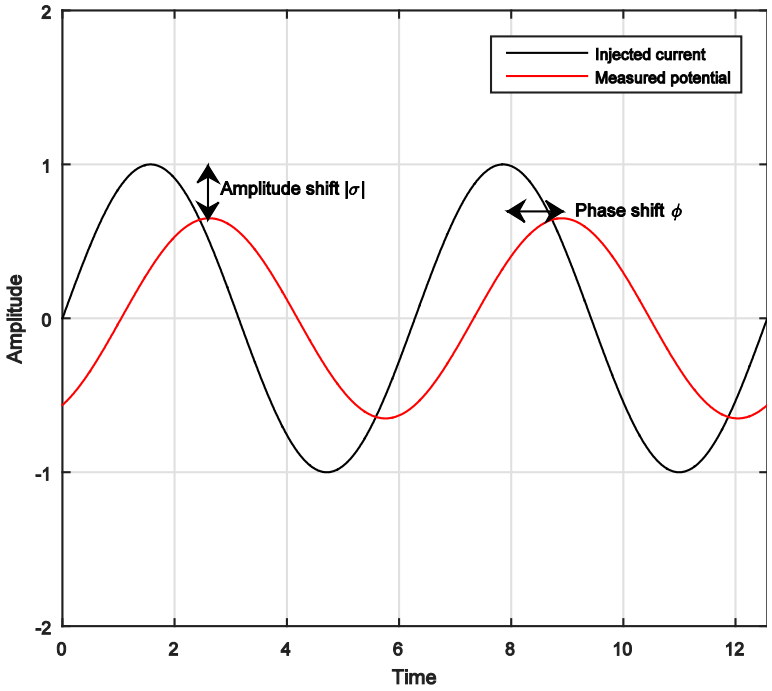

Figure 1.3. Illustration of the injected current and received potential in CR measurements and the extracted parameters.

In polar coordinates, the total complex resistivity ρ^* can be expressed as:

Complex resistivity $$\rho^* = |\rho|e^{i\varphi} \quad (1.3)$$

where $|\rho|$ is the magnitude of the amplitude and φ is the phase angle. In the literature, it is more common to express the measured complex quantity in terms of conductivity σ^* rather than resistivity ρ^*. From now on, this notation will therefore be used here also. For reasons that will become clear in the following chapters, it is often useful to express the complex conductivity in terms of the real (σ') and imaginary (σ'') components respectively:

Complex conductivity $$\sigma^* = |\sigma|e^{i\varphi} = \sigma' + i\sigma'' \quad (1.4)$$

The real component is in-phase while the imaginary component is out-of-phase with the current waveform. The relationship between the measured parameters $|\sigma|$ and φ and the computable parameters σ' and σ'' is therefore of mathematical nature. The relationships can be written as:

Phase $$\varphi = tan^{-1}(\frac{\sigma''}{\sigma'}) \quad (1.5a)$$

Amplitude $$|\sigma| = \sqrt{(\sigma')^2 + (\sigma'')^2} \quad (1.5b)$$

That is, the complex conductivity parameters φ and $|\sigma|$ are functions of both the real and imaginary components of the complex conductivity.

2.3 Electromagnetic interaction and normalized IP parameters

When a current is transmitted into the ground, an electromagnetic field is created which interacts with the media according to the electromagnetic theory. The relevant material properties for the interaction are the conductivity σ, the dielectric permittivity ε and the magnetic permeability μ. The magnetic permeability is mainly relevant when ferromagnetic minerals or materials are present in the soil (Butler 2005). Examples of ferromagnetic geological materials are pyrite (FeS_2) and magnetite (Fe_3O_4). Although most geologic materials are non-ferromagnetic and therefore do not have a significant magnetic permeability, all soils exhibit both conductive and dielectric behavior (Butler 2005).

The dielectric permittivity can be described as the ability of the material to become polarized in response to an electric field. Charges in the soil, which are not able to move freely, still react to an alternating electric field by displacing themselves in any way possible from their equilibrium positions. The charge displacements store energy from the electric field into the medium (Powers 1997; Butler 2005; Marshall & Madden 1959).

Since both the conductivity and the dielectric permittivity control motions of charges back and forth under the influence of a time varying electric field, it is not possible to only measure one of them from the total current density in the soil. The complex conductivity and the complex permittivity are two different measures of the same property. The measured complex conductivity will contain some influence of bound charges, while the measured complex permittivity will be affected by free charges. This means that whether in time domain or in frequency domain, the measured resistivity and induced polarization are influenced by both conductive and dielectric properties of the soil.

In most geological media, the dielectric effects are small in comparison to the conductive and can therefore often be neglected during resistivity or conductivity measurements. The dielectric properties of the soil are, in contrast, often significantly influenced by the bulk conductivity of the soil. The bulk conductivity is a sum of the real valued ionic conductivity of the groundwater, the complex surface conductivity along interconnected particle surfaces and electronic conduction inside the grains.

Normalization of the chargeability or phase values with the measured conductivity yields the so called normalized IP parameters, which in many cases are useful approximations of pure polarization properties of the soil (Slater & Lesmes 2002b):

Normalized phase angle $$\sigma'' = \varphi \cdot \sigma' \qquad (1.6a)$$

Normalized chargeability $$MN = \frac{m_i}{\rho} \qquad (1.6b)$$

When the normalized IP parameters are used, it is assumed that the bulk conductivity is mainly made up of ionic conduction in the groundwater (i.e. that the contributions from surface conductivity and electronic conductivity are small) (Slater & Lesmes, 2002b). This assumption is valid for metal-free soils where electronic conduction in solid material is negligible. Most geologic materials are insulators, except e.g. metallic minerals such as pyrite and magnetite. Generally, the contribution of the electronic conduction to the

electric conductivity of the soil becomes more important for low-porosity rocks, where the contribution from the ionic and surface conductions are small (Butler, 2005).

2.4 IP spectra and time decays

A physical basis for spectral IP is that different polarization processes in the soil take different amount of time to arise and decay. When the current is sent through the soil, charges start to move in accordance to the applied electric field. Therefore, it takes some time before the maximum potential is reached during the charging period. When the current is turned off (or the polarity is switched in frequency domain) the process is reversed and the charges start to return to their original positions. The reversed process takes an equal amount of time to occur, which means that the charge and discharge (decay) curves are inverses of each other, at least theoretically. In other words, the polarization of the soil is theoretically a linear process, which means that Fourier transformation can be used to convert time domain IP data to frequency domain IP data and vice versa (Powers 1997; Sumner 1976). In time domain measurements, settings such as sampling rate and time duration of the current pulses affect how much spectral information is actually recorded (Kemna 2000; Van Voorhis et al. 1973). Time domain data corresponding to the fundamental frequency and harmonics of the square wave can be translated to phase spectra via Fourier transform. The method is described in detail in Van Voorhis et al. (1973).

There are however some practical difficulties related to the comparison of phase- and chargeability measurements. The magnitude of the measured phase values are limited by the frequency range used in the spectral induced polarization (SIP) measurements, while the intrinsic chargeability in the time domain include the majority of the polarization response (Zonge et al. 1972). This could for example lead to an underestimation of the phase response if the main relaxation frequency is beyond the frequency range used in the measurements. In time domain, the underestimation of the intrinsic chargeability is most commonly caused by difficulties in gathering data from short times. It could also be caused by too short current pulses, since the time would then be too short for the low frequency polarization mechanism to occur.

Chapter 3: Phenomenological Models of IP spectra

Phenomenological models are equations that can be fitted to IP data in order to describe and parameterize the observed IP spectra or IP decays. These models are also used in inversion algorithms for extraction of spectral information from field data.

It has been argued that three main types of phase spectra have been observed in different SIP studies; spectra with a phase peak, nearly frequency independent phase spectra and spectra that increases with frequency (Titov et al. 2002). In addition, phase spectra with multiple phase peaks have also been reported (e.g. Nordsiek & Weller 2008). Several different kinds of models have been used to fit different kinds of IP spectra (see e.g. Dias 2000) and in this chapter, some of the most common phenomenological models in the literature are described.

3.1 The Debye and Cole-Cole models

The Debye equation describes the general behavior of the dielectric constant with a varying measurement frequency. The theory was developed for polar liquids, pictured as spheres in a viscous medium. The viscous medium represents molecular interactions that oppose the alignment of the dipoles according to the varying electric field. The frequency dependence of the dielectric constant is thus caused by the obstructed dipole polarization in this model. The complex dielectric constant ε^* in the Debye models is described as (Cole & Cole 1941):

Debye model $$\varepsilon^*(\omega) = \varepsilon_\infty + \frac{\varepsilon_0 - \varepsilon_\infty}{1 + i\omega\tau_0} \qquad (3.1)$$

where ε_∞ is the limiting (lower) value at high frequencies and $\varepsilon_0$is the limiting (higher) value at low frequencies. The measurement frequency is represented by ω, and τ_0 is a parameter called relaxation time. In the Debye theory, the relaxation time is proportional to the ratio between the macroscopic viscosity and the absolute temperature. This has the implication that the frequency range of the dispersion is low for solids (relatively high viscosity and large τ_0) and high for fluids. τ_0 is a measure of the time required for spherical dipoles to return to their original alignment after polarization. If the dipoles were assumed to be elliptical instead, three relaxation times would theoretically be obtained since the relaxation would occur along three axes (Cole & Cole 1941).

Cole & Cole (1941) observed that a broader frequency range of dispersion and adsorption could be seen in a wide range of experimental data, compared to what would be predicted from the Debye equation. As a result, they modified the Debye equation by adding the empirical exponent $(1-\alpha)$ to equation 3.1, which gives the model an arbitrary flatter appearance (Cole & Cole 1941):

Cole-Cole model $$\varepsilon^*(\omega) = \varepsilon_\infty + \frac{\varepsilon_0 - \varepsilon_\infty}{1+i\omega\tau_0{}^{1-\alpha}} \qquad (3.2)$$

The main difference between the Debye and the Cole-Cole model is that the Debye model represents the relaxation of a single particle size (in the above case a molecule). In contrast, the Cole-Cole model represents the relaxation of a range of sizes which broadens the spectra.

In the 1970s, Pelton et al. (1978) adopted the Cole-Cole model for complex resistivity data in frequency and time domain, introducing the intrinsic chargeability m_0 (equation 1.1) into the model (Pelton et al. 1978 and references therein):

Frequency domain Cole-Cole model

$$Z^*(\omega) = R_0\left[1 - m_0\left(1 - \frac{1}{1+(i\omega\tau)^c}\right)\right] \qquad (3.3)$$

where $Z^*(\omega)$ is the complex impedance (analogous to the complex dielectric constant) and R_0 is the DC resistivity. In this adoption of the Cole-Cole model, the exponent c (dimensionless, typically in the range between 0.1-0.6) is called the frequency dependence or the frequency factor. For a comparison between the Debye model and the Cole-Cole model with c =0.6, see Figure 3.1. The amplitude represent the real part of the complex impedance while the phase is the imaginary part. The time domain equivalent of the Cole-Cole model is given by (Pelton et al. 1978):

Time domain Cole-Cole model

$$V(t) = m_0 \frac{R_0}{I_0} \sum_{n=0}^{\infty} \frac{(-1)^n \left(\frac{t}{\tau}\right)^{nc}}{\Gamma(nc+1)} \qquad (3.4)$$

where $V(t)$ is the transient decay of the voltage after the disruption of the charging current I_0. In time domain, τ determines the length of time required for the main voltage decay. The effect of different relaxation times on the Cole-Cole model is plotted in Figure 3.2, in both time- and frequency domain.

In frequency domain, a single Cole-Cole model gives a symmetrical phase spectra where both sides of the peak have an equal slope (c and –c respectively). A variant of the Cole-Cole model, which gives an asymmetric phase peak, was presented in 1951 and is referred to as the Cole-Davidson model, see Figure 3.1. It can be seen that the slope of the Cole-Davidson model is similar to the Debye model on the left hand side, while it approaches the slope of a Cole-Cole model (with c=0.6) at the right hand side. Both the Cole-Cole and the Cole-Davidson variants were combined in the so-called generalized Cole-Cole model 1983, where an additional exponent (a) was added to the denominator (Nordsiek & Weller, 2008 and references therein):

Generalized Cole-Cole model

$$Z^*(\omega) = R_0 \left[1 - m_0 \left(1 - \frac{1}{(1+(i\omega\tau)^c)^a}\right)\right] \qquad (3.5)$$

The Debye, Cole-Cole and Cole-Davidson models all presume a single phase peak in the IP spectra. However, multiple phase peaks have in some cases been observed in previous research. Depending on the shape of the spectra, Pelton et al. (1978) fitted their phase spectra with one or several Cole-Cole relaxations. An example of a double Cole-Cole model is plotted in Figure 3.1. An approach that allows even more flexibilities in possible shapes of the spectra is the Debye decomposition. Here, the observed IP spectra are decomposed into a number of Debye spectra. The observed real and imaginary parts of the measured impedance $Z^*(\omega)$ are inverted in a process where values of chargeability are obtained from a predefined interval of relaxation times τ (Nordsiek & Weller 2008).

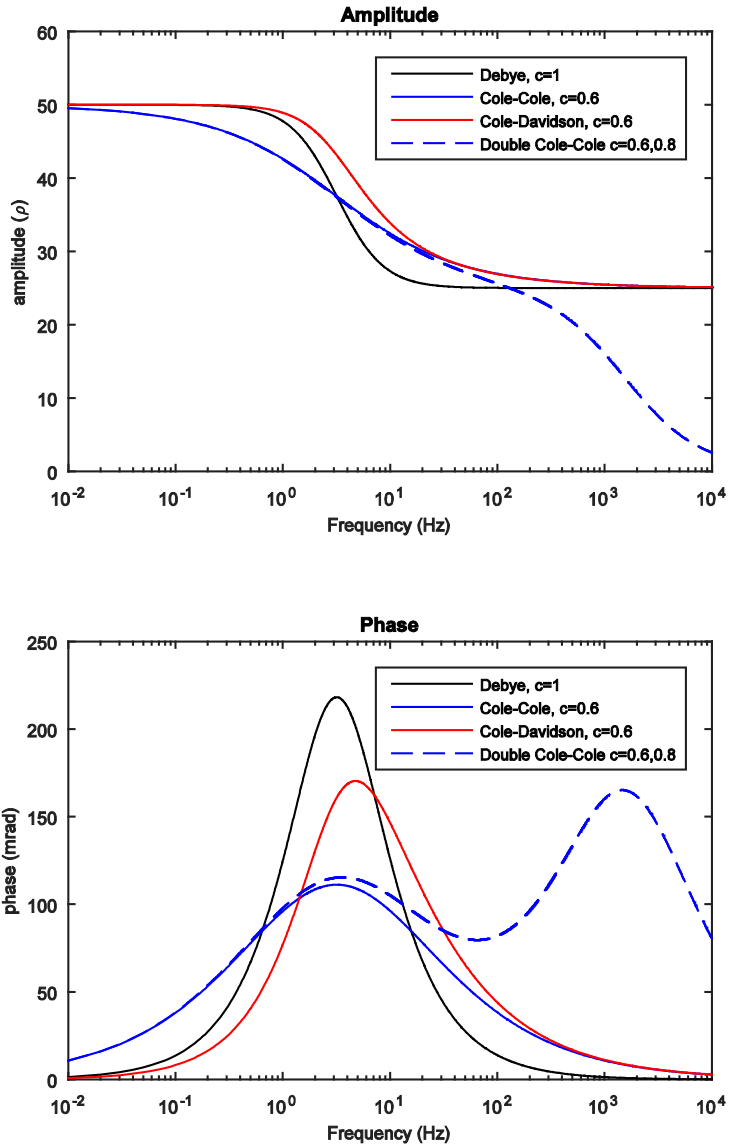

Figure 3.1. Comparison of common phenomenological models for IP spectra with phase peaks. $\boldsymbol{R_0}$=50Ω, $\boldsymbol{m}$=500mV/V and $\boldsymbol{\tau}$=0.05s.

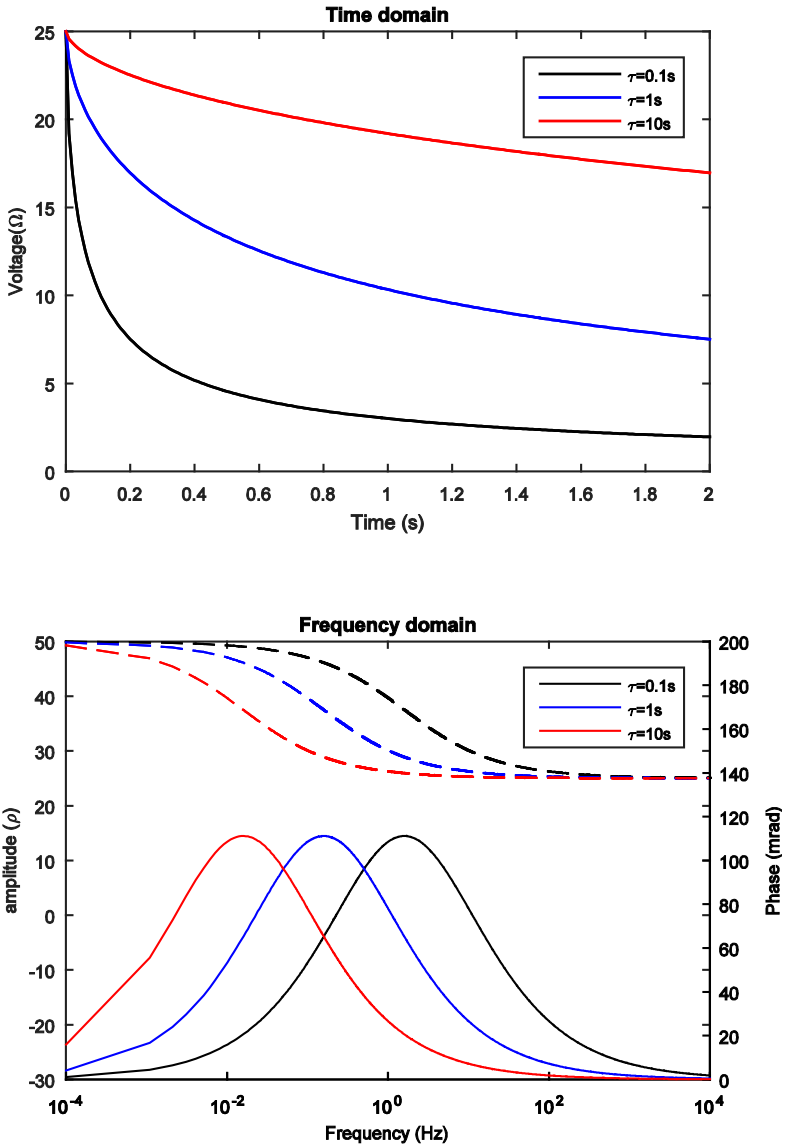

Figure 3.2. Variation of the Cole-Cole relaxation time in time domain (top) and frequency domain (bottom). In the bottom Figure, the dashed lines are the amplitudes and the solid lines are the phases. R_0=50Ω, m=500mV/V and c=0.6.

3.2 Constant phase angle models

Constant phase angle (CPA) models are based on the idea that there is no frequency dependence of the measured phase angle. Based on their experiences from measurement on mineralized copper porphyry rock, Van Voorhis el al. (1973) constructed an empirical model to describe the shapes of their spectra (other variants of CPA models have also been described in the literature, see e.g. Lesmes & Friedman (2005)). Van Voorhis et al. (1973) observed a decrease of the amplitude with increasing frequency, while the phase was essentially constant. This behavior was described by their so-called Drake model:

Drake model
$$\rho^*(\omega) = K(i\omega + \omega_l)^{-b} \qquad (3.6)$$

Where b is a positive fraction and K is an empirical constant. ω_l is a co-called low frequency pole, above which the phase spectrum is constant and the amplitude decreases. The positive fraction b determines the slope of the amplitude spectrum at frequencies above ω_l. The Drake model is plotted in Figure 3.3, where ω_l was set to 1Hz (for illustrative purposes. Generally, the low-frequency pole is set to much smaller values). At frequencies above ω_L, the phase is given by:

$$\varphi = -\frac{\pi}{2}b \qquad (3.7)$$

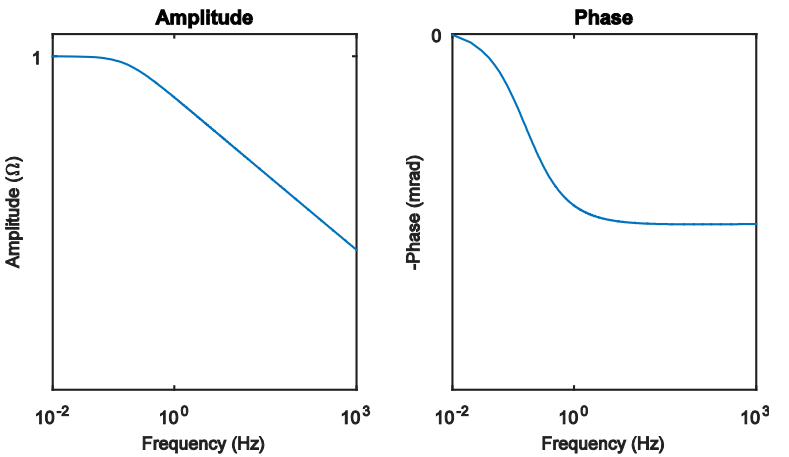

Figure 3.3. Illustration of the CPA model from Van Voorhis et al. (1973). ω_l=1Hz.

Chapter 4: Physical Mechanisms of Induced Polarization

As mentioned earlier, the IP effect is a measure of the ability of the soil to become polarized when charges are displaced from their equilibrium positions. In a fundamental way, spectral IP is equivalent to electrochemical dielectric spectroscopy. In the chemistry field, dielectric spectroscopy is often used to analyze the properties of different fluids and other materials in a broad frequency range (up to the MHz range). Depending on the frequency, the charge displacement takes place through different mechanisms; e.g. electronic polarization which means that the circular orbits of electrons becomes elliptical, or orientational polarization when dipole molecules with a net neutral charge rotate into alignment with the electric field. As the frequency of the electric field (AC current) increases, the dielectric permittivity generally decreases since some of the polarization processes do not reach their fully displaced positions before the field reverses (Powers 1997).

SIP measurements are low-frequency dielectric spectroscopy measurements. At the relatively low current frequencies (usually below 1kHz), most polarization processes in the soil are related to redistribution of ions. Conceptually, the buildup and relaxation of different polarization mechanisms in the soil take different amounts of time to occur. With high current frequencies, there may not be enough time for the slowest mechanisms to completely arise before the electric field reverses its direction. This is one of the reasons why the amount of polarization varies with different current frequencies, and a spectral behavior of the IP effect is observed.

The difficulties in explaining the IP-effect in geological materials originate in the heterogeneity of soils and rocks at the microscale where the polarization processes occur. Varying mineral composition, microgeometry, chemical environment etc. makes it more difficult to understand how the polarization mechanisms work in the soils and rocks compared to more homogeneous materials. The measured IP-parameters are also often results of superimposed

relaxations of several different polarization mechanisms occurring simultaneously in the soil. At present, there are four conceptual polarization mechanisms that can occur in the soil at the relevant frequencies, namely electrode polarization, membrane polarization, electrochemical polarization and interfacial (Maxwell-Wagner) polarization.

4.1 Electrode polarization

The electrode polarization mechanism is associated with conductive minerals in the soil (e.g. Sumner 1976; Ward 1988). When a conductive mineral is immersed into an electrolyte, its surface will become negatively charged. This will attract a fixed layer of positive counter ions in the electrolyte, called the Stern (or Helmholtz) layer (Figure 4.1). The ions in the fixed layer can be both electrostatically and/or chemically attracted. In addition, a second so-called diffuse layer is also formed by electrostatically attracted solvent ions. Both layers are collectively called the electrical double layer (EDL).

Two types of processes resulting in frequency dependent polarization can occur at the mineral-solution interface; faradic and non-faradic processes. The faradic processes are electrochemical redox reactions at the mineral-solution interface, i.e. electron transfer processes. Electron transfer between the minerals and the solution require that an energy barrier (reaction resistance) is crossed, which explains the impedance of the interface (Sumner 1976; Ward 1988). If the rate of redox reactions is high, the faradic processes are limited by the diffusion of ions to and from the mineral-electrolyte interface (Sumner 1976). When the rate of the redox reactions are limited, an excess of charge is found on the mineral surface (Bard & Faulkner 2001).

The faradic processes require the presence of active ion species in the electrolyte, which can take part in electrochemical redox reactions. Non-faradic processes involve non-active ions on the mineral surface. The non-faradic capacitance of the electrical double layer surrounding a mineral is directly comparable to a capacitor in an equivalent circuit. If no charge transfer occur, the two layers of charge can be compared to the two plates of a

capacitor, separated by an insulating media (Wong 1979; Bard & Faulkner 2001).

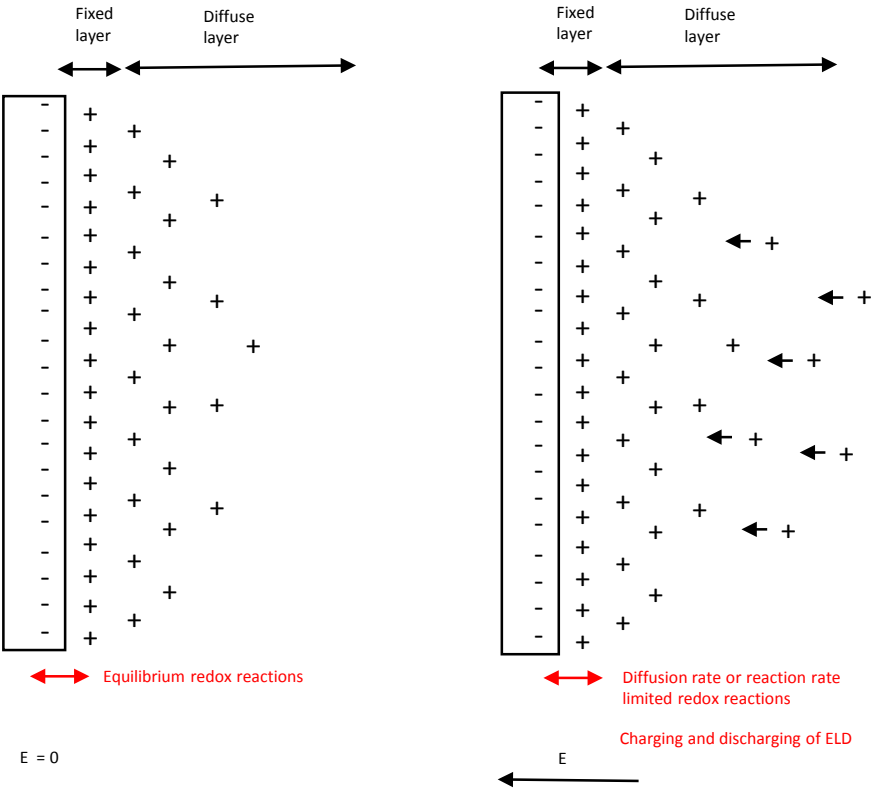

Figure 4.1. Conceptual sketch of the electrode polarization mechanism. The impedance of the metallic surface under the influence of an electric field arise due to unbalanced redox reactions and charging and discharging processes of the EDL.

The faradic processes and the EDLs around the minerals are in equilibrium when no electric field acts upon the soil (Sumner 1976). When an electric field is applied, ions in the electrolyte start to move and tend to accumulate at the surface of conductive minerals, since the different phases form a barrier for direct charge transport. The electrons in the mineral redistribute and balance the adsorbed excessive ions. With some faradic charge transfer between the mineral and the electrolyte, the system can be described as a “leaky” capacitor (Wong 1979). The capacitance is dependent on the rate of diffusion of active ions to and from the interface. While the impedance of a classical capacitor is

inversely proportional to the current frequency ($1/(i\omega)$), the impedance of the metal-electrolyte interface is, because of the diffusion dependence, instead proportional to $1/\sqrt{i\omega}$ (and referred to as the Warburg impedance). At very low frequencies, the impedance is large and the soil acts as an insulator. At high frequencies on the other hand, the soil acts as a conductor and the impedance is low (Wong 1979; Sumner 1976; Marshall & Madden 1959).

The processes described above contribute to the impedance at the conductive mineral-electrolyte interface in two different ways. The non-faradic path represents the charging and discharging of the EDL under the influence of an alternating current. The faradic path represents the charge transfer across the interface, and the impedance is dependent on the redox reaction and ion diffusion rates. At low frequencies, most of the current is carried by the faradic processes while the non-faradic processes are dominant at higher frequencies (Ward 1988).

4.2 Membrane polarization

The membrane polarization model was first described by Marshall & Madden in 1959 in order to analyze and account for the so-called background polarization effects, which could not be explained by presence of conductive minerals. The concept of the membrane mechanism is the existence of a series of ion selective zones in the ground, regularly interrupted by zones with no ion selectivity. Ion selective zones are passages in the pore system where cations can pass while anions are blocked or vice versa. These zones can consist of narrow pores or pore-throats mainly occupied by cations in the EDLs of the surrounding grains (e.g. Titov et al. 2002), or of negatively charged clay particles attracting a cloud of positive counter ions (e.g. Marshall & Madden 1959; Ward 1988). A conceptual sketch of the membrane polarization mechanism is shown in Figure 4.2, where the alternating series consist of narrow ion selective pore throats and wider non-selective pores.

When an electric field is applied to the system, anions are blocked in front of the ion-selective zones while the cation diffusion is enhanced (membrane blocking effect), leading to an alternating series of ion surplus and deficiency along the pore space. With clay particles in the pore system, the cations attached to these will be displaced according to the electric field (Marshall & Madden 1959; Vinegar & Waxman 1984; Sumner 1976).

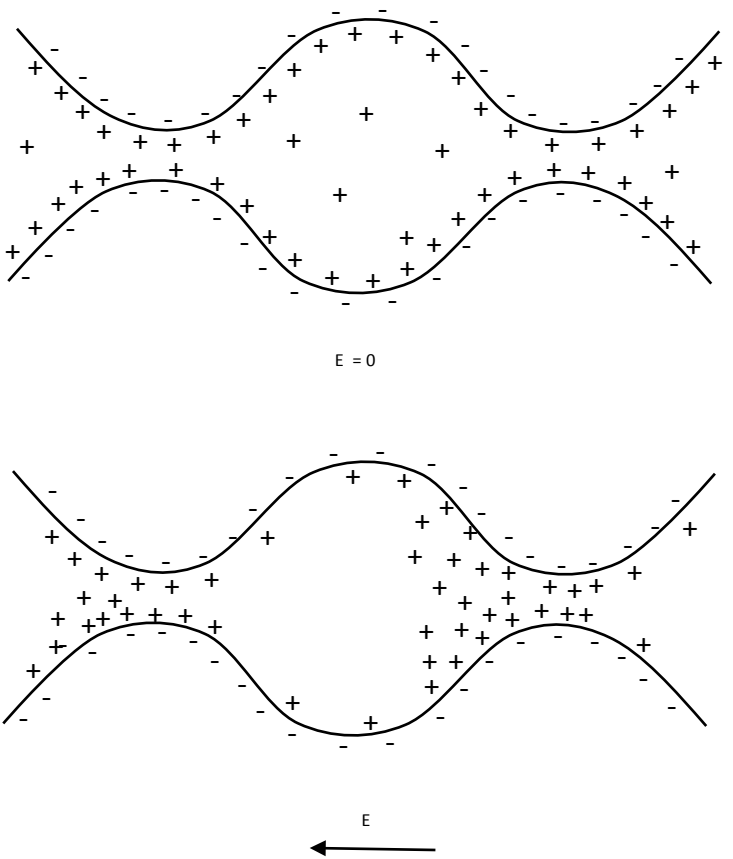

Figure 4.2. Conceptual sketch of the membrane polarization mechanism, where the ion selective zones consist of narrow pore throats. The mechanism leads to zones of ion surplus and ion deficiency around the narrow pores. Only cations are shown here for clarity.

The length ratio between ion selective and non-selective zones and the relative ion transparencies determine the amount of possible polarization. It is evident that if the ion selective zones occur too frequently, and essentially become continuous, no polarization will occur since no concentration gradient can develop without the non-selective zones. This situation can occur e.g. in very clay-rich shales (Sumner 1976; Marshall & Madden 1959; Vinegar & Waxman 1984; Titov et al. 2002).

The frequency dependence of the membrane polarization mechanism is diffusion controlled. The length of the ion selective and/or non-selective zones determines the length between the ion surplus and deficiency zones, and accordingly the relaxation times. According to Marshall & Madden (1959), the relaxation times are longer if the non-selective zones are longer than the selective zones. The relaxation time for a system similar to Figure 4.2 can be expressed as (Revil et al. 2012):

Membrane relaxation time $$\tau = \frac{r^2}{2D} \quad (4.1)$$

Where r is the characteristic pore size and D is the ion diffusion coefficient. According to (Titov et al. 2002), the peak relaxation time can be expressed as:

Membrane relaxation time $$\tau = \frac{l^2}{4D} \quad (4.2)$$

where l is the length of the selective zone. This is valid if the selective zone is much longer than the non-selective zone, an assumption referred to as the Short Narrow Pore (SNP) model (Titov et al. 2002; Titov et al. 2004). Regardless of whether it is the selective or non-selective zones that determines the relaxation time, the frequency dispersion increases with a large distribution of zone lengths (Marshall & Madden 1959; Vinegar & Waxman 1984).

4.3 Electrochemical polarization

Electrical double layers do not only form around conductive minerals immersed in an electrolyte; EDLs also form at the interfaces of electrically insulating minerals (e.g. silicates). When an electric field is applied to a geological media, the ions in the EDLs around the grains are redistributed. A conceptual sketch of the grain polarization principle is shown in Figure 4.3, where both the EDL around a grain becomes polarized under the influence of the electric field. The grain polarization model clearly has some mechanisms in common with the membrane polarization model, i.e. the displacement of counter ions attached to particle surfaces.

The electrochemical polarization mechanism can be divided between polarization of the fixed and diffuse layers respectively, since they react differently to an applied field. A theory for polarization of the fixed layer was developed by Schwarz (1962), who assumed that the ions could only move in a direction tangential to the grain surface. Surface conductivity along

interconnected grains via their electrical double layers was not taken into account in this model.

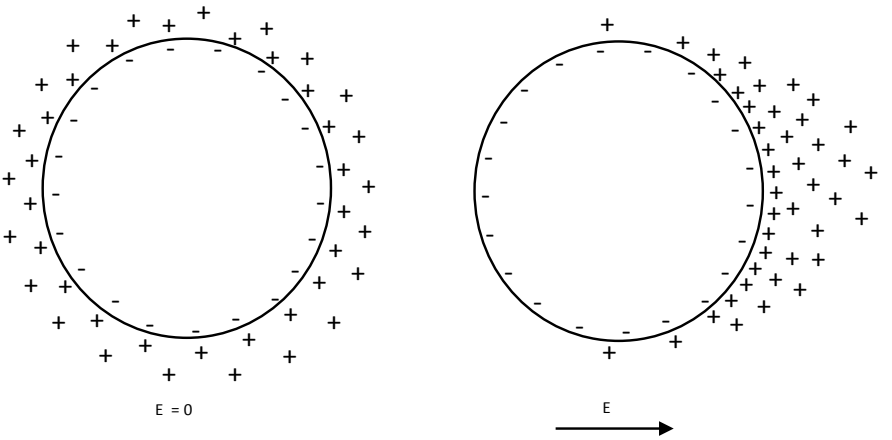

Figure 4.3. Conceptual sketch of the electrochemical polarization mechanism. Ions in the EDL are displaced under the influence of an electric field.

Later, both the fixed and diffuse layers were taken into account in models of the electrochemical polarization mechanism. The fixed layer polarization resulted in single Debye relaxation, while the diffuse layer showed a dispersion pattern more similar to a Cole-Cole relaxation. According to results of modelling, the fixed layer polarization is much stronger in magnitude than the diffuse layer polarization (de Lima & Sharma 1992; Lesmes & Morgan 2001). Polarization of the diffuse layer was later dismissed by Leroy et al. (2008) and Revil & Florsch (2010), who stated that the diffuse layer contributes to surface conductivity but not to polarization. The reason for the absent polarization is that the diffuse layers of the grains in a granular material are interconnected (Leroy et al. 2008; Revil & Florsch 2010).

In recent models, the mobility, ion densities and cation exchange capacities (CEC) in the fixed and diffuse layers are taken into account. The surface conduction is assumed to be dominated by the diffuse layer because of the low ion mobility in the Stern layer (Revil & Florsch 2010; Revil 2012).

The frequency dispersion of the electrochemical polarization mechanism is highly dependent on the grain size distribution. According to Revil & Florsch

(2010), the peak relaxation time $\tau\ (s)$ of the peak soil polarization is related to dominant particle size d_0:

Electrochemical relaxation time $$\tau = \frac{d_0^2}{8D} \quad (4.3)$$

where D is the diffusion coefficient of the ions. The frequency dispersion around the peak relaxation time is dependent on the grain size distribution; a wider distribution leads to a broader frequency dispersion.

4.4 Interfacial (Maxwell-Wagner) polarization

Maxwell-Wagner polarization is a mechanism that occurs at the interfaces between different materials in a composite material, and it is therefore also called interfacial polarization. A conceptual sketch of the mechanism in granular material is shown in Figure 4.4.

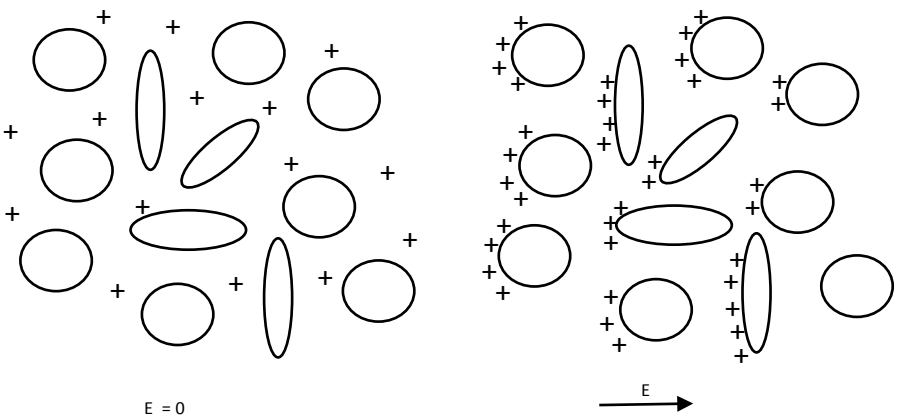

Figure 4.4. Conceptual sketch of the interfacial (Maxwell-Wagner) polarization mechanism.

Different materials can be characterized by their electrical conductivity (σ) and dielectric permittivity (ε). The ratio between these properties (ε/σ) is the relaxation time (τ), and the relaxation time describes the required time for excess charges to spread in the material. In a simple case, charge builds up at a linear interface between two materials with different relaxation times:

Maxwell-Wagner relaxation time $$\tau_{MW} = \frac{\varepsilon_1 K_1 + \varepsilon_2 K_2}{\sigma_1 K_1 + \sigma_2 K_2} \quad (4.4)$$

where ε_1, ε_2, σ_1 and σ_2 are the dielectric permittivities and electrical conductivities of the two materials. K_1 and K_2 are geometrical factors which describe the ratio between the surface area of the interface and the thickness of the materials. The Maxwell-Wagner polarization process is therefore described by a single relaxation time τ_{MW} which is not equal to the relaxation times of the different materials (Iwamoto 2012). The accumulated charge at the interface is, at steady-state conditions:

Interfacial charge $$Q_s = (\tau_1 - \tau_2) \cdot J \cdot S \quad (4.5)$$

Where τ_1 and τ_2 are the relaxation times of the materials, J (A/m^2) is the steady-state current density and S (m^2) is the interfacial surface area (Iwamoto 2012).

Equations for more complex geometries than the simple case in equations 4.4 and 4.5 have been developed. The classical Maxwell-Wagner treatment describes the complex dielectric response of small concentrations of isolated spherical particles suspended in a medium. For larger concentrations, the Bruggeman-Hanai equation is considered more appropriate. In both equations, the complex permittivity of the mixture is proportional to the complex permittivities and the relative volume fraction of the constituents (de Lima & Sharma 1992). The Bruggeman-Hanai equation was further developed by Sen et al. (1981) to incorporate Archie's cementation exponent m as a representation of particle shapes:

Complex permittivity $$\varepsilon^*(\omega) = \varepsilon_w^* \theta^m \left(\frac{1-\varepsilon_g^*/\varepsilon_w^*}{1-\varepsilon_g^*/\varepsilon} \right)^m \quad (4.6)$$

where ε_w^* and ε_g^* are the complex permittivities of the pore fluid and the grains, ε is the dielectric constant and θ is the volume fraction of pore fluid (Lesmes & Morgan 2001). At DC conditions, the Bruggeman-Hanai-Sen equation reduces to Archie's law (Sen et al. 1981; Lesmes & Morgan 2001):

Archie's law $$\sigma_{dc} = \sigma_w \theta^m \quad (4.7)$$

where σ_{dc} is the conductivity if the material and σ_w is the water conductivity.

Geometrical factors that affect Maxwell-Wagner polarization include for example existence of pore spaces isolated from the main conducting paths. The equations above assume that the pore space is interconnected, but existence of isolated pore spaces or pockets could give rise to higher dielectric permittivity at low frequencies (Sen et al. 1981). The Maxwell-Wagner polarization also appear to increase with small concentrations of grains with high aspect ratios in a host rock (Sen 1981).

The Maxwell-Wagner polarization mechanism arise due to intrinsic and geometrical properties of the geological material and is not dependent on surface electrochemistry. The two mechanisms are however superposed in geological media, and models that incorporate both interfacial and electrochemical polarization mechanisms have been developed (see de Lima & Sharma 1992; Lesmes & Morgan 2001; Leroy & Revil 2009).

Chapter 5: Previous Research and Applications

The aim of this chapter is to give a brief description of previous research findings and applications for IP. The objective is to obtain an overview of areas where more research is needed, and the chapter does not give a complete review of the research field.

The research ares have here been divided into four sections; conductive minerals, soils and sedimentary rocks, pore water properties and contaminated soil and microbiological processes. The main motivation for IP measurements on conductive minerals has been ore exploration. Many studies on the IP responses of granular soils and sedimentary rocks and pore water properties have been carried out with the objective to image hydrogeological information, for example hydraulic conductivity (see e.g. Slater & Lesmes (2002) for a review). Another common motivation of IP research has been to develop methods for characterization of contaminated soil.

5.1 Conductive minerals

It has been known for a long time that certain minerals e.g. graphite, magnetite, pyrrhotite, pyrolusite and many sulfides produce high IP effects when they are disseminated in a host rock (e.g. Pelton et al. 1978). These minerals have in common that they are electrically conductive; other minerals containing similar elements do not give rise to strong IP effects due to their low electrical conductivity (e.g. Bertin & Loeb 1976).

In rocks or soils containing conductive minerals, the main polarization mechanism is electrode polarization. The IP magnitude is dependent on the concentration of conductive minerals. The spectral behavior in ores is dependent on the amount, size and geometry of the conductive minerals. When

the mineralization occurs in veins and veinlets the observed relaxation times are generally very long. For discrete disseminated ores, the peak relaxation time is dependent on the grain size of the conductive minerals; large grain sizes leads to longer peak relaxation times, flatter spectra and decreased IP magnitudes compared to smaller grain sizes (Pelton et al. 1978; Wong 1979). Similar spectral IP behavior has been observed in sands containing conductive grains (Nordsiek & Weller 2008).

5.2 Soils and sedimentary rocks

Sands and sandstones have been studied a lot in previous research. Several relationships between IP spectra and petrophysical properties such as grain size distribution, specific surface area and pore throat size distribution have been found in the laboratory.

The amount of fine fractions (silt and clay) in a granular sample seems to play a significant role for the magnitude of the IP response; the IP magnitude generally increases with increasing amounts of fine fractions (Boadu & Owusu-Nimo 2010; Slater & Lesmes 2002a). Increasing clay content in sands and sandstones seem to play a particular role for observing high IP effects (Vinegar & Waxman 1984; Slater & Lesmes 2002a). The reason is believed to be that clays generally have high specific surface area, which enables higher surface charge densities per unit volume.

The spectral dispersion in granular materials is generally considered to depend on the characteristic length scales over which the charges polarize (Slater & Lesmes 2002a). The relaxation time is in a homogeneous granular material dependent on either the grain size distribution (e.g. Revil & Florsch 2010; Titov et al. 2002; Leroy et al. 2008) or the distribution of pore throats sizes (e.g. Scott & Barker 2003; Binley et al. 2005). Similar to the case with conductive minerals, increased length scales (grain diameter or pore throat size) leads to longer relaxation times. It has also been observed that wider grain- or pore throat distributions leads to flatter polarization peaks (i.e. lower values of Cole-Cole frequency exponent c) (Scott & Barker 2003).

The specific surface area of grains in relation to pore volume (S_{por}) is one of the most important petrophysical parameters determining the magnitude of the IP effect (Slater & Lesmes 2002; Weller & Slater 2015). Binley et al. (2005) and Zisser et al. (2010) observed shorter relaxation times with increasing S_{por}.

This was interpreted as an effect of the lower porosity in relation to the grain surface area leading to a greater number of small grains or pore throats being polarized. Similarly, Scott & Barker (2003) and Koch et al. (2011) observed that more densely packed grains seem to lead to shorter relaxation times, which could be an effect of smaller pore spaces compared to the conditions in more loosely packed grains.

Although increasing clay content in sands and sandstones tends to increase the IP response, research has shown that the IP responses of well-sorted clays usually are almost absent (Marshall & Madden 1959; Iliceto et al. 1982; Olhoeft 1985). Similarly, the studies by Iliceto et al. (1982) also indicated that the chargeability of well-sorted silt and loam was lower compared to the chargeability of natural sands. The absence of IP effects in clays were explained with the membrane polarization mechanism as a lack of zones with differing ion transparency (Marshall & Madden 1959). These conditions essentially leads to pure conduction along the grain surfaces without any ion displacements.

5.3 Pore water properties

Several studies have shown that the strength of the IP effect (chargeability or phase) decreases with increasing water content (e.g. Titov et al. 2004; Cassiani et al. 2009; Jougnot et al. 2010). In saturated samples, the main current path is via the electrolyte in the larger pores, meaning that the relative importance of the complex conductance through the EDL along the pore walls is relatively low. As the water saturation decreases and the larger pores drain, the relative importance of the complex conductance through the EDL becomes larger and the polarization increases (Titov et al. 2004). It can be presumed that the larger pore throats drain before the smaller ones, which has been reflected in the observation of shorter relaxation times with decreasing water saturation (Binley et al. 2005).

Normalized IP parameters seem to increase with groundwater salinity up to a certain point where after the magnitude starts to decrease with further increase in water conductivity (Vinegar & Waxman 1984; Lesmes & Frye 2001; Slater & Lesmes 2002a). The initial increase can be attributed to increasing surface charge density, while the decrease at higher pore water salinity might be an effect of reduced surface charge mobility (Lesmes & Frye 2001) or an

increased importance of the electrolytic (non-polarizable) conduction through the saline water (Scott & Barker 2003). While Scott & Barker (2003) observed a slight shift to shorter relaxation times, Vinegar & Waxman (1984) did not observe any strong frequency dependence with increasing water salinity.

5.4 Contaminated soil and microbiological processes

It is known that buried waste in landfills often produce large IP effects, and a number of studies have shown that chargeability or normalized chargeability mappings often are successful tools to delineate the waste body (e.g. Dahlin et al. 2010; Gazoty et al. 2012). Field IP measurements have also been performed with the aim to characterize soil contaminated with various kinds of substances, including BTEX and other hydrocarbons (e.g. Deceuster & Kaufmann 2012; Flores Orozco et al. 2012) or chlorinated solvents (e.g. Cardarelli & Di Filippo 2009). In the lab, several studies have dealt with the IP responses of contaminants such as e.g. oil or oil mixtures (Börner et al. 1993; Schmutz et al. 2010), waste- and motor oil (Vanhala 1997), gasoline (Martinho et al. 2006), octanol and benzene (Cassiani et al. 2009), toulene (Ustra et al. 2012), kerosene (Titov et al. 2004), ethanol (Personna et al. 2013) and trichloroethylene (Chambers et al. 2004). Many of the contaminants in the mentioned studies can be classified as non-aqueous phase liquids (NAPLs), which do not easily dissolve in water and often occupy the pore space as an own phase. There is no consensus on how NAPLs influence the measured IP response (Johansson et al. 2015) and more research is needed in this area (Kemna et al. 2012).

A complicating factor is that NAPL contaminated soils are subject to microbial degradation, which can lead to physical changes affecting the measurements. Microbial growth can lead to increased IP effects due to attachment of microbial cells around grains. It has been shown that EDLs forms around living cells which can affect the measured IP response (Atekwana & Slater 2009). Living or dead microbial cells can also change the pore geometry, for example by constriction of pores (Abdel Aal et al. 2006; Atekwana & Slater 2009). Furthermore, some bacterial activity involves precipitation of e.g. magnetite (Atekwana & Slater 2009) or calcite (Zhang et al. 2012). Microbial induced precipitation of sulfide minerals from the groundwater and corresponding measured increased IP effects have also been documented (Ntarlagiannis et al. 2005; Flores Orozco et al. 2011).

Chapter 6: Methods & Materials

As described in chapter 1, the aim of this work is to increase the understanding of spectral IP responses measured in the field. The overall methodology used in this licentiate thesis is to combine field scale DCIP measurements with microgeometrical studies, since IP effects are known to arise at the microscale regardless of the measurement scale used.

The DCIP data that have been analyzed in paper I and paper II were collected during the same field campaign (autumn 2013). The investigated site was selected since it is one of the worst PCE contaminated sites in Sweden, and the main objective was to investigate if the PCE contamination could be delineated with DCIP. Another objective was to characterize the soil- and bedrock conditions in the surrounding area to aid the risk assessment for polluted groundwater dispersal.

6.1 Time domain induced polarization measurements

The ABEM Terrameter LS was used to collect resistivity and time domain IP data along 2D sections with the cable and electrode layout shown in Figure 6.1. Separated cables for injecting current and measuring potential were used in order to reduce capacitive coupling effects (Dahlin & Leroux 2012). The extra cables were connected to the instrument via an external relay switch (ES10-64).

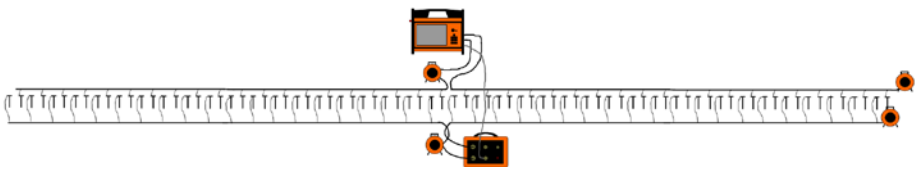

Figure 6.1. Separated cable layout used for the DCIP measurements.

To further reduce capacitive coupling and to increase the signal-to-noise ratio, low contact resistances between the electrodes and the ground were secured by a Focus One electrode contact test (Dahlin & Leroux 2012). When needed, the contact resistance was reduced by adding a starch-water mixture around the electrodes.

The pole-dipole electrode configuration was used in order to acquire data of both high spatial resolution and large depth penetration (Dahlin & Zhou 2004). The spacing between the electrodes was 2.5m, except in one case when a road was crossed and electrodes were excluded from the measurement protocol. Cables with 5m spacing between the 21 electrode take-outs were used. For the shorter measurement profiles (paper I), 42 electrodes or less (due to lack of space) were in use in the electrode spread. This corresponds to a maximum profile length of 102.5m and depth penetration of around 27.5m. In the longer measurement profiles (paper II), all 84 electrodes were in use which resulted in 207.5m long measurement profiles with a maximum depth penetration of approximately 75m. The on- and off-times of the current pulses were 1s long, and full waveform data was collected with a sampling rate of 1000Hz.

6.2 Data processing

Since the data was measured in an urban area, it was affected by noise. The main sources of periodic noise were power line and train traffic noise at frequencies of 50Hz and 16 2/3Hz. The periodic noise was reduced by using multiples of 60ms (equivalent to one period of 16 2/3 Hz and three periods of 50Hz) in the gating of the IP data. The delay time was 1ms and the gates were logarithmically spaced in between 0.07-0.97s.

Before inversions in AarhusInv, all decays were processed in Workbench. In Workbench it is possible to remove single IP gates and keep the remaining part of the decays. Typical bad IP gates are gates at early times, which may be affected by inductive coupling, or late times, which may be affected by electrode polarization effects. Examples of unprocessed decay curves are shown in Figure 6.2. A noise affected decay curve can be seen in Figure 6.2b, and a decay with too high values in the first gate is shown in Figure 6.2c. In Figure 6.2d, one of the decay curves becomes strongly negative at later times. In some cases, single gates in the middle of the decays were removed if the quality of the decay looked good for the rest. Negative IP decays (fig 6.2a)

were generally not regarded as bad data quality, since they may be caused by geometrical distribution of chargeable bodies in zones of negative sensitivity (Dahlin & Loke 2015). In some cases, there might also be physical mechanisms behind negative IP decays (Brandes & Acworth 2003).

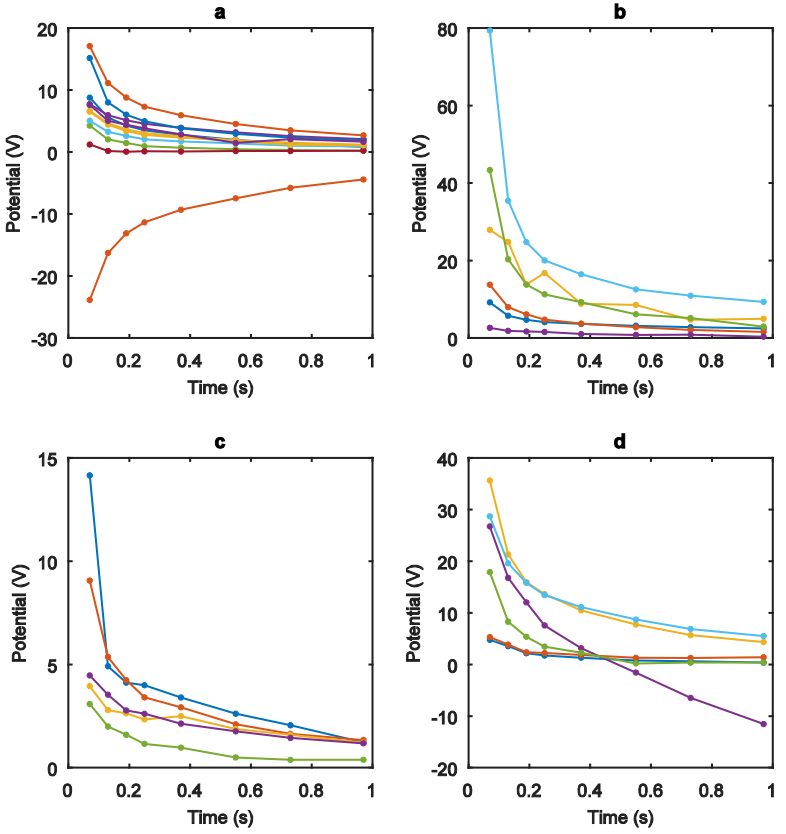

Figure 6.2. Examples of unprocessed decay curves. (a) a negative decay curve. (b) noise affected decay curve (yellow) (c) a decay curve with a disturbed first time gate (blue) (d) Disturbed decay curve becoming negative after ~0.5s (purple).

6.3 Data inversion

The inversions of processed data were made in AarhusInv (Fiandaca et al. 2012; Fiandaca et al. 2013). In the forward response modelling, the complex conductivity distribution is calculated in a finite element mesh for a number of frequency decades. The model space is then defined by frequency, resistivity and the spectral IP parameters of the Cole-Cole or the CPA model. The complex impedance transfer function of the system can be calculated for any electrode quadruple and be transformed to a potential response in time domain via inverse Fourier transform. The finite length of current pulses in time domain measurements and the stacking procedure can affect the potential response considerably. The transmitted waveform and received potential response is therefore modelled and superposed in the forward response (Fiandaca et al. 2012; Fiandaca et al. 2013). The data and the forward response are then used in an iterative inversion process, where the misfit between the data and the model is minimized (Auken et al. 2014).

In paper I, the data was inverted with both the Cole-Cole and the CPA models, although the Cole-Cole inversion of the data was considered uncertain due to the short measured time interval (0.07-0.97s). The data were inverted using L2-norm constraints with horizontal and vertical constraints of 7.5% and 25% respectively. The model fit was checked via a visual comparison between the measured and the inverted decays. An example of a good model fit with the CPA model is shown in Figure 6.3a. For the decays in Figure 6.3b, the CPA model underestimates the potential values at early times. In this case, a Cole-Cole model may fit the data better.

For paper II, a new signal processing scheme was available which enabled recovering of early decay times (Olsson et al. 2016). The time interval 0.009-0.974s was used, and the extra decade of data increased the possibilities of recovering spectral information during the inversions for paper II. In addition, shorter relaxation times were generally expected in the consolidated limestone analyzed in paper II, compared to the unconsolidated soils which were in focus in paper I. For these reasons, the Cole-Cole model was used for the inversions in paper II. The data were inverted using L2-norm constraints with horizontal and vertical constraints of 15% and 50% respectively.

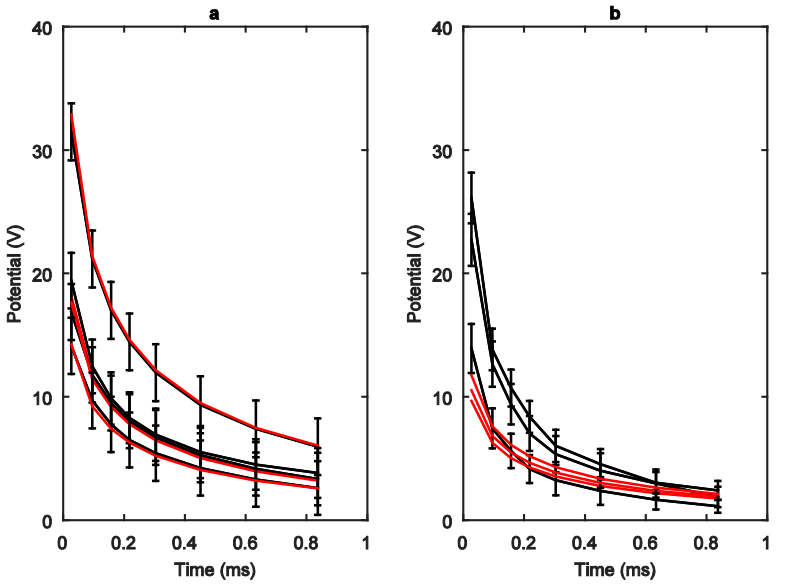

Figure 6.3. Fit between data (black) and CPA inverted decays (red). The model underestimates the chargeability in (b), where the decays likely contain spectral information.

6.4 Interpretation

The inverted data that were analyzed in paper I were measured on a site contaminated with tetrachloroethylene (PCE). PCE is a dense non-aqueous phase liquid (DNAPL), and the physical properties of the contaminant infer that it affects the pore geometry of the investigated soil.

The inverted results were initially compared with borehole data of DNAPL concentrations collected at the site, but the direct comparison did not show any strong correlation with the resistivity or IP anomalies. Previous experiences from similar investigations were therefore sought in the literature. However, no consensus was found in the results of previous research, and several different conceptual models of NAPL geometry in the pore space have been used to interpret data from both laboratory and field studies. Therefore the probable effect of possible NAPL configurations on the spectral IP response of a granular material (based on current knowledge of physical mechanisms,

see chapter 4) was discussed in paper I. Both interpretations from previous research and novel ideas were taken into account.

The possible NAPL configurations were based on the common physical properties of the fluids and on previous research in the fields of petrophysics and environmental research. Since the geological material at the investigated site consists mainly of sandy chalk till (in which no large IP effects are expected), the simple conceptual models discussed in paper I were considered accurate enough to guide the interpretation of the IP responses measured at the site. In a more complex geological setting, the conceptual models in paper I might not be applicable.

The inverted data in paper II were also ambiguous to interpret. Varying resistivity and spectral IP responses were found in the investigated limestone bedrock. Since IP investigations of limestones are not common in the literature, the microstructure and composition of limestone from the Kristianstad basin were investigated. General characteristics and a detailed lithological analysis of a nearby deeply drilled core were available in the geological literature. Access to drill cutting samples was also provided by an entrepreneur working in the Kristianstad basin after the DCIP survey. These samples were investigated with Scanning Electron Microscopy (SEM) and Energy Dispersive X-ray Spectroscopy (EDS) and provided detailed information of varying microstructure and mineral composition at different levels of the limestone. The geological characterization of the investigated limestone served as a basis for the interpretation of the varying IP responses measured at the site.

The field data interpretations presented in the next chapter are rather theoretical and qualitative than empirical and quantitative. Quantitative results of field data can be uncertain for several reasons, including insufficient amount of reference data for statistical significance and different measurement accuracy of the compared quantities. For example, the spatial accuracy of the borehole contaminant concentrations used in paper I are high, while the corresponding IP responses are representative of a relatively large soil volume. Data quality, processing and inversion also infer uncertainties in the exact accuracy of the inverted IP values. Qualitative interpretations of field data that can be theoretically supported by microgeometrical properties might also have a larger potential for providing results which can be useful and applicable in future field studies.

Chapter 7: Main Results

7.1 Spectral IP responses of NAPL contaminated soil

Previous results from field and laboratory IP investigations on NAPL contaminated soil vary a lot and point in opposite directions. In paper I (Johansson et al. 2015), previous research is reviewed and DCIP field results are presented, measured at a tetrachloroethylene (PCE) contaminated site.

The four possible configurations of NAPLs in a water saturated pore space that were discussed in paper I are shown in Figure 7.1. Depending on factors such as e.g. concentration, oil wettability and vertical or horizontal location in the contaminant plume, the NAPLs can be present in pores or pore throats of the granular material, interconnected through several pores or coating grain surfaces (Figure 7.1a-d).

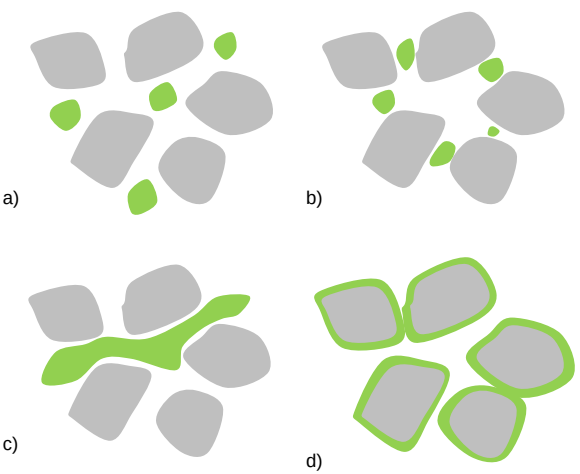

Figure 7.1. Different conceptual models of possible NAPL configurations in a granular pore space (modified from Johansson et al. 2015). The different models are expected to affect spectral IP parameters in different ways, see Table 7.1.

Expected spectral IP (Cole-Cole) responses of these systems (Table 7.1), theoretically based on the electrochemical and membrane polarization mechanisms, were discussed and presented in paper I.

Table 7.1. Expected spectral Cole-Cole responses of the NAPL configurations in Figure 7.1 (modified from Johansson et al. 2015). The responses are discussed in Johansson et al. (2015) and are based on the electrochemical (EC) and membrane (M) polarization mechanisms.

Conceptual model	Chargeabiliy (m_0)		Relaxation time (τ)		Frequency factor (c)	
	EC	M	EC	M	EC	M
A	increase	increase	decrease	decrease	decrease	decrease
B	increase	increase	decrease	unchanged	decrease	unchanged
C	decrease	not present	unchanged	not present	decrease	not present
D	increase or decrease	increase	increase	decrease	decrease	decrease

The field results in paper I showed that enhanced IP effects appeared next to the PCE source zone, i.e. not at the location where the highest concentrations of free phase contaminants had been measured (Figure 7.2). At the locations of the phase anomalies, the measured PCE concentrations were intermediately large. The enhanced phase and normalized phase were therefore interpreted as a representation of a degradation zone, where partial degradation of the free phase PCE has resulted in a NAPL configuration similar Figure 7.1a. According to the electrochemical and membrane polarization mechanisms, such a NAPL configuration is expected to give rise to an enhanced IP response compared to the IP response of a clean soil.

In contrast to this, a NAPL configuration similar to Figure 7.1c is expected to decrease the IP response of a contaminated soil. This could explain why no phase anomalies are present in the source zone where the highest PCE concentrations have been measured, since high concentrations increase the probability of interconnected NAPL in the pore space. More research is needed to validate the influence of different NAPL configurations on the spectral IP response, but it is likely that these results at least partly can explain why varying results have been achieved in previous research.

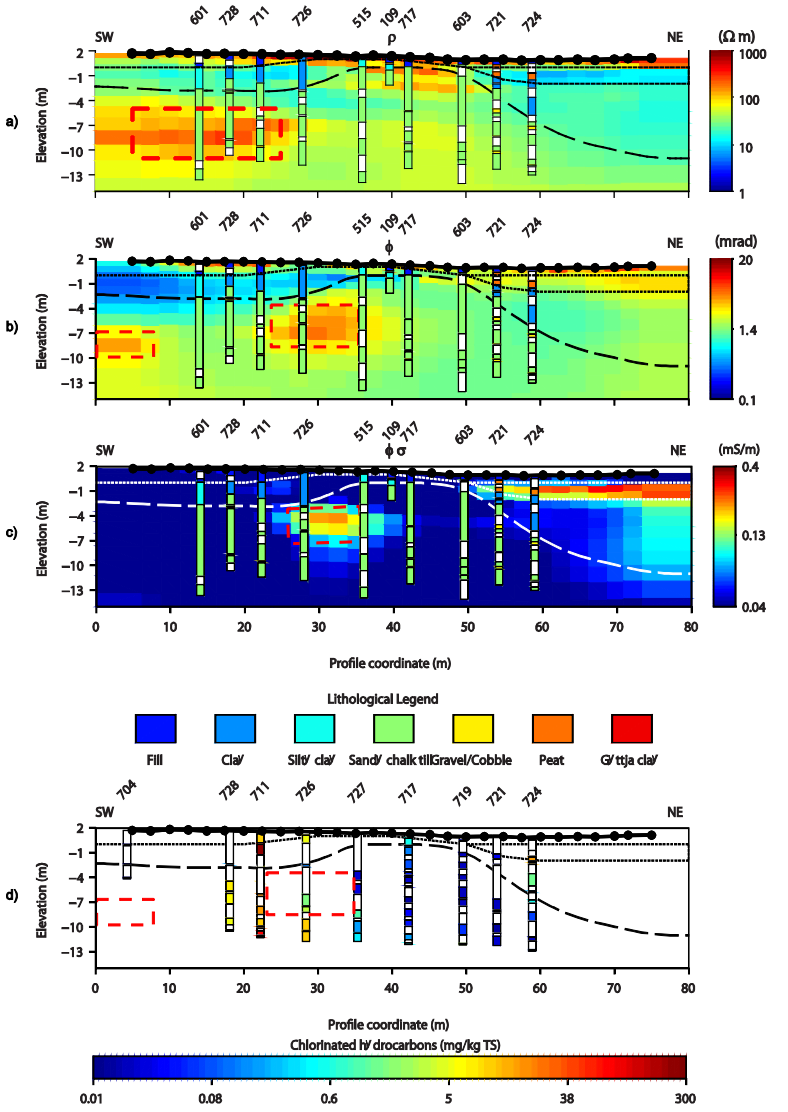

Figure 7.2. Field results from the investigated site, showing sections of resistivity (a), phase (c) and normalized phase (c) with superposed geological borehole information. Total chlorinated hydrocarbon concentrations measured in the boreholes are shown in d. Increased phase and normalized phase values can be observed at the border of the PCE source zone (as indicated by high chemical concentrations in (d) (Johansson et al. 2015)).

7.2 Varying spectral IP responses in a Cretaceous limestone

In previous research, resistivity and IP has been used to map fractured and weathered zones in bedrocks. In studies of silicate based rock types, zones with low resistivity and high chargeability have been indicators of clay weathered fracture zones, where the clay is responsible for the elevated IP responses. In the Cretaceous limestone (Kristianstad basin) investigated in paper II, weak IP responses were expected. However, anomalous zones of elevated normalized chargeability and low resistivity were found. The low resistive zones could indicate e.g. fracture or karst zones, but clay weathering processes are naturally limited in limestones. In a weathered limestone, the dissolution of calcium carbonate would rather be expected to lead to decreased IP responses. It was therefore uncertain how to interpret the detected zones of elevated normalized chargeability in paper II (Johansson et al. 2016).

Since the main survey area in paper II was located in an urban environment where it could not be completely excluded that noise and 3D-effects distort the DCIP results, a reference line was also measured in a rural area approximately 4km from the main survey site. The Cole-Cole inverted results from the reference line are shown in Figure 7.3. At this location, the limestone bedrock surface is located a few meters below the ground surface. Figure 7.3a-d shows that the resistivity and the Cole-Cole parameters varies in the bedrock. Previous research has shown that normalized chargeability (Figure 7.3e) often describes structural surface polarization properties better than chargeability (Figure 7.3b). Although the normalized chargeability generally is low in the limestone, anomalous zones of elevated values can be observed. Interesting variations in Cole-Cole relaxation time and frequency factor (Figure 7.3b-c) could possibly reflect textural variations within the limestone. Since no man-made constructions or installations are present in vicinity of the reference line, these results confirm that variations in IP response can be linked to the limestone composition or structure.

The analysis of the drill cutting samples from a borehole in the Kristianstad basin showed that the character of the limestone varied between different levels, from almost pure calcium carbonate based limestone to limestone with quartz and feldspar grains and clay matrix. Varying presence of clay matrix could be a possible explanation to varying IP responses of the limestone. In

addition, pyrite minerals were detected in most of the core levels, as well as glauconitic sand (Figure 7.4). Varying presence of these minerals could also be an explanation of varying IP responses within the limestone.

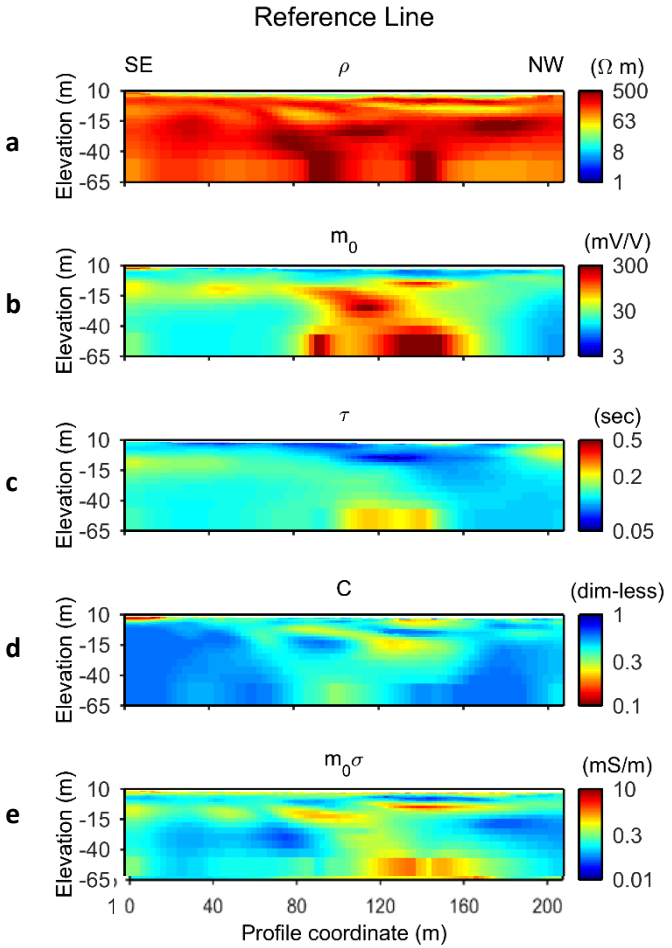

Figure 7.3. Variations in Cole-Cole parameters and normalized chargeabiltiy measured in a Cretaceous limestone bedrock (Johansson et al. 2016)

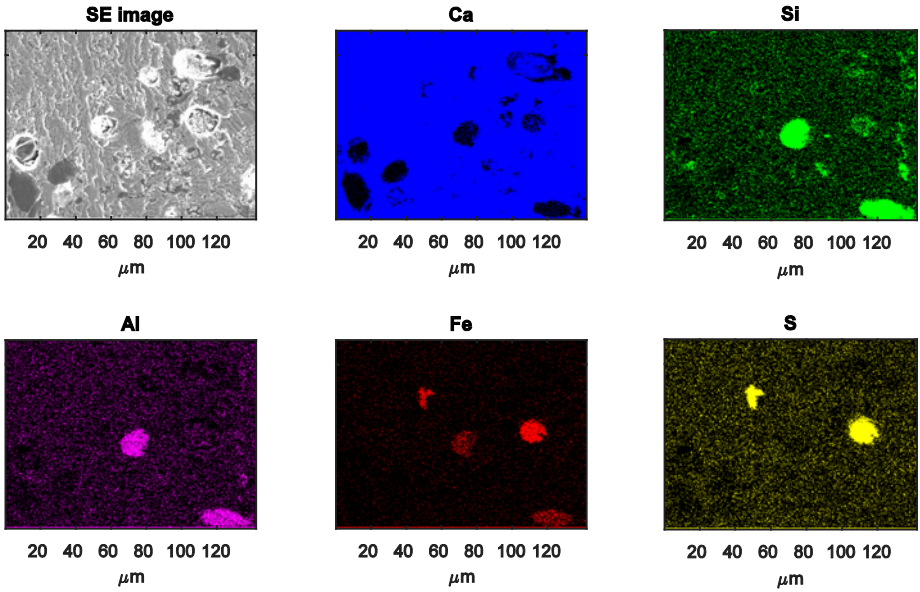

Figure 7.4. SEM and EDS results from a limestone sample, showing prescence of both pyrite (indicated by Fe and S) and glauconitic grains (indicated by Si, Al and Fe) within the limestone (modified from Johansson et al. 2016). The amounts of pyrite and glauconite varied at different levels in the core.

A lithological analysis of a relatively closely located core in the Kristianstad basin confirms variations in microgeometrical properties in the limestone. The variations in this core originate from a varying sedimentation environment during the formation of the limestone. Local depressions or channels in the bedrock at some point or collapsed karst cavities could explain vertical variations in the microgeometry.

Chapter 8: Conclusions and Future Work

8.1 Conclusions

Interpretation of field data is not always straight forward – many unknown factors could influence the IP response of the subsurface. It is crucial to initially evaluate if observed IP effects could be a result of bad data quality, 3D-effects or noise, especially when the data have been measured in urban environments. Secondly, it is important to obtain an acceptable fit between the data and the inverted model. With spectral inversion, this involves an assessment of which phenomenological model (e.g. the Cole-Cole or the CPA model) the data should be fitted with.

From this work, it can be concluded that it is possible to obtain spectral IP models of consistent quality from time domain IP measurements in an urban environment. This is a result of new developments in data acquisition techniques, data processing and inversion methods. Challenging conditions with periodic noise from train traffic and power lines is handled with improved data filtering. Although it is more favorable to measure with longer time pulses, it has been shown that under certain conditions, spectral information can be recovered from data measured with as short on-off times as 1s.

The interpretation of inverted spectral IP models based on field data can be challenging since microgeometrical and microchemical factors are often unknown. However, the interpretation can be enhanced by knowledge of relationships obtained in lab studies. In addition, conceptual models of the pore scale geometry and chemical composition can aid interpretation of field data.

A general conclusion of this work is that much knowledge about granular silicate soils and sedimentary rocks have already been obtained in previous research (chapter 5). The established relationships should be possible to use qualitatively in field scale interpretation of spectral IP parameters more or less

directly. For example, higher IP magnitude and shorter relaxation times could indicate more consolidated conditions in an otherwise homogeneous sandstone. Similarly, lower IP magnitude could indicate higher water content or saline groundwater. However, the interpretation of field scale data always requires knowledge of site specific factors and a critical review of different possible sources to the observed signals.

The conclusions that can be drawn from the work on NAPL contaminated soil (presented in paper I) is that it is difficult to correlate NAPL concentrations to IP variations in a similar way as groundwater salinity can be correlated to resistivity variations. The IP responses of NAPL contaminated soils are probably not only related to the contaminant concentrations, but also to other factors. One important factor that depends on the physical properties of the contaminants is the NAPLs influence on the pore geometry and the interfaces between different phases in the soil. The conceptual model of physical mechanisms in the pore space enhanced the interpretation of the field data in paper I.

From the analysis of spectral IP responses of limestones (paper II), the main conclusion is that similar IP responses can indicate different rock properties depending on the mineral constituents of the rock. For example, geological weathering processes affect the physical properties of silicate and calcium carbonate rocks differently. The SEM and EDS-analysis gave an important insight into the microgeometry and mineralogical content of the investigated limestone. The microgeometry of the limestone is not well represented by many current IP mechanisms (chapter 5), which are based around the response of granular homogeneous soils and rocks. More research is needed to understand spectral IP behavior of limestones, for example, the possible effects of different fossil grain shapes and the degree of cementation.

8.2 Future work

Generally, there seems to exist a gap between the field scale and the laboratory scale in understanding of IP. This gap needs to be bridged by knowledge of IP behavior in samples with heterogeneous structures. Planned future work includes combinations between laboratory IP measurements at microgeometrical characterization. More research is also needed about the theoretical equivalence of time and frequency domain measurements. This

topic is most likely going to be partly covered in future work via combinations of lab scale time- and frequency domain measurements.

On the topic of IP response of NAPL contaminated soil, X-ray tomography will be combined with frequency domain laboratory measurements. The aim is to verify how different geometrical configurations (reviewed in paper I) can affect IP spectra. Another planned experiment is to perform time lapse IP measurements in a tank with sand, NAPL and bacteria. In this way, the effect on spectral IP of the degradation of a NAPL can be monitored in a controlled environment.

Future research is also planned for natural and uncontaminated geological material. To study possible relationships between spectral IP and rock quality, field results will be compared to core samples, which will be investigated with microgeometrical methods and laboratory IP measurements.

References

Abdel Aal, G.Z., Slater, L.D. & Atekwana, E.A., 2006. Induced-polarization measurements on unconsolidated sediments from a site of active hydrocarbon biodegradation. *Geophysics*, 71(2), pp.H13–H24.

Atekwana, E.A. & Slater, L.D., 2009. Biogeophysics: A new frontier in Earth science research. *Reviews of Geophysics*, 47(4), pp.1–30.

Auken, E., Christiansen, A. V., Kirkegaard, C., Fiandaca, G., Schamper, C., Behroozmand, A. A., Binley, A., Nielsen, E., Effersø, F., Christensen, N.B., Sørensen, K., Foged, N. & Vignoli, G., 2014. An overview of a highly versatile forward and stable inverse algorithm for airborne, ground-based and borehole electromagnetic and electric data. *Exploration Geophysics*, 46(3), pp.223–235.

Bard, A.J. & Faulkner, L.R., 2001. *Electrochemical Methods Fundamentals and Applications* Second ed., John Wiley & Sons, Inc.

Bertin, J. & Loeb, J., 1976. *Experimental and Theoretical Aspects of Induced Polarization*, Berlin Stuttgart: Gebrüder Borntraeger.

Binley, A., Slater, L. D., Fukes, M., & Cassiani, G., 2005. Relationship between spectral induced polarization and hydraulic properties of saturated and unsaturated sandstone. *Water Resources Research*, 41(12), W12417.

Boadu, F.K. & Owusu-Nimo, F., 2010. Influence of petrophysical and geotechnical engineering properties on the electrical response of unconsolidated earth materials. *Geophysics*, 75(3), pp.G21–G29.

Brandes, I. & Acworth, I., 2003. Intrinsic Negative Chargeability of Soft Clays. In *Procs. ASEG 16th Geophysical Conference and Exhibition, February 2003, Adelaide*.

Butler, K.D., 2005. *Near-surface Geophysics* Investigat. K. D. Butler, ed.13, Society of exploration geophysicists.

Börner, F., Gruhne, M. & Schön, J., 1993. Contamination indications derived from electrical properties in the low frequency range. *Geophysical Prospecting*, 41(1), pp.83–98.

Cardarelli, E. & Di Filippo, G., 2009. Electrical resistivity and induced polarization tomography in identifying the plume of chlorinated hydrocarbons in sedimentary formation: a case study in Rho (Milan - Italy). *Waste Management & Research*,

27(6), pp.595–602.

Cassiani, G., Kemna, A., Villa, A., & Zimmermann, E., 2009. Spectral induced polarization for the characterization of free-phase hydrocarbon contamination of sediments with low clay content. *Near Surface Geophysics*, 7(5-6), pp.547–562.

Chambers, J. E., Loke, M. H., Ogilvy, R. D., & Meldrum, P. I., 2004. Non-invasive monitoring of DNAPL migration through a saturated porous medium using electrical impedance tomography. *Journal of contaminant hydrology*, 68, pp.1–22.

Cole, K.S. & Cole, R.H., 1941. Dispersion and Absorption in Dielectrics I. Alternating Current Characteristics. *The Journal of Chemical Physics*, 9, pp.341–351.

Dahlin, T. & Leroux, V., 2012. Improvement in time-domain induced polarization data quality with multi-electrode systems by separating current and potential cables. *Near Surface Geophysics*, 10, pp.545–565.

Dahlin, T., Leroux, V. & Rosqvist, H., 2010. Resistivity-IP mapping for landfill applications. *First Break*, 28(August), pp.101–105.

Dahlin, T. & Loke, M.H., 2015. Negative apparent chargeability in time-domain induced polarisation data. *Journal of Applied Geophysics*, 123, pp.322–332.

Dahlin, T. & Zhou, B., 2004. A numerical comparison of 2D resistivity imaging with 10 electrode arrays. *Geophysical Prospecting*, 52(5), pp.379–398.

Deceuster, J. & Kaufmann, O., 2012. Improving the delineation of hydrocarbon-impacted soils and water through induced polarization (IP) tomographies: a field study at an industrial waste land. *Journal of contaminant hydrology*, 136-137(August 2012), pp.25–42.

Dias, C.A., 2000. Developments in a model to describe low-frequency electrical polarization of rocks. *Geophysics*, 65(2), pp.437–451.

Fiandaca, G., Ramm, J., Binley, A., Gazoty, A., Christiansen, a. V., & Auken, E., 2013. Resolving spectral information from time domain induced polarization data through 2-D inversion. *Geophysical Journal International*, 192(2), pp.631–646.

Fiandaca, G., Auken, E., Christiansen, A. V., & Gazoty, A., 2012. Time-domain-induced polarization: Full-decay forward modeling and 1D laterally constrained inversion of Cole-Cole parameters. *Geophysics*, 77(3), pp.E213–E225.

Flores Orozco, A., Kemna, A., Oberdörster, C., Zschornack, L., Leven, C., Dietrich, P., & Weiss, H., 2012. Delineation of subsurface hydrocarbon contamination at a former hydrogenation plant using spectral induced polarization imaging. *Journal of contaminant hydrology*, 136-137, pp.131–44.

Flores Orozco, A., Williams, K. H., Long, P. E., Hubbard, S. S., & Kemna, A., 2011. Using complex resistivity imaging to infer biogeochemical processes associated with bioremediation of an uranium-contaminated aquifer. *Journal of Geophysical Research: Biogeosciences*, 116(3), pp.1–17.

Gazoty, A., Fiandaca, G., Pedersen, J., Auken, E., & Christiansen, A. V., 2012. Mapping of landfills using time-domain spectral induced polarization data: the Eskelund case study. *Near Surface Geophysics*, pp.575–586.

Iliceto, V., Santarato, G. & Veronese, S., 1982. An approach to the identification of fine sediments by induced polarization laboratory measurements. *Geophysical Prospecting*, 30, pp.331–347.

Iwamoto, M., 2012. Maxwell–Wagner Effect. In B. Bhushan, ed. *Encyclopedia of Nanotechnology*. pp. 1276–1285.

Johansson, S., Sparrenbom, C., Fiandaca, G., Lindskog, A., Olsson, P.-I., Dahlin, T., & Rosqvist, H., 2016. Investigations of a Cretaceous limestone with spectral induced polarization and scanning electron microscopy. *Submitted for publication (Geophysical Journal International)*.

Johansson, S., Fiandaca, G. & Dahlin, T., 2015. Influence of non-aqueous phase liquid configuration on induced polarization parameters: Conceptual models applied to a time-domain field case study. *Journal of Applied Geophysics*, 123, pp.295–309.

Jougnot, D., Ghorbani, A., Revil, A., Leroy, P., & Cosenza, P., 2010. Spectral induced polarization of partially saturated clay-rocks: a mechanistic approach. *Geophysical Journal International*, 180(1), pp.210–224.

Kemna, A., Binley, A., Cassiani, G., Niederleithinger, E., Revil, A., Slater, L., Williams, K.H., Flores Orozco, A., Haegel, F.-H., Hördt, A., Kruschwitz, S., Leroux, V., Titov, K &Zimmermann, E., 2012. An overview of the spectral induced polarization method for near-surface applications. *Near Surface Geophysics*, 10, pp.453–468.

Kemna, A., 2000. *Tomographic Inversion of Complex Resistivity - Theory and Application*. Ruhr-Universität Bochum.

Koch, K., Kemna, A., Irving, J., & Holliger, K., 2011. Impact of changes in grain size and pore space on the hydraulic conductivity and spectral induced polarization response of sand. *Hydrology and Earth System Sciences*, 15(6), pp.1785–1794.

Leroy, P., Revil, A, Kemna, A, Cosenza, P., & Ghorbani, A, 2008. Complex conductivity of water-saturated packs of glass beads. *Journal of colloid and interface science*, 321(1), pp.103–17. Available at: http://www.ncbi.nlm.nih.gov/pubmed/18272167 [Accessed May 29, 2013].

Leroy, P., & Revil, A., 2009. A mechanistic model for the spectral induced polarization of clay materials. *Journal of Geophysical Research: Solid Earth*, 114(B10202).

Lesmes, D. & Friedman, S., 2005. Hydrogeophysics. In Y. Rubin and S. S. Hubbard, ed. Springer, pp. 87–128.

Lesmes, D.P. & Frye, K.M., 2001. Influence of pore fluid chemistry on the complex conductivity and induced polarization responses of Berea sandstone. *Journal of Geophysical Research*, 106(B3), pp.4079–4090.

Lesmes, D.P. & Morgan, F.D., 2001. Dielectric spectroscopy of sedimentary rocks. *Journal of Geophysical Research*, 106(B7), pp.13329–13346.

de Lima, O.A.L. & Sharma, M.M., 1992. A generalized Maxwell-Wagner theory for membrane polarization in shaly sands. *Geophysics*, 57(3), pp.431–440.

Magnusson, M.K., Fernlund, J.M.R. & Dahlin, T., 2010. Geoelectrical imaging in the interpretation of geological conditions affecting quarry operations. *Bulletin of Engineering Geology and the Environment*, 69(3), pp.465–486.

Marshall, D.J. & Madden, T.R., 1959. Induced polarization, a study of its causes. *Geophysics*, XXIV(4), pp.790–816.

Martinho, E., Almeida, F. & Senos Matias, M.J., 2006. An experimental study of organic pollutant effects on time domain induced polarization measurements. *Journal of Applied Geophysics*, 60(1), pp.27–40.

Nordsiek, S. & Weller, A., 2008. A new approach to fitting induced-polarization spectra. *Geophysics*, 73(6), pp.F235–F245.

Ntarlagiannis, D. et al., 2005. Low-frequency electrical response to microbial induced sulfide precipitation. *Journal of Geophysical Research*, 110(G2).

Olhoeft, G.R., 1985. Low frequency electrical properties. *Geophysics*, 50(12), pp.2492–2503.

Olsson, P.-I., Fiandaca, G., Larsen, J. J., Dahlin, T., & Auken, E., 2016. Doubling the spectrum of time-domain induced polarization: removal of non-linear self-potential drift, harmonic noise and spikes, tapered gating, and uncertainty estimation. *Submitted for publication (Geophysical Journal International)*.

Pelton, W. H., Ward, S. H., Hallof, P. G., Sill, W. R., & Nelson, P. H., 1978. Mineral discrimination and removal of inductive coupling with multifrequency IP. *Geophysics*, 43(3), pp.588–609.

Personna, Y. R., Slater, L., Ntarlagiannis, D., Werkema, D., & Szabo, Z., 2013. Complex resistivity signatures of ethanol in sand-clay mixtures. *Journal of contaminant hydrology*, 149(2013), pp.76–87.

Powers, M.H., 1997. Modeling frequency-dependent GPR. *The Leading Edge*, 16(11), pp.1657–1662.

Revil, A., 2012. Spectral induced polarization of shaly sands: Influence of the electrical double layer. *Water Resources Research*, 48(2).

Revil, A. & Florsch, N., 2010. Determination of permeability from spectral induced polarization in granular media. *Geophysical Journal International*, 181(3), pp.1480–1498.

Revil, A., Koch, K. & Holliger, K., 2012. Is it the grain size or the characteristic pore size that controls the induced polarization relaxation time of clean sands and sandstones? *Water Resources Research*, 48(5).

Schmutz, M., Revil, A., Vaudelet, P., Batzle, M., Viñao, P. F., & Werkema, D. D., 2010. Influence of oil saturation upon spectral induced polarization of oil-

bearing sands. *Geophysical Journal International*, 183(1), pp.211–224.

Scott, J.B.T. & Barker, R.D., 2003. Determining pore-throat size in Permo-Triassic sandstones from low-frequency electrical spectroscopy. *Geophysical Research Letters*, 30(9).

Seigel, H.O., 1959. Mathematical formulation and type curves for induced polarization. *Geophysics*, XXIV(3), pp.547–565.

Sen, P.N., 1981. Relation of certain geometrical features to the dielectric anomaly of rocks. *Geophysics*, 46(12), pp.1714–1720.

Sen, P.N., Scala, C. & Cohen, M.H., 1981. A self-similar model for sedimentary rocks with application to the dielectric constant of fused glass beads. *Geophysics*, 46(5), pp.781–795.

Slater, L. & Lesmes, D.P., 2002a. Electrical-hydraulic relationships observed for unconsolidated sediments. *Water Resources Research*, 38(10), pp.1–13.

Slater, L.D. & Lesmes, D., 2002b. IP interpretation in environmental investigations. *Geophysics*, 67(1), pp.77–88.

Sumner, J.S., 1976. *Principles of induced polarization for geophysical exploration*, Amsterdam: Elsevier Scientific Publishing Company.

Titov, K., Kemna, A., Tarasov, A., & Vereecken, H., 2004. Induced Polarization of Unsaturated Sands Determined through Time Domain Measurements. *Vadose Zone Journal*, 3(4), pp.1160–1168.

Titov, K., Komarov, V., Tarasov, V., & Levitski, A., 2002. Theoretical and experimental study of time domain-induced polarization in water-saturated sands. *Journal of Applied Geophysics*, 50(4), pp.417–433.

Ustra, A., Slater, L., Ntarlagiannis, D., & Elis, V., 2012. Spectral Induced Polarization (SIP) signatures of clayey soils containing toluene. *Near Surface Geophysics*, 10, pp.503–515.

Vanhala, H., 1997. Mapping oil-contaminated sand and till with the spectral induced polarization (SIP) method. *Geophysical Prospecting*, 45(2), pp.303–326.

Ward, S., 1988. The resistivity and induced polarization methods. In *1st EEGS Symposium on the Application of Geophysics*.

Weller, A. & Slater, L.D., 2015. Induced polarization dependence on pore space geometry : Empirical observations and mechanistic predictions. *Journal of Applied Geophysics*, 123, pp.310–315.

Vinegar, H.J. & Waxman, M.H., 1984. Induced polarization of shaly sands. *Geophysics*, 49(8), pp.1267–1287.

Wong, J., 1979. An electrochemical model of the induced-polarization phenomenon in disseminated sulfide ores. *Geophysics*, 44(7), pp.1245–1265.

Van Voorhis, G.D., Nelson, P.H. & Drake, T.L., 1973. Complex resistivity spectra of porphyry copper mineralization. *Geophysics*, 38(1), pp.49–60.

Zhang, C., Slater, L., Redden, G., Fujita, Y., Johnson, T., & Fox, D., 2012. Spectral

induced polarization signatures of hydroxide adsorption and mineral precipitation in porous media. *Environmental Science and Technology*, 46(8), pp.4357–4364.

Zisser, N., Kemna, A. & Nover, G., 2010. Relationship between low-frequency electrical properties and hydraulic permeability of low-permeability sandstonesRelationship. *Geophysics*, 75(3), pp.E131–E141.

Zonge, K.L., Sauck, W.A. & Sumner, J.S., 1972. Comparison of time, frequency and phase measurements in induced polarization. *Geophysical Prospecting*, 20(3), pp.626–648.

Appended papers

Paper I

Johansson, S., Fiandaca, G. and Dahlin, T.

Influence of non-aqueous phase liquid configuration on induced polarization parameters: Conceptual models applied to a time-domain field case study.

Special issue: Advances in IP, Journal of Applied Geophysics, Volume 123, December 2015, Pages 295–309.

Journal of Applied Geophysics 123 (2015) 295–309

Contents lists available at ScienceDirect

Journal of Applied Geophysics

journal homepage: www.elsevier.com/locate/jappgeo

Influence of non-aqueous phase liquid configuration on induced polarization parameters: Conceptual models applied to a time-domain field case study

Sara Johansson [a,*], Gianluca Fiandaca [b], Torleif Dahlin [a]

[a] Engineering Geology, Lund University, P.O. Box 118, SE-22100 Lund, Sweden
[b] Department of Geoscience, Aarhus University, C.F.Møllers Allé 4, Building 1120, 8000 Aarhus C, Denmark

ARTICLE INFO

Article history:
Received 14 April 2015
Received in revised form 10 July 2015
Accepted 26 August 2015
Available online 31 August 2015

Keywords:
Spectral induced polarization
Pore space properties
Non-aqueous phase liquids
Membrane polarization
Electrochemical polarization
Cole–Cole model

ABSTRACT

Resistivity and induced polarization (IP) measurements on soil contaminated with non-aqueous phase liquids (NAPLs) show a great variety in results in previous research. Several laboratory studies have suggested that the presence of NAPLs in soil samples generally decrease the magnitude of the IP-effect, while others have indicated the opposite. A number of conceptual models have been proposed suggesting that NAPLs can alter the pore space in different ways, e.g. by coating the grain surfaces and thus inhibiting grain polarization, or by changing the pore throat size and thus affecting the membrane polarization mechanism. The main aim of this paper is to review previously published conceptual models and to introduce some new concepts of possible residual NAPL configurations in the pore space. Time domain induced polarization measurements were performed at a NAPL contaminated field site, and the data were inverted using the Constant Phase Angle (CPA) model and the Cole–Cole model respectively. No significant phase anomalies were observed in the source area of the contamination when the CPA inverted profiles were compared with soil sampling results of free-phase contaminant concentrations. However, relatively strong phase and normalized phase anomalies appeared next to the source area, where residual free-phase presence could be expected according to the chemical data. We conclude that depending on the NAPL configuration, different spectral IP responses can be expected. In previous research, the NAPL configurations in different samples or field sites are often unknown, and this may to some extent explain why different results have been achieved by different authors. In our field case, we believe that the NAPL forms a more or less continuous phase in the pore space of the source zone leading to an absence of IP anomalies. The increase in phase and normalized phase angle observed next to the source zone is interpreted as a degradation zone. The ongoing biodegradation may have led to a fractionation of the continuous NAPL in the outer part of the original source zone, leading to residual presence of isolated NAPL droplets in the soil pores. With such NAPL configurations, an increased polarization can be expected according to the electrochemical- and membrane polarization mechanisms. More research is needed to confirm the effects of different NAPL configuration on spectral IP parameters.

1. Introduction

A common environmental problem is the remediation of ground contaminated with non-aqueous phase liquids (NAPLs), e.g. gasoline or industrial chlorinated solvents. These chemicals are immiscible liquids that do not easily dissolve in water, and as such they often exist as an own phase in the soil (a so called free-phase product). NAPLs are divided into light non-aqueous phase liquids (LNAPLs) and dense non-aqueous phase liquids (DNAPLs), where the former have a lower density and the latter have a higher density than water. The density difference has the implication that large LNAPL spills are often found floating on the groundwater surface when released into the ground, while DNAPLs sink trough the groundwater until it reaches a less permeable layer, e.g. the bedrock. Free-phase products of both LNAPLs and DNAPLs can exist as a continuous phase in the ground or as a residual phase, where parts of the contaminant have been trapped in the soil and are not displaced due to gravitational forces (Atekwana and Atekwana, 2010; Ajo-Franklin et al., 2006).

Delineations of NAPL plumes are commonly carried out by means of borehole drilling and chemical sampling. However, there is a risk of spreading the contaminants vertically during this process and the drillings are expensive and give point information rather than a continuous picture of the contaminant plume. Geophysical methods are, in a general sense, effective tools in providing continuous information of soil properties in between individual boreholes. Resistivity and induced polarization (IP) are methods that have been considered promising in order to achieve detection of NAPLs in soils, and research

* Corresponding author.
E-mail address: sara.johansson@tg.lth.se (S. Johansson).

http://dx.doi.org/10.1016/j.jappgeo.2015.08.010
0926-9851/

has been carried out in both laboratory and field. The interest in the resistivity method has emerged because NAPLs are electrical insulators and can cause a rise in resistivity when their free-phase products displace water in saturated soil. This has been observed in a number of lab and field studies on different kinds of NAPLs (e.g. Chambers et al., 2004; Cassiani et al., 2009; Naudet et al., 2014; Power et al., 2015). However, at field sites, the situation is complicated by the fact that the age and degradation status of the contaminants change the groundwater chemistry. Release of ions during biodegradation, or mineral weathering and dissolution caused by organic acids released by bacteria, can cause increased groundwater conductivity (Atekwana and Slater, 2009; Atekwana and Atekwana, 2010). Thus, increased bulk resistivity due to free-phase NAPL presence could be suppressed by increased groundwater conductivity.

A possible solution to the problem of using resistivity alone for NAPL detection is to extend the measurements to include IP. IP spectra or time decays are sensitive to properties at the pore scale, such as e.g. grain sizes, grain shape, grain surface chemistry and pore throat size distribution (e.g. Slater and Lesmes, 2002a; Scott and Barker, 2003; Binley et al., 2005; Nordsiek and Weller, 2008; Titov et al., 2010). Consequently, the IP method may have a greater potential of being able to detect NAPLs in the pore space compared to resistivity alone. However, the results of previous studies in both field and laboratory scale vary and sometimes point in opposite directions. Several laboratory measurements have suggested that the presence of NAPLs in water saturated soil samples generally reduce the magnitude of the IP effect (Börner et al., 1993; Vanhala et al., 1992; Vanhala, 1997; Chambers et al., 2004; Martinho et al., 2006; Schmutz et al., 2010; Revil et al., 2011), while others have indicated the opposite (Olhoeft, 1985; Titov et al., 2004; Cassiani et al., 2009; Schmutz et al., 2010, 2012). As expected, varied results have also been achieved in field surveys of NAPL contaminated ground. For example, free-phase NAPL presence in an unconfined aquifer have resulted in decreased chargeability (Flores Orozco et al., 2012), while in another field study, high chargeability was interpreted as an indicator of LNAPLs in clayey sand (Deceuster & Kaufmann, 2012).

In contrast to several lab studies, where the relationship between NAPL concentration and IP response has been interpreted as essentially linear (e.g. Revil et al., 2011; Schmutz et al., 2010, 2012), other trends have also been observed. In some cases, a threshold value in the relationship between NAPL concentration and IP response in water saturated soil samples has been seen. Titov et al. (2004) found increasing chargeability with LNAPL content up to a saturation of 92% and decreasing chargeability with further increase of the LNAPL. A similar trend has been observed by Schmutz et al. (2012). In contrast, measurements by Martinho et al. (2006) indicated an initial decrease of chargeability values up to a LNAPL saturation of around 10% in clayey sand samples. Slightly increasing chargeability values were observed at higher contents, although all values were below the values of clean sand, in contrast to the data from Titov et al. (2004).

It is not always straightforward to compare the results from previous laboratory measurements since there can be variations in e.g. sample preparation and NAPL phases and species (Cassiani et al., 2009). Field data is often even more challenging because of different field circumstances such as geological setting and degradation status. Beyond variations in chemical, biological and geological parameters, a factor that plays a major role in understanding the effect on measured IP of NAPL in soils is the geometrical configuration of the free-phase product in the pore space. In published research, interpretation of IP data often rely on different conceptual models of NAPL configuration, which in different ways explain the observed results (e.g. Olhoeft, 1985; Titov et al., 2004; Martinho et al., 2006; Schmutz et al., 2010; Revil et al., 2011; Flores Orozco et al., 2012; Shefer et al., 2013). However, to date, there are no comparative studies discussing possible effects of different models. There is thus a need for a comprehensive discussion and comparison of various possible NAPL configurations, since this may enhance the understanding of why different results may be achieved when IP measurements are performed on NAPL contaminated soil.

The main aim of this paper is to review previously published conceptual models and to introduce some new concepts of possible residual NAPL configurations in the pore space. We will discuss how the conceptual models can be expected to influence spectral (Cole–Cole) IP parameters (Section 5). Field results from time domain IP measurements on a site contaminated with DNAPLs will be presented (Section 4) and discussed in relation to the qualitative results from the discussion of NAPL configurations. The data were inverted with both the Constant Phase Angle (CPA) model and the Cole–Cole model. The results indicate a zone of increased phase/chargeability and decreased relaxation time at a location outside the free-phase source area, while no effects can be distinguished at the locations where the highest DNAPL concentrations were observed. The increased IP effects are interpreted as possible effects of residual free-phase presence. We believe that the concentration and configuration of the DNAPL in the soil are important since this will affect the micro geometrical properties at the pore scale and the current paths through the soil.

In a wider context, we wish to raise the awareness of the importance of assumptions about the NAPL configuration in a pore space, an issue that was also stressed by Cassiani et al. (2009), and its possible impacts on spectral IP parameters. We believe that such considerations could enhance future interpretations of IP data measured on NAPL contaminated lab samples or field sites.

2. Theory

2.1. Polarization mechanisms

The mechanisms behind the spectral induced polarization response in metal-free soils are usually described in terms of electrochemical polarization, membrane polarization or Maxwell–Wagner polarization. The basis of the electrochemical polarization mechanism (also called grain polarization or Stern layer polarization) is the existence of electrical double layers (EDLs) around soil grains. The EDLs arises as a result of a negative surface charge on mineral grains surrounded by water, which leads to attachment of a fixed layer of counter-ions at the grain surface, the so called Stern layer. In addition, a second layer of counter-ions, called the diffuse layer, is formed and consists of more weakly electrostatically attracted solvent ions. When an electrical field is applied to the soil, the EDL becomes polarized (Schwarz, 1962). Modeling studies have shown that the polarization of the Stern layer is much stronger in magnitude compared to the polarization of the diffuse layer (De Lima and Sharma, 1992; Lesmes and Morgan, 2001; Leroy et al., 2008). The total polarization magnitude has been observed to be inversely proportional to the grain size of silts, sands and tills (Slater, 2002). The relaxation time increases with the characteristic grain (or pore throat) size, since this determine the possible length scale of diffusion for ions in the EDL (Slater, 2007).

The concept behind membrane polarization is that series of small ion-selective and non-selective zones exist in the pore system. The ion-selective zones can consist of negatively charged clay particles attracting a cloud of counter-ions, or narrow pores or pore-throats which to a large degree are occupied by the EDLs of the surrounding grains. When an electric field is applied to the system, ions are blocked in front of the ion-selective zones, and ions attached to mineral particles are displaced. The length ratio and relative ion transparencies between the ion-selective and non-selective zones determine the polarization magnitude, while the length of the non-selective zones controls the diffusion length scale and therefore the relaxation time (Marshall and Madden, 1959; Vinegar and Waxman, 1984; Titov et al., 2002).

The Maxwell–Wagner polarization mechanism is related to ion accumulations at borders between soil phases with different dielectrical properties, e.g. water and grains. This mechanism dominates at higher frequencies (above 1 kHz) and is also dependent on the shapes of

different phases in a soil matrix (Lesmes and Morgan, 2001). Quantification of the mechanism requires modeling with effective media theories, and this has usually been made with two-phase systems (De Lima and Sharma, 1992; Lesmes and Morgan, 2001; Leroy and Revil, 2009).

The IP effects measured in a natural soil likely consist of several superposed relaxation mechanisms, but no unifying theory covering interactions between all of the polarization mechanisms is available to date. Therefore, we will discuss both electrochemical and membrane polarization mechanisms in Section 5. Although Maxwell–Wagner effects are also likely to influence measured IP effects, this mechanism will not be further discussed. A study of the behavior of the Maxwell–Wagner effect in NAPL contaminated soil requires modeling of three-phase systems, and its behavior cannot be qualitatively predicted from simplified conceptual models as those that will be presented in Section 5. Furthermore, we are mainly interested in low-frequency mechanisms.

2.2. Frequency domain and time domain IP

In frequency domain, the amplitude- and phase-shifts of an alternating current (AC) that has traveled through a soil volume is measured. The total complex conductivity σ^* (the reciprocal of complex resistivity ρ^*) can be expressed as:

$$\sigma^* = |\sigma| e^{i\phi} \tag{1}$$

where $|\sigma|(S/m)$ is the measured magnitude of the amplitude and ϕ(mrad) is the phase angle.

In time domain, resistivity is measured during the injection of a direct current (DC) pulse, while chargeability is measured as the remaining potential after the current has been switched off. The intrinsic chargeability is defined as (Seigel, 1959):

$$m = \frac{V_s}{V_p} \tag{2}$$

where V_p is the primary voltage of the transmitted DC current and V_s is the maximum voltage immediately after the interruption of the current pulse. In practice, m is commonly measured and calculated as the integral of the decay curve during a defined time window:

$$m_i = \frac{1}{t(i+1) - t(i)} \int_{t(i)}^{t(i+1)} \frac{V}{V_p} dt. \tag{3}$$

The complex conductivity (Eq. (1)) can be rewritten in Cartesian coordinates:

$$\sigma^* = \sigma' + i\sigma'' \tag{4}$$

where σ' and σ'' are the real and imaginary parts of σ^*, which can be calculated as functions of both $|\sigma|$ and ϕ. The real part σ' represents the electrical conduction in the soil, which is mainly made up of ionic conduction in the groundwater and surface conduction along interconnected grains. The imaginary part σ'' represents the complex and frequency-dependent capacitive properties in the soil, i.e. it is usually assumed to be a measure of the induced polarization effect only. The time domain parameter m can be compared to the frequency domain ϕ, that is, it is affected not only by polarization mechanisms but also the bulk conductivity in the ground. The time domain equivalent to the frequency domain parameter σ'' is called the normalized chargeability (MN) and is calculated by a division with resistivity. Since the normalized parameters (during the right soil conditions, e.g. water saturated and metal free soil) can be assumed to be a measure of the IP effect alone, they are more sensitive to surface chemical properties of the material compared to m and ϕ (Slater and Lesmes, 2002b).

A number of phenomenological models exist which can be fitted to the IP spectra, among which the most commonly used are the Cole–Cole like model (Cole and Cole, 1941; Pelton et al., 1978) and the Constant Phase Angle (CPA) model (e.g. Van Voorhis et al., 1973). The Cole–Cole model assumes a peak frequency of the polarization spectra and implies four parameters describing the shape of the IP spectra. The Cole–Cole model describing the complex resistivity $\rho^*(\omega)$ is:

$$\rho^*(\omega) = \rho\left[1 - m_0\left(1 - \frac{1}{1 + (i\omega\tau)^c}\right)\right] \tag{5}$$

where $\rho(\Omega m)$ is the DC resistivity, $m_0(mV/V)$ is the chargeability as defined in (2), $\tau(s)$ is the relaxation time, c is the frequency factor, $\omega(rad)$ is the angular frequency and i is the imaginary unit (Pelton et al., 1978; Fiandaca et al., 2013). The response of soils or rocks with little or no frequency dependence of the phase shift is often described in frequency domain with the CPA model:

$$\rho^*(\omega) = K(i\omega)^{-b} \tag{6a}$$

in which the phase of the complex resistivity is constant over frequency

$$\phi = -\frac{\pi}{2} b. \tag{6b}$$

In the CPA model the modulus of the resistivity increases indefinitely for decreasing frequencies, and it is not possible to define a zero-frequency value, that can instead be defined in the Drake model (Van Voorhis et al., 1973):

$$\rho^*(\omega) = K(i\omega + \omega_l)^{-b} \tag{7a}$$

in which the low-frequency pole ω_l allows the definition of a zero-frequency resistivity ρ

$$\rho = \rho^*(0) = K(\omega_l)^{-b}. \tag{7b}$$

The Drake model and the CPA model coincide for $\omega \gg \omega_l$. In the present study when inverting for the CPA model we actually use a Drake model with low-frequency pole ω_l fixed to a small value (1 μHz). In this way we can invert directly for ϕ and ρ, instead of having to invert for the non-conventional parameter K of Eq. (6a).

3. Methods & materials

Resistivity and time domain IP (DCIP) were measured over a former dry-cleaning site in southern Sweden, where a large amount of tetrachloroethylene (PCE) was released between the early 1900s and the late 1980s. The site, which is one of the worst PCE contaminated areas in Sweden, rests on top of a major drinking aquifer, and a protected wetland is situated east of the property boundary, see Fig. 1.

The site and its surroundings have previously been extensively investigated with drilling and soil- and groundwater sampling in order to try to delineate the source area of the PCE spill as well as polluted groundwater plumes. While the source area of free-phase PCE resides within the boundaries of the former dry-cleaning site (Fig. 1), contaminated groundwater with dissolved degradation products have been widely spread over surrounding areas covering several hectares.

3.1. Previous investigations

The main aim of the DCIP survey was to investigate if the source area of free-phase PCE could be detected with DCIP. As reference data, geological classifications from the previous drilling investigations carried out in between 2008 and 2013 were used. The labeled boreholes

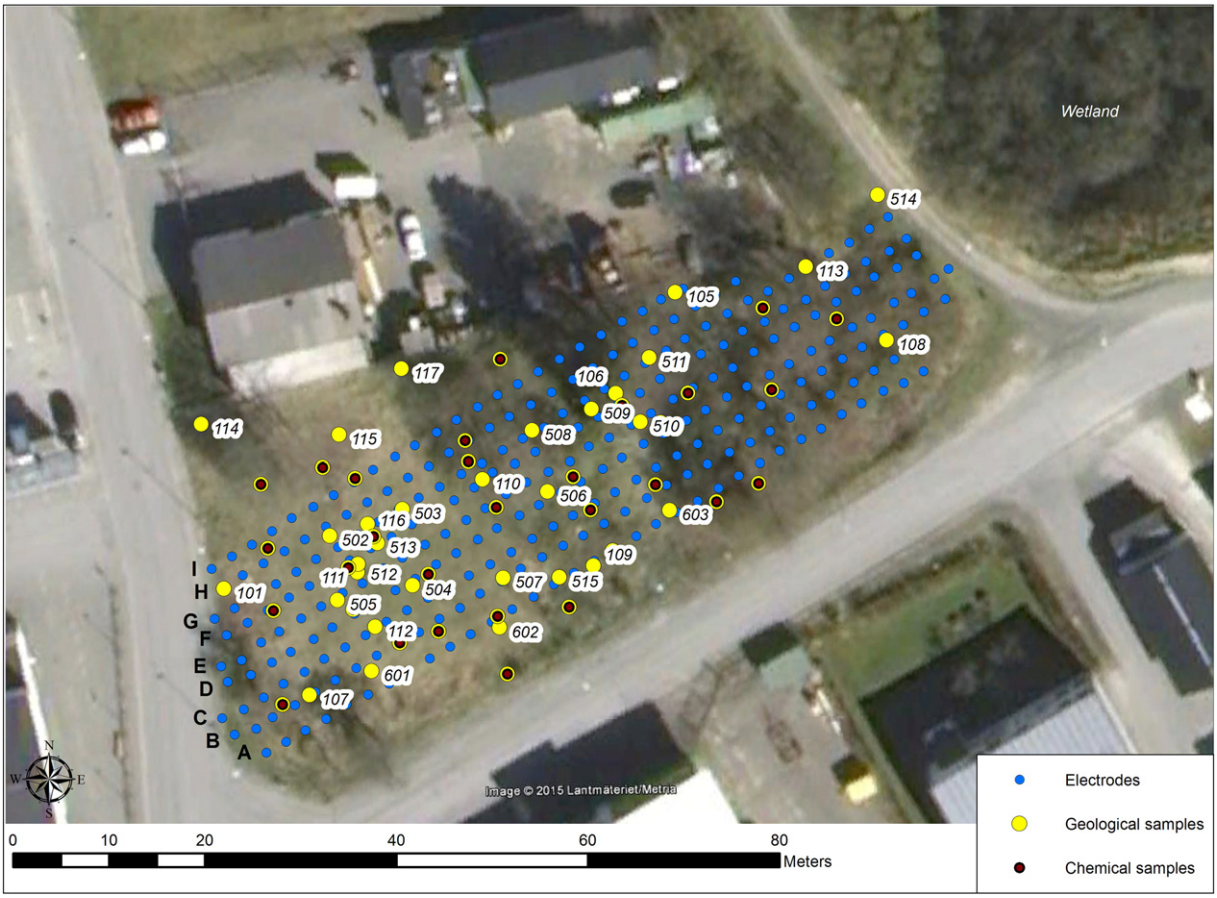

Fig. 1. Satellite image of the investigated site with the positions of the DCIP electrodes. The yellow and red markers represent previously drilled boreholes with geological classifications and chemical sampling data respectively.

in Fig. 1 were drilled during the period 2008 to 2010, using auger (100-series) and sonic (500- and 600-series) drilling methods respectively. Polyethene (PEH) wells were installed in approximately half of the 100- and 500-series boreholes, but these had been removed at the time of the DCIP survey.

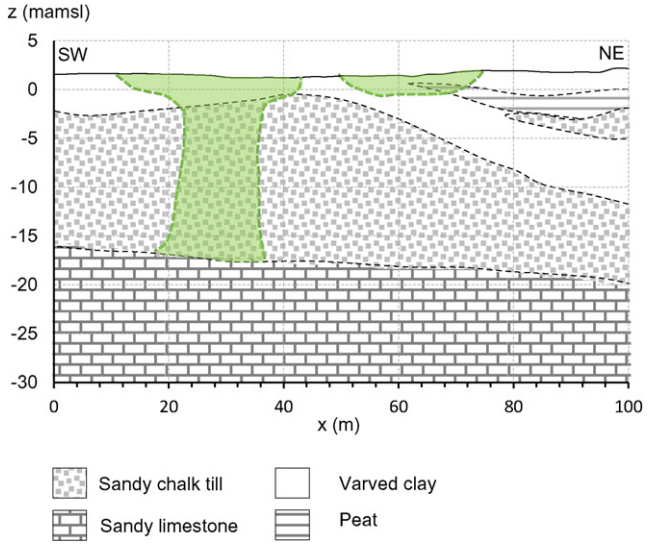

Fig. 2. Principal geological profile across the site, based on geological classifications from the boreholes in Fig. 1. The estimated extension of the free-phase contamination is also shown.

A principal sketch of the geological profile across the site is shown in Fig. 2. The general geological setting consists mainly of sandy chalk till above a bedrock of sandy limestone. At the southeastern (SE) boundary of the site, the bedrock is situated below −15 mamsl, tilting towards the northwest (NW) to below −20 mamsl. Above the till is a layer of varved clay and a thin layer of fill material. In the NW half of the site, the thickness of the clay layer increases and the clay is interspersed with layers of sand, peat and gyttja clay as the wetland is approached.

Fig. 2 also show a sketch of the estimated vertical extension of the PCE source contamination in green. The sketch is based on chemical soil sampling results (700-series, Fig. 3) performed less than a month before the DCIP measurements in 2013. The soil samples were collected from complete cores extracted from the boreholes with sonic drilling. Shortly after the core drillings, the cores were geologically classified and soil samples were taken out from different levels along the cores and sent for chemical analysis of different chlorinated hydrocarbon species. Generalized results of the chemical analyses are shown in Fig. 3, where interpolated spatial extensions and total measured amounts of PCE and its degradation product Cis-1,2-dichloroethene (Cis-1,2-DE) in the sandy chalk till (−4 to −14 mamsl) are visualized. The amounts of Cis-1,2-DE were more than 10 times higher than the first- and third order degradation products trichloroethylene (TCE) and vinyl chloride (VC), which are not visualized in Fig. 3.

The interpolated PCE surface in Fig. 3 shows the probable source area of the contamination, while the Cis-1,2-DE results indicate a main degradation zone east of the source area. High amounts of PCE and Cis-1,2-DE were also found in the upper fill- and clay layers (above −4 mamsl), as qualitatively shown in Fig. 2.

No groundwater wells were installed during the drilling campaign 2013 (700-series). Therefore, no reference data on groundwater

Fig. 3. Summarizing results from the chemical analyses of soil samples taken in the sandy chalk till (below −4 mamsl). The interpolated PCE surface show approximately the main location of the source contamination, while the interpolated Cis-1,2-DE surface indicate the main degradation zone.

chemistry at the site were available to compare with the DCIP results. However, divers installed in surrounding areas showed that the groundwater level was located at around −1.7 mamsl during the time of the DCIP measurements.

3.2. DCIP measurements

Nine parallel DCIP lines separated by 2.5 m were used to cover the site of the former dry cleaning facility (Figs. 1 and 3). The DCIP measurements were made with ABEM Terrameter LS by use of pole–dipole configuration, with an electrode spacing of 2.5 m and an average profile length of 80 m. In order to reduce capacitive coupling, a separated cable layout was used (Dahlin and Leroux, 2012). The pole–dipole configuration was used in order to gain good depth penetration in relation to the rather limited spreads, where the spread lengths were limited by the urban character of the site. An electrode spread of 80 m resulted in maximum median depth penetration of around 30 m, but as the data cover for the deepest levels is limited, the model results for the largest depths were not considered in the interpretation.

Stainless steel electrodes were used for current transmission as well as potential measurements (Dahlin et al., 2002; LaBrecque and Daily, 2008). The measurement protocols were designed to avoid using an electrode for potential measurement immediately or soon after it was used for transmitting current, in order to reduce background potential variation due to charge-up during current injection (Dahlin, 2000). Attention was devoted to securing good galvanic contact between the electrodes and ground in order to optimize data quality, where a starch based gel (Revert Optimum from Johnson Screens®) proved effective for reducing the contact resistance in coarse grained soils and fill material. Average contact resistances were thereby kept well below 1 kΩ with occasional electrodes going up to a few kΩ.

A square-wave with 1 s on- and off time was used for the measurements and full-waveform data was recorded. Logarithmically spaced IP gates were integrated over multiples of 60 ms to account for and remove train traffic disturbances at 16 2/3 Hz. The total measuring time of each decay curve was 1 s, which together with the gating provided a time domain data range corresponding to approximately 1.25–25 Hz in frequency domain.

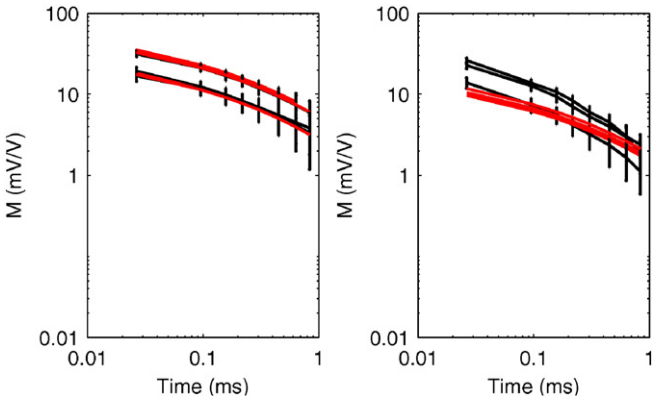

Fig. 4. Inverted decay curves (red lines) fitted to the data (black lines) during the CPA inversion. Most decays were fitted with the CPA model (left) while some decays contained spectral information neglected in the CPA inversion (right).

3.3. Data processing and inversion

The raw data was affected by urban noise but were still of an overall adequate quality. The data sets were processed, and the noisiest decay curves were removed together with some early data points which indicated coupling effects. Around 25% of the measured decay curves were removed due to low data quality.

The processed DC and full decay IP data were inverted in 2D with AarhusInv (Auken et al., 2014), following (Fiandaca et al., 2013), with both the CPA and the Cole–Cole models. In both cases, the current

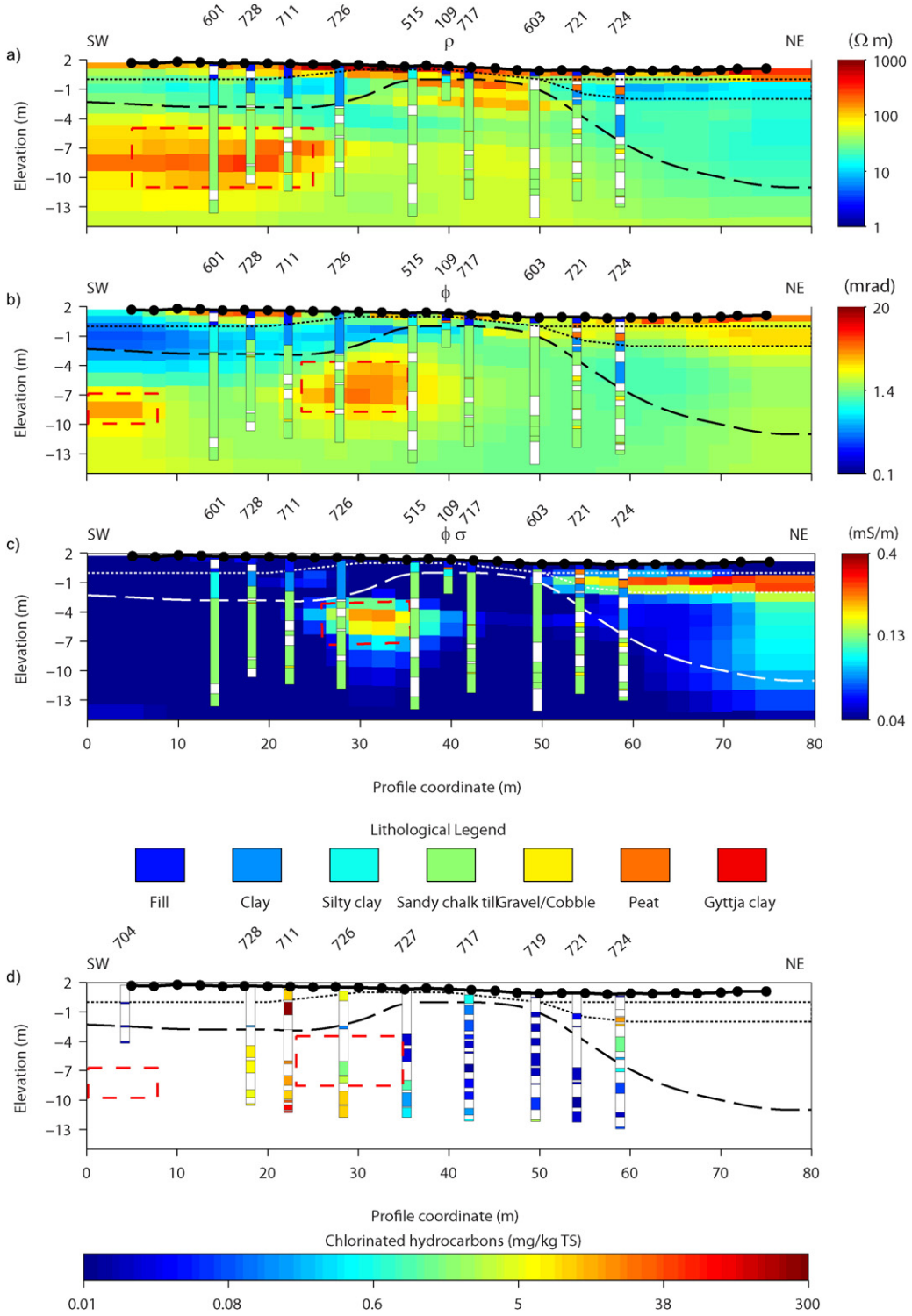

Fig. 5. CPA inverted sections of Line A with superposed geological reference data (a–c). The black dashed line represent the border between the clay layers and the sandy till, while the dotted line show the limits between fill, clay and peat layers. a) The resistivity of the sandy till is generally low with the exception of a high-resistive anomaly (red dashed line). b) The phase angle is generally low with the exception of two anomalies (red dashed lines). c) The center phase anomaly is also visible in the normalized phase angle profile (red dashed line), which indicate that it is not related to variations in groundwater chemistry. d) The chemical reference data show that the zone of highest concentrations of chlorinated hydrocarbons (boreholes 728 and 711, which indicate the PCE source zone) is located in between the phase anomalies.

waveform was modeled in the forward computations, in order to obtain inversion results not affected by the acquisition settings (Fiandaca et al., 2012). All settings used for inverting the CPA- and Cole–Cole models were identical with the exception of the parameterization.

Since the IP decays had been measured during only 1 s, it was difficult to reliably resolve the spectral parameters τ and c during the inversion. With such short acquisition times, the data were fitted at least equally as good with the CPA model. For this reason, the CPA

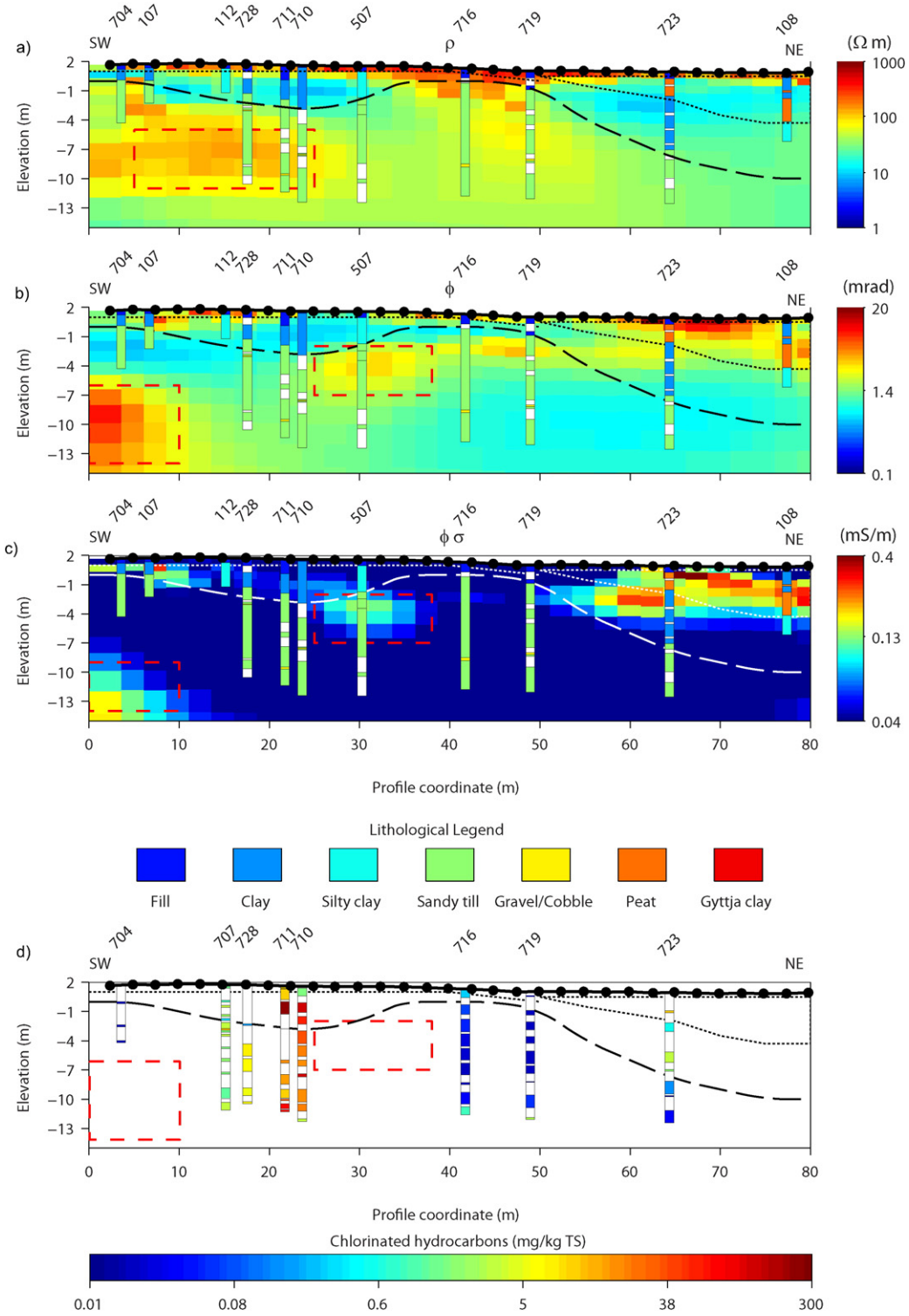

Fig. 6. CPA inverted sections of Line C with superposed geological reference data (a–c). The black dashed line represent the border between the clay layers and the sandy till, while the dotted line show the limits between fill, clay and peat layers. a) The resistivity of the sandy till is generally low with the exception of a high-resistive anomaly (red dashed line). b) The phase angle is generally low with the exception of two anomalies (red dashed lines). c) Both phase anomalies are also visible in the normalized phase angle profile (red dashed lines), which indicate that it is not related to variations in groundwater chemistry. d) The chemical reference data show that the zone of highest concentrations of chlorinated hydrocarbons (boreholes 728, 711 and 712, which indicate the PCE source zone) is located in between the phase anomalies.

inversion models will generally be shown in the following, except for one example where both inverted CPA and Cole–Cole models will be shown for comparison. The CPA models will be shown both in terms of the inverted parameters (ρ and ϕ) and of the normalized phase angle $\phi\sigma$, obtained dividing the inverted phase angle ϕ by the inverted resistivity ρ cell by cell. Fig. 4 shows qualitative examples of the fit between the data and the inverted CPA model.

4. Results

In Section 4.1, we will show results from three of the nine CPA inverted DCIP-lines; two of which were measured directly upon the source zone in the southwestern part of the site (lines A and C in Fig. 3 in Section 3.1). The third and northernmost line (Line G) is shown as a reference since only small amounts of chlorinated hydrocarbons,

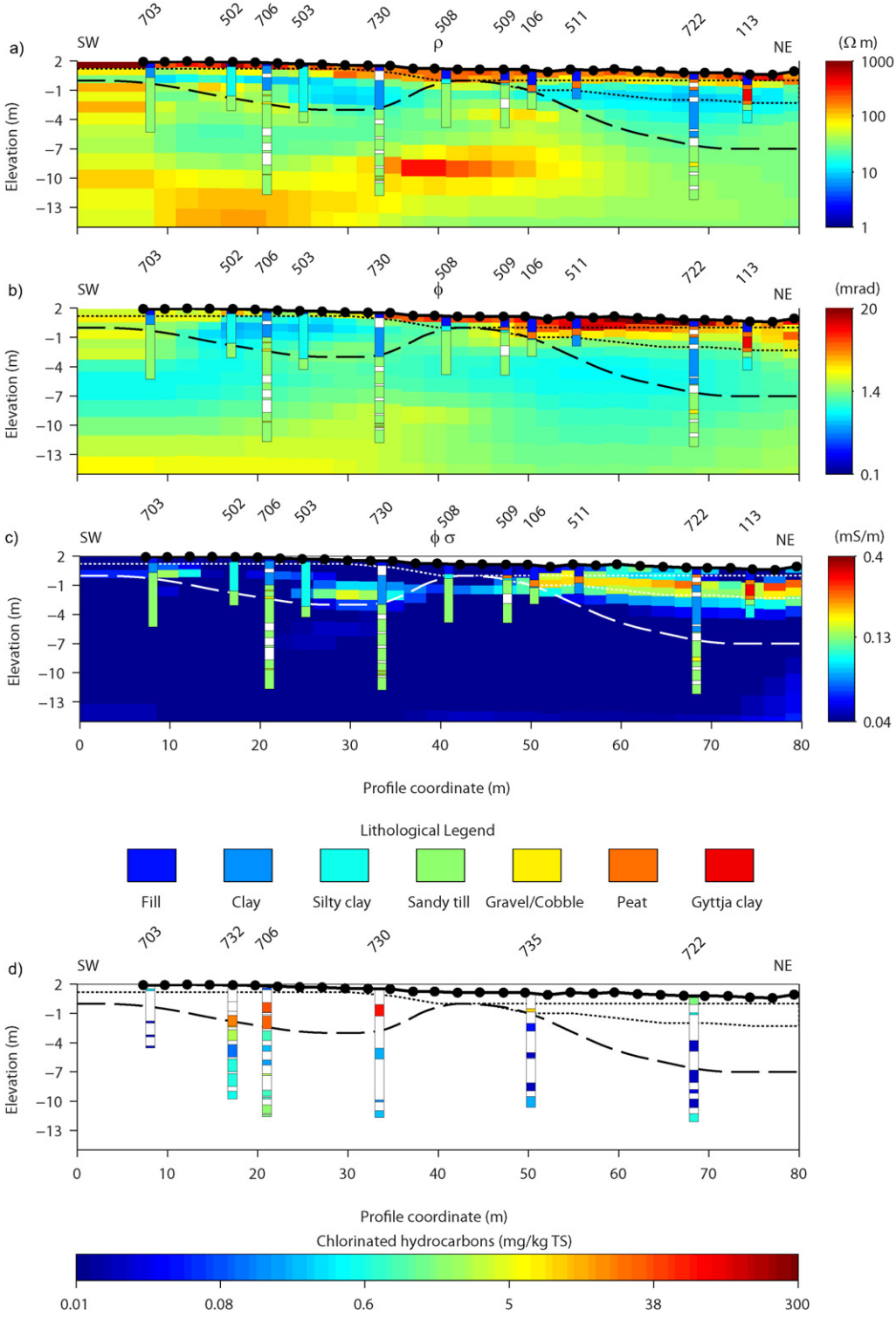

Fig. 7. CPA inverted sections of Line G with superposed geological reference data (a–c). The black dashed line represent the border between the clay layers and the sandy till, while the dotted line show the limits between fill, clay and peat layers. a) The resistivity of the sandy till is more heterogeneous compared to Lines A and C. b) The phase angle is low. c) No normalized phase angle anomalies can be distinguished in the till. d) The chemical reference data show that high concentrations of chlorinated hydrocarbons are only found in the clay layers. The low values found in the till do not seem to give rise to phase anomalies.

situated mainly in the clay layer above the till, were discovered here. In Section 4.2, we will also show results from Line A inverted with the Cole–Cole model for a comparison with the CPA results.

4.1. CPA inversion results and interpretation

Fig. 5 show the CPA inverted results from Line A together with geological reference data. Below the thin fill layer is a low resistive clay layer in the SW half of the profile, extending vertically to −4 mamsl (Fig. 5a, upper and lower limits indicated by dotted and dashed lines respectively). The vertical and horizontal extension of the clay layer is more clearly distinguishable in the phase section (Fig. 5b), where it gives rise to an anomaly of low phase. In agreement with the geological reference data, the clay layer becomes thinner from x-distance 30 m and is absent in between x-distances 40–50 m. Also in the NE part of the profile a clay layer is present beneath the fill, but here, it is interspersed with layers of peat and gyttja clay. As the wetland is approached, the layer quickly grows thicker towards the NE from x-distance 50 m towards the end of the profile (Fig. 5a, dashed line). The layer is characterized by low resistivity (Fig. 5a) and high- to intermediate phase (Fig. 5b), where the lowest resistivity and highest phase values seem to correspond to presence of peat (dotted lines in Fig. 5a-b). A discrimination between organic material and clay is effectively seen in the normalized phase section (Fig. 5c), where the layer of high normalized phase correlate well with confirmed peat presence in the reference boreholes.

Below the fill- and clay layers in Fig. 5 (the black dashed line in Fig. 5a–c), the geophysical data correspond exclusively to sandy chalk till. As can be seen in Fig. 5a, the resistivity is generally low with the exception of a high-resistive anomaly (red dashed line). The reference data do not indicate a major geological difference between the higher- and lower resistive zones in the till, but it is possible that these variations are caused by slight differences in grain size distribution that may have been overlooked during the geological classifications. The phase values in the sandy chalk till (Fig. 5b) are generally low as expected for sand and chalk. However, two clearly distinguishable anomalies with high phase values can be seen at x-distances 0–10 m and 20–35 m respectively (red dashed lines). These anomalies cannot be explained by geological variations in the till material as no e.g. clayey zones have been discovered in the sandy chalk till. Furthermore, the center anomaly is also visible in the normalized phase section (Fig. 5c), which indicate that it is not connected to variations in groundwater chemistry.

In Fig. 5d, chemical reference data from boreholes along Line A are plotted together with lines representing the geological interpretations from and the phase anomalies in the geophysical data. Just west of the center phase anomaly, the chemical reference data show that the total chlorinated hydrocarbon concentrations are at a maximum, which indicate the location of the PCE source zone (Fig. 3 in Section 3.1). The location of the source zone (Fig. 5d) correspond to high values in resistivity (Fig. 5a). However, it is uncertain if the source of the observed high resistivity is due to free-phase contamination, coarser till or a combination thereof. The center phase and normalized phase anomaly is located in a zone which is characterized by intermediate concentrations of chlorinated hydrocarbons (Fig. 5d). While the concentrations are high at the SW border of the phase anomaly, they are intermediate inside it and are becoming essentially zero beyond the NE border.

The patterns of the phase anomalies in the till in relation to chemical borehole data are consistent in all of the nine measured DCIP profiles. Phase anomalies surrounding high hydrocarbon concentrations in the

Fig. 8. Map showing the highest resistivity- and phase values in the sandy till (−4 to − 14 mamsl), obtained through interpolation of the resistivity and phase values in the CPA inverted 2D sections.

till are visible in Lines A–E. Another example is shown in Fig. 6, where the CPA inverted results from Line C are shown. The resistivity, phase and normalized phase distributions in the sandy till show patterns similar to those in Line A (Fig. 5), i.e. a high resistive anomaly coinciding with the location of the chlorinated hydrocarbon source zone (Fig. 6a, red dashed line) and a phase anomaly NE of the source zone (Fig. 6b and d, red dashed line) which is also visible in the normalized phase section (Fig. 6c). In Line C, a second strong phase anomaly located SW of the source zone is visible in both the phase and the normalized phase sections (Fig. 6b–c). Based on the location of this anomaly close to edges of the inverted sections, it is possible that it is enhanced due to border effects, but a physical cause of these anomalies cannot be ruled out.

In Lines F–I, high hydrocarbon concentrations are only found in the upper clay layer, and the IP effects in the till are generally very low. Fig. 7 shows an example of data from Line G, where the concentrations are low in the till and there is no longer an apparent phase anomaly visible below the clay layers (Fig. 7b–c). The geological stratigraphy is similar to Lines A and C according to the geological reference data, although the resistivity values are more heterogeneous compared to in Lines A and C (Fig. 7a).

High resistivity in the till where high total chlorinated hydrocarbon concentrations have been measured is visible in many of the profiles, but the resistivity anomalies do not show the same consistency in relation to the chemical data as the phase anomalies. It is probable that the high resistive anomalies are caused by both high concentrations of chlorinated hydrocarbons and/or zones of coarser till material. Gravel and cobbles have been observed locally in a few of the reference boreholes, although the major parts of the sandy chalk till consist mainly of sand-sized grains.

In Fig. 8, the CPA inverted resistivity and phase data have been interpolated between the 2D profiles, and the highest values encountered in the sandy chalk till (resistivity above 130 Ωm and phase above 3 mrad) at levels −5 to −14 mamsl have been visualized in a map. When the locations of the high-resistive anomalies in Fig. 8 are compared to the distribution of the PCE source zone in Fig. 3 (Section 3.1) some resemblance can be seen. The Cis-1,2-DE distribution NE of the PCE source zone in Fig. 3, which indicate the location of the degradation zone, correlate well with the phase anomalies in Fig. 8. The phase anomalies close to the SW border of the investigation area in Fig. 8 indicate an additional degradation zone SW of the PCE source zone. Such a widely distributed degradation zone is not indicated by the interpolated Cis-1,2-DE distribution in Fig. 3 due to a lack of chemical data between boreholes 728 and 704. However, high concentrations of Cis-1,2-DE have been measured in borehole 728 which is located just SW of the PCE source zone in Fig. 3. It is therefore likely that a degradation zone actually exist in the SW part of the site and extends beyond borehole 728, as indicated by the phase anomalies in Fig. 8.

4.2. Comparison with Cole–Cole inversions

In Fig. 9, one of the CPA inverted models shown above (Line A) is compared to the Cole–Cole inverted results of the same data. The resistivity pattern in the Cole–Cole inverted model is, as expected, similar to the pattern in the CPA inverted model (Fig. 9a). Also the location of the discussed IP anomalies in the till, i.e. high ϕ and m_0 respectively, is similar (red dashed lines in Fig. 9b). A difference between the m_0 and the ϕ sections is that the center m_0 anomaly (x-distance 25–40 m) seems to extend throughout the SW half of the Cole–Cole inverted profile, connecting to another high m_0 anomaly located at the SW border of the investigated line. The SW border anomaly is also visible in the CPA inverted ϕ section; however, it is much weaker compared to the Cole–Cole inverted m_0 section.

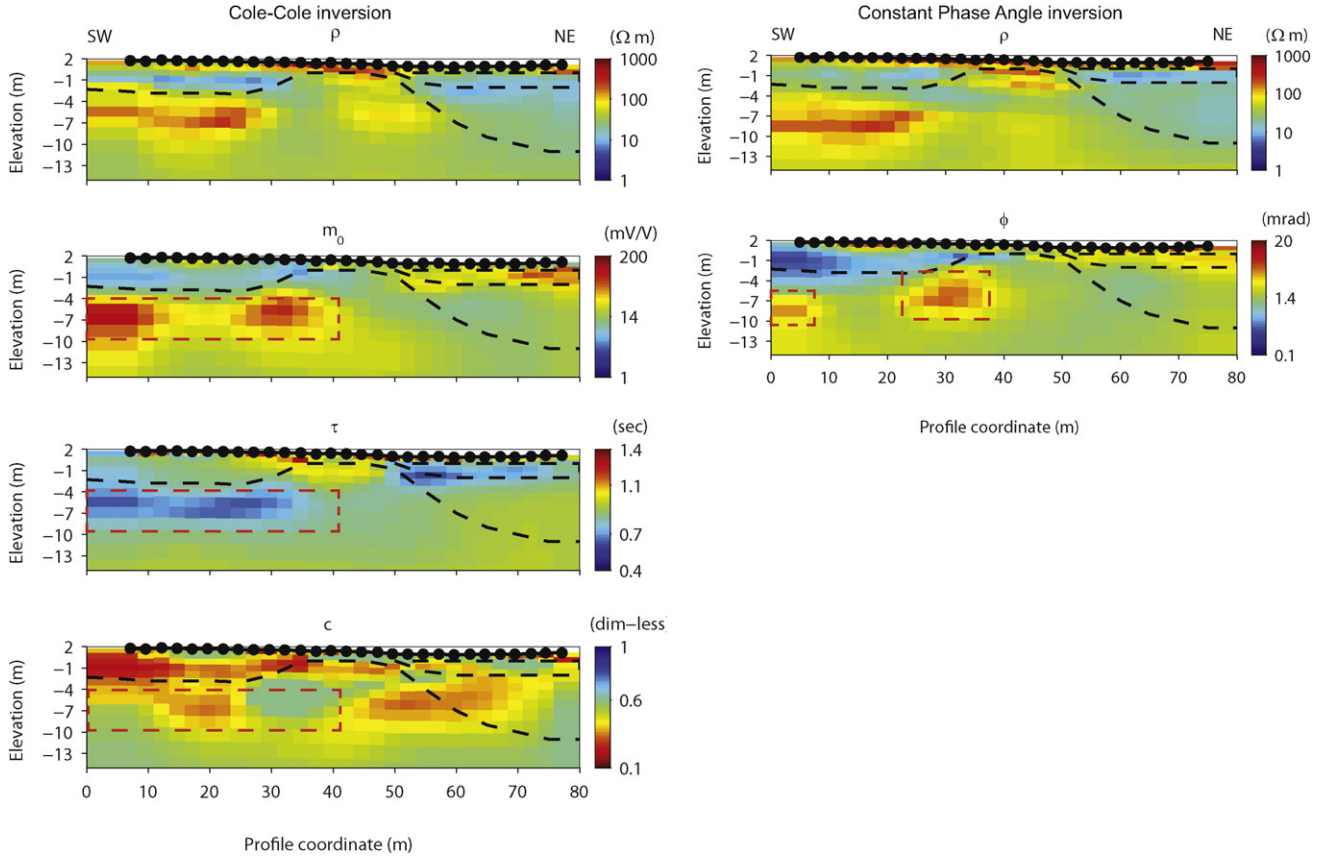

Fig. 9. Comparison of Line A inverted with the Cole–Cole model (left) and CPA model (right). The IP anomaly located east of the highest contaminated area is marked with a dashed line, and it can be seen that shorter relaxation times have been measured here compared to the surrounding till.

In Fig. 9c–d, it can be seen that the discussed m_0 anomaly seem to correspond to areas with relatively low τ and a varying c (Fig. 9b–d, red dashed lines). Where m_0 is strongest, the inverted c results are high. These patterns are consistent in all of the nine Cole–Cole inverted profiles. As mentioned in Section 3.3, the short acquisition times and noise affected IP decays resulted in an uncertainty in the inverted Cole–Cole parameters τ and c. Even so, the inverted results are good enough to provide a rough estimation of the variation of these parameters at locations where the signal-to-noise ratio is high, i.e. where m_0 is high.

Because of the general uncertainty in the spectral parameters due to the short acquisition range, we constrict our interpretation of the Cole–Cole inverted results to the fact that the discussed m_0 anomalies in the till seem to comprise low τ.

5. Discussion

The field results presented in Section 4 show that high DNAPL concentrations in the soil did not give any measurable IP response, while zones with intermediate DNAPL concentrations gave enhanced IP effects and indicated decreased τ. Considering the spatial location of the ϕ anomalies next to the source zone of free-phase PCE (Figs. 5d and 6d in Section 4.1) and with support from the chemical data in Fig. 3 (Section 3.1), we interpret these anomalies as representations of degradation zones in the outer edges of the PCE source zone. In a degradation zone, we believe that the partial degradation and dissolution of a continuous free-phase contamination can be expected to result in residual free-phase DNAPL in the soil pores. However, enhanced ϕ (or m_0) and decreased τ due to NAPL presence is in a general sense contradictory to the results from several other studies, since many of them indicate decreased IP effects (Börner et al., 1993; Vanhala et al., 1992; Vanhala, 1997; Chambers et al., 2004; Martinho et al., 2006; Schmutz et al., 2010; Revil et al., 2011) and often increased τ (Schmutz et al., 2010, 2012; Revil et al., 2011; Flores Orozco et al., 2012) in NAPL contaminated compared to clean soil. In order to explain our results, we therefore review some of the conceptual interpretation models that have been used in earlier studies, and complement them by other possible NAPL configurations that have not been discussed previously. The description of the expected IP behavior of these simplified systems will be carried out in terms of Cole–Cole parameters, since these are both effective and commonly used to describe IP spectra in both time- and frequency domain.

5.1. Conceptual models of NAPL saturated pore space

If the soil pores are essentially saturated with non-conductive free-phase NAPL, the two scenarios depictured in Fig. 10 can be considered. The configuration of NAPL around the soil grains depends on whether the geological material is water-wet or oil-wet. A discussion of the factors that determine the wettability of the interface between geological materials and NAPLs is outside the scope of this paper and can be found elsewhere (Zinszner and Pellerin, 2007). Regardless of the wettability, however, full free-phase NAPL saturation in a soil usually makes it impossible to inject current into the sample and measure the IP response in lab (e.g. Schmutz et al., 2010). On the other hand, a zone of NAPL saturated soil could in theory be detectable in field measurements as an anomaly with low m_0. Low m_0 would be the result of suppressed membrane and/or Stern layer polarization mechanisms due to the displacement of the pore water by the NAPL.

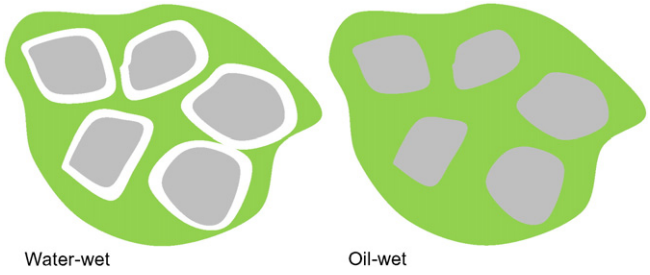

Fig. 10. Conceptual models showing the arrangement of NAPL in nearly fully saturated water-wet and oil-wet porous media. In both cases, the IP response can be expected to be absent.

5.2. Conceptual models of residual NAPL in water saturated pore space

When the soil is not fully saturated with NAPL, there is a variety of possible geometrical arrangements of the free-phase product, and we constrict ourselves here to the case of residual NAPL presence in an otherwise water-saturated pore space. The geometrical configuration of the residual NAPL depends on factors such as the wettability, the capillary pressure and the dynamic history of the NAPL in the pore space (Zinszner and Pellerin, 2007). Fig. 11 gives four different conceptual models which are possible during different circumstances, and the geometrical configurations in these models could affect measured spectral IP parameters in different ways. In model A, the NAPL is trapped in the soil pores while it in principle also could be trapped in the pore throats (model B), interconnected between several pores (model C) or coating the grain surfaces (model D). In contrast to models C and D, the effects of the conceptual models A and B on IP response or Cole–Cole parameters have not been thoroughly discussed in previous research.

5.2.1. Model A

Assuming that the NAPL is present as isolated spheres or blobs in the pores of the granular media (model A in Fig. 11), we can expect an increase in m_0. This can be explained by either the electrochemical or the membrane polarization mechanism. It has been shown that a negative surface charge arises at the interfaces between non-polar oil droplets and water, caused by adsorption of hydroxyl ions (Marinova et al., 1996). Analogous to the EDL that forms at grain-water interfaces, the water–oil interfaces will also attract counter ions, leading to the formation of polarizable EDL that can add up to a larger IP response of the soil system. A second contributing factor to increased m_0 in model A would be that a larger portion of the current flows through the EDLs of the grains compared to the conductive preferential pathways made up by free ion mobility in the water, and thus produce enhanced polarization, a process that has been described by Titov et al. (2004) for unsaturated sands. According to the electrochemical polarization mechanism, the Cole–Cole peak relaxation time τ is proportional to the dominant radius of the (assumed spherical) particles (Lesmes and Frye, 2001; Revil and Florsch, 2010). With the presence of NAPL droplets in the pores (which are smaller than the dominant grain size), it can be assumed that the dominant size of the spheres (grains and NAPL droplets) decrease, resulting in a decreased τ in the soil volume. Because of the greater range of particle sizes and relaxation times τ, the frequency factor c can also be expected to decrease. Although these effects may be likely for many natural materials with a relatively broad particle size distribution, a second peak in the frequency spectra may be more likely to appear in a very well sorted medium.

In terms of the membrane polarization mechanism, the space between the grains and the NAPL droplets can be considered as the ion selective (narrow) zone while the pore throats makes up the non-selective (wide) zones, i.e. the opposite to the situation in clean granular material where the pore throats make up the selective zones and the non-selective zones are constituted by the pores (Titov et al., 2002, 2004). Compared to a clean sample, m_0 would increase with NAPL presence since the variation ion transparency between the zones becomes larger (Titov et al., 2004). Since τ is determined by the length of the non-selective zones (Vinegar and Waxman, 1984; Titov et al., 2002) and the pore throats (i.e. grain contacts) have smaller length scales than the pores, τ can be expected to decrease in NAPL

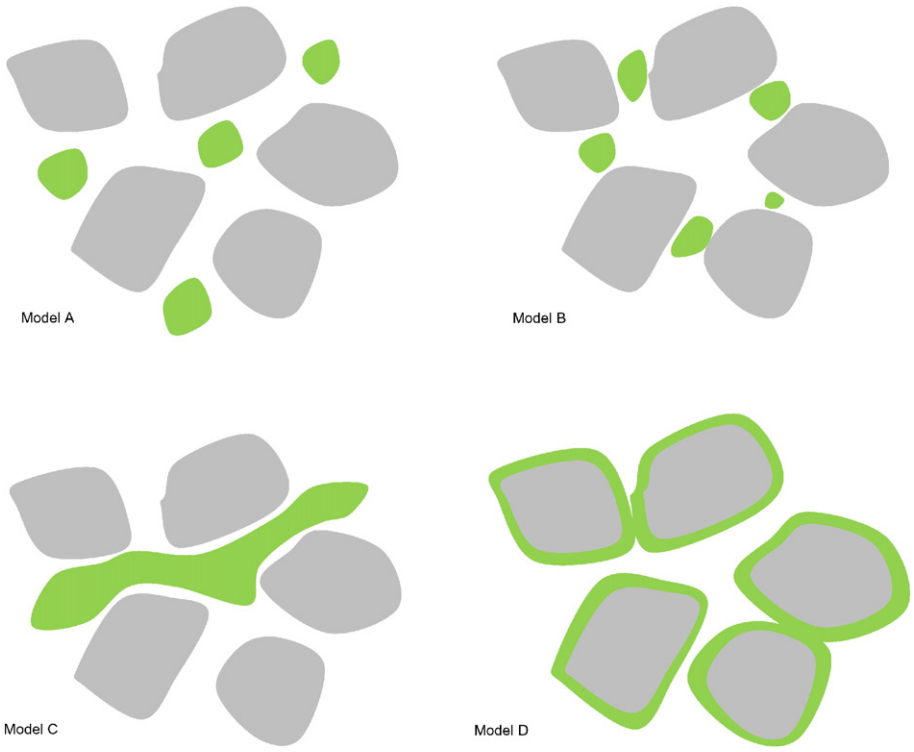

Fig. 11. Conceptual models showing possible residual NAPL configurations in water saturated porous media. Each of these configurations can be expected to affect measured IP responses in a different way. Model A: the NAPL is distributed as isolated droplets in the pores. Model B: the NAPL droplets are trapped in the pore throats. Model C: the NAPL forms a continuous phase through several pores. Model D: the NAPL is coating the grains.

contaminated soil. The frequency factor c is dependent on the distribution of non-selective zone lengths. Thus, the presence of NAPL droplets in a portion of, but not all, pores would possibly increase the dispersion of relaxation times τ.

NAPL droplets in soil pores was proposed but not discussed by Martinho et al. (2006).The NAPL configuration in model A is also similar to the conceptual model of air-filled pores in water saturated soil studied by Titov et al. (2004), who interpreted a measured increased m_0 in NAPL contaminated samples as a result of mechanisms identical to increased m_0 of unsaturated samples. However, the NAPL configuration in model A does not require that entire pore spaces are filled with NAPL, and the mechanism of NAPL displacement over water is not the same as water drainage of pores in a soil.

5.2.2. Model B

If the residual NAPL is assumed to be trapped in the pore throats (model B in Fig. 11) instead of in the pores, the electrochemical polarization mechanism would still be expected to work identically as in case A, i.e. increased m_0, decreased τ and decreased c. However, the membrane polarization mechanism would differ in this case, since the non-selective zones appear in the pore throats for both clean and contaminated samples. The chargeability m_0 would still increase by NAPL droplets due to the decreased ion transparency in the narrower pore throats, but the lengths of the non-selective zones, and consequently τ and c, would probably remain unchanged.

5.2.3. Model C

In model C (Fig. 11), it is assumed that the free-phase NAPL is interconnected between several pores and pore throats. It can be expected that part of the electrochemical polarization present in a clean sample would be short-circuited by surface conduction along the EDLs of the interconnected residual NAPL, similarly to what have been observed for clays where the microstructure results in a conductive continuum rather than unconnected and polarizable EDLs or series of alternating ion transparency (Marshall and Madden, 1959). In addition, membrane polarization effects would vanish since this mechanism requires diffusion of mobile ions in the pore fluid. The net polarization m_0 is therefore expected to decrease with NAPL presence, until the soil eventually approaches the fully NAPL-saturated case (Fig. 11) and results in a flat IP spectrum. This means that c is expected to decrease while τ is left unchanged. We believe that in the case of a NAPL configuration according to model C, the decrease in polarization magnitude would be related to an interconnected EDL of the NAPL rather than a suppression of the EDLs forming around the mineral grains.

Conceptual models similar to Figure model C (Fig. 11) have been published by Schmutz et al. (2010) and Revil et al. (2011) for the water-wet distribution of LNAPLs in the pore space. In addition, they also presented a variant on model C where the geological material is assumed to be oil-wet rather that water-wet. This condition results in a full or partial prohibition of the EDLs around the affected grains in contact with the interconnected EDL, and this conceptual model have also been presented by Flores Orozco et al. (2012).

In contradiction to our qualitative predictions above, Schmutz et al. (2010, 2012) saw an increase in σ'' with increasing LNAPL content during water-wet conditions, a result which was attributed to the decrease in water saturation. In contrast, decreased σ'' were measured by Revil et al. (2011) for oil-wet conditions as well as decreased m_0 by Flores Orozco et al. (2012) in a field study of a LNAPL spill. Revil et al. (2011) interpreted the decrease in σ'' to depend on an increased cation exchange capacity (CEC) at the oil–water interface due to presence of polar molecules in the NAPL, resulting in increased surface conduction and a disappearance of polarization length scales, while Flores Orozco et al. (2012) interpreted their observation as a result of prevented of EDL formation. In most cases, increased τ were observed in these studies (Schmutz et al., 2010, 2012; Revil et al., 2011; Flores Orozco et al., 2012), but these observations were not interpreted as a result of the NAPL configuration in model C. Therefore, these studies are not in contradiction to our expectation of unchanged τ due to the NAPL configuration

in model C. The observed effects on τ may instead be related to other superposed mechanisms, e.g. Maxwell–Wagner effects (Revil et al., 2011) or mixed NAPL configurations (Flores Orozco et al., 2012).

5.2.4. Model D

In model D (Fig. 11), it is assumed that the NAPL coats grain surfaces and thereby prohibits grain EDL formation. Martinho et al. (2006) interpreted their data in terms of model D, where organic molecules coating clay particles would explain the observed decrease in m_0 in the range 10–20% gasoline concentration in a sandy loam. Prior to Martinho et al. (2006); Olhoeft (1985) suggested a similar process whereby organic molecules attach to the clay surfaces and inhibit the cation exchange processes, given that the actual organic molecules are soluble in water. Nevertheless, Olhoeft (1985) showed that the net effect of organic contaminants on the measured ϕ was an increase, induced by unspecified chemical effects, so called clay-organic reactions.

Focusing only on the effects of the NAPL configuration, it is reasonable that a decreased m_0 can be observed for clay grains, given that their assumable high CEC would lead to a considerable stronger EDL if NAPLs are absent. On the other hand, the effect of NAPL coating on e.g. sand grains may be much more subtle and the response of m_0 is difficult to judge since it depends on the relative strength of the NAPL and grain EDLs. In terms of the electrochemical polarization mechanism, τ is expected to increase since the dominant diameters of the polarizing spheres (grain and NAPL) will increase. Assuming that not all grains are coated by NAPL, the frequency factor c could be expected to decrease.

In terms of the membrane polarization effect, it can be argued that the generally narrower zones will have a greater effect on ion transparency in the pore-throats compared to the pores, which will still mainly consist of pore fluid. Thus, the contribution of the membrane mechanism to the net polarization m_0 may be an increase. In addition, decreased τ can be expected according to the membrane mechanism since the length scale of the pores will be reduced by the NAPLs. Assuming again that not all grains are coated by NAPL, the distribution of pore lengths will increase resulting in a broader relaxation spectra and decreased c.

5.2.5. Summary

The conceptual models in Fig. 11 and the discussion above covers a wide range of possible NAPL configurations in the pore space, each expected to affect the spectral IP parameters in different ways (summarized in Table 1). However, in a real sample or field site, it is not obvious that all parts of the residual NAPL are arranged in a certain way: a combination of one or several of the conceptual models in Fig. 11 is probably possible.

Although outside the scope of this paper, it is worth mentioning that a variety of NAPL configurations could be possible also in unsaturated material where air constitutes a third phase in the pore system together with NAPL and water. For example, Shefer et al. (2013) presented a conceptual model of these conditions, where the NAPL was, as we understand it, assumed to create rings around air-filled pores by displacement of the water phase.

5.3. Interpretation of field data

In our field data, the source zone of free-phase PCE did not give rise to any ϕ anomalies. The chemical sampling results showed high concentrations of chlorinated hydrocarbons, and it is probable that the DNAPL to a large degree forms a continuous and interconnected phase in the pore space at this location (model C above).

Several decades have passed since the release of the contaminant and parts of the PCE has degraded and dissolved into the ground water. Around the borders of the continuous PCE source zone, microorganisms get access to the contaminant and use it as a carbon source. We believe that the biodegradation may fractionate the continuous PCE leading to a distribution more similar to model A above, i.e. isolated droplets in the soil pores. We have shown that the expected behavior of NAPL arranged in this way is an increase of m_0 (or ϕ), in terms of both electrochemical and membrane polarization mechanisms. This means that the enhanced IP effects that were observed outside the source zone in our field data (Figs. 5b-d, 6-d and 8) probably represent a degradation zone. This interpretation is supported by the spatial pattern of the chemical sampling results in Fig. 3 (Section 3.1) and Figs. 5 and 6 (Section 4.1), going from high concentrations to low with the main ϕ anomaly coinciding with medium concentration of chlorinated hydrocarbons. Furthermore, the Cole–Cole inversions of our field data (Fig. 8) indicated lower τ and higher c corresponding to the same ϕ anomalies. The inverted τ models also support the expected behavior of model A, although the results from the Cole–Cole inversion should be interpreted with some caution.

It should be pointed out that even though the geometrical arrangement of NAPLs in the pores is an important parameter controlling the IP response, there are also other contributing factors that could explain enhanced IP effects in a degradation zone. For example, it has been shown that microbial growth in hydrocarbon contaminated soil leads to increased IP effects, probably due to pore constriction or attachment of microbial cells around grains (Abdel Aal et al., 2006; Atekwana and Slater, 2009). Some bacterial activity can also involve iron precipitation (Atekwana and Slater, 2009) or create favorable conditions for iron sulfate precipitation by inducing groundwater chemistry changes (Flores Orozco et al., 2011). Since microbiological and groundwater chemical factors were outside the scope of this investigation, it is unknown if such effects could be possible at this specific site. Future research is needed in order to enable a discrimination between IP effects induced by the NAPL itself and possible effects of microbiological activities in a degradation zone.

The comparison between the horizontally interpolated ϕ anomalies in Fig. 8 (Section 4.1) and the interpolated chemical reference data in Fig. 3 (Section 3.1) shows an overall good agreement of the ϕ anomalies and the degradation zone (as indicated by the Cis-1,2-DE distribution). A perfect correlation cannot be expected since the drilling data do not show an absolute extension of the contaminants; in order to achieve this, the sampling would need to be even denser and cover the full length of every borehole. An interesting example is the ϕ anomaly encountered close to the SW border of the investigated site; although one borehole (728 in Fig. 3, Section 3.1) indicate a degradation zone

Table 1
Summarizing table showing the expected effects of the different NAPL distributions in Fig. 11 on the electrochemical- and membrane polarization mechanisms in terms of Cole–Cole parameters.

Conceptual model	Chargeability (m_0)		Relaxation time (τ)		Frequency factor (c)	
	Electro-chemical	Membrane	Electro-chemical	Membrane	Electro-chemical	Membrane
A	Increase	Increase	Decrease	Decrease	Decrease	Decrease
B	Increase	Increase	Decrease	Unchanged	Decrease	Unchanged
C	Decrease	Not present	Unchanged	Not present	Decrease	Not present
D	Decrease or increase	Increase	Increase	Decrease	Decrease	Decrease

going from the source zone in this direction, its extension cannot be determined due to a lack of chemical data. In addition, the scale differences between DCIP data and chemical data as well as the fact that the interpretation of the ϕ anomalies as degradation zones are based on the total amount of free-phase product in the pore space and not the NAPL species (visualized in Fig. 3), some deviations between the patterns in Figs. 3 and 8 are unavoidable.

Our inverted c models contradict our expectation of decreased c for all the discussed residual NAPL configurations. However, it is possible that the apparently high c may merely be an effect of a zone of high m_0 surrounded by natural till material with a broad τ distribution. More research is needed to investigate the IP spectra in natural soils and the relationships between lab results and the inverted spectral parameters measured in field. For field data, the possibility of choosing either the Cole–Cole or the CPA model provides a valuable flexibility in the inversion process that may be important in overcoming these scale differences.

Future research is needed to verify the expected spectral IP responses of different conceptual models (Fig. 11 and Table 1), as well as to investigate the effects of possible Maxwell–Wagner mechanisms on measurement data from NAPL contaminated soil. In order to further improve the applicability of the method in environmental projects, more research is also needed on the technical issues associated with field measurements. Full-waveform measurements in time domain are robust and time efficient, but further development is necessary in order to achieve data from the earliest times after the current switch off and cover a spectral range comparable to frequency domain measurements. However, since the IP mechanisms we are interested in usually occur at relatively low frequencies, the long acquisition times necessary for the collection of spectral IP data is probably a more challenging problem in both time- and frequency domain field measurements.

6. Conclusions

The potential of detecting NAPL with frequency- or time domain IP has been investigated in a number of lab and field studies, but the results in these studies are inconsistent and sometimes even contradictory. Different conceptual models have been proposed to explain the results from individual authors, and an overall understanding of the effects of NAPL on the porous system has not yet been achieved. In this study, we review and discuss around possible conceptual models (Section 5) and conclude that the spatial configuration of residual NAPLs in a water-saturated pore space may influence the IP mechanisms in different ways. While a decrease in chargeability or phase can be expected for some configurations, the opposite may be true for others. The NAPL configurations in different samples or field sites are often unknown, and this may to some extent explain why different results have been achieved by different authors.

In our field case, we believe that the DNAPL forms a more or less continuous phase in the pore space of the source zone leading to an absence of IP effects. The observed increase in phase and normalized phase angle next to the source zone is interpreted as a degradation zone. It is suggested that the ongoing biodegradation may have led to a fractionation of the continuous DNAPL in the outer part of the original source zone, leading to a residual presence of isolated DNAPL droplets in the soil pores. Another contributing factor to the increased IP effects may be the presence of microbial cells in the degradation zone or microbial induced changes in the geochemical environment.

In summary, an understanding of the influence of free-phase NAPLs on spectral IP parameters makes the method a promising tool to improve field delineation of NAPL contaminants in the ground. Furthermore, the ability to detect degradation zones enables monitoring of the natural biodegradation or stimulated in-situ degradation of NAPL spills.

Acknowledgments

We would like to thank the two anonymous reviewers who helped to improve the quality and clarity of the paper. We also thank our project colleagues and field co-workers Per-Ivar Olsson, Marcus Wennermark, Carl-Henrik Månsson and Mikael Lumetzberger. Funding for the work was provided by Formas — The Swedish Research Council for Environment, Agricultural Sciences and Spatial Planning, (ref. 2012-1931), BeFo — Swedish Rock Engineering Research Foundation, (ref. 331), SBUF — The Development Fund of the Swedish Construction Industry, (ref. 12719) and Sven Tyréns Stiftelse (ref. 921456 3.81). The project is part of the Geoinfra-TRUST framework (http://trust-geoinfra.se/).

References

Abdel Aal, G.Z., Slater, L.D., Atekwana, E.A., 2006. Induced-polarization measurements on unconsolidated sediments from a site of active hydrocarbon biodegradation. Geophysics 71 (2), H13–H24 (Available at: http://library.seg.org/doi/abs/10.1190/1.2187760).

Ajo-Franklin, J.B., Geller, J.T., Harris, J.M., 2006. A survey of the geophysical properties of chlorinated DNAPLs. J. Appl. Geophys. 59 (3), 177–189 (Available at: http://linkinghub.elsevier.com/retrieve/pii/S0926985105000868, Accessed January 8, 2014).

Atekwana, E.A., Atekwana, E.A., 2010. Geophysical signatures of microbial activity at hydrocarbon contaminated sites: a review. Surv. Geophys. 31 (2), 247–283 (Available at: http://link.springer.com/10.1007/s10712-009-9089-8, Accessed April 28, 2014).

Atekwana, E.A., Slater, L.D., 2009. Biogeophysics: a new frontier in earth science research. Rev. Geophys. 47 (4), 1–30 (Available at: http://www.agu.org/pubs/crossref/2009/2009RG000285.shtml, Accessed July 1, 2013).

Auken, E., Christiansen, A.V., Kirkegaard, C., Fiandaca, G., Schamper, C., Behroozmand, A.A., Binley, A., Nielsen, E., Effersø, F., Christensen, N.V., Sørensen, K., Foged, N., Vignoli, G., 2014. An overview of a highly versatile forward and stable inverse algorithm for airborne, ground-based and borehole electromagnetic and electric data. Explor. Geophys. 1–13 (Available at: http://dx.doi.org/10.1071/EG13097).

Binley, A., Slater, L.D., Fukes, M., Cassiani, G., 2005. Relationship between spectral induced polarization and hydraulic properties of saturated and unsaturated sandstone. Water Resour. Res. 41 (12) (p. n/a–n/a. Available at: http://doi.wiley.com/10.1029/2005WR004202, Accessed August 30, 2013).

Börner, F., Gruhne, M., Schön, J., 1993. Contamination indications derived from electrical properties in the low frequency range. Geophys. Prospect. 41 (1), 83–98.

Cassiani, G., Kemna, A., Villa, A., Zimmermann, E., 2009. Spectral induced polarization for the characterization of free-phase hydrocarbon contamination of sediments with low clay content. Near Surf. Geophys. 7 (5–6), 547–562.

Chambers, J.E., Loke, M.H., Ogilvy, R.D., Meldrum, P.I., 2004. Non-invasive monitoring of DNAPL migration through a saturated porous medium using electrical impedance tomography. J. Contam. Hydrol. 68, 1–22.

Cole, K.S., Cole, R.H., 1941. Dispersion and absorption in dielectrics I. Alternating current characteristics. J. Chem. Phys. 9 (4), 341 (Available at: http://scitation.aip.org/content/aip/journal/jcp/9/4/10.1063/1.1750906, Accessed March 22, 2014).

Dahlin, T., 2000. Short note on electrode charge-up effects in DC resistivity data acquisition using multi electrode arrays. Geophys. Prospect. 48 (1), 181–187.

Dahlin, T., Leroux, V., 2012. Improvement in time-domain induced polarization data quality with multi-electrode systems by separating current and potential cables. Near Surf. Geophys. 545–565 (Available at: http://nsg.eage.org/publication/publicationdetails/?publication=65633, Accessed December 3, 2013).

Dahlin, T., Leroux, V., Nissen, J., 2002. Measuring techniques in induced polarisation imaging. J. Appl. Geophys. 50 (3), 279–298.

De Lima, O.A.L., Sharma, M.M., 1992. A generalized Maxwell–Wagner theory for membrane polarization in shaly sands. Geophysics 57 (3), 431–440 (Available at: http://library.seg.org/doi/abs/10.1190/1.1443257).

Deceuster, J., Kaufmann, O., 2012. Improving the delineation of hydrocarbon-impacted soils and water through induced polarization (IP) tomographies: a field study at an industrial waste land. J. Contam. Hydrol. 136–137 (August 2012), 25–42 (Available at: http://www.ncbi.nlm.nih.gov/pubmed/22659399, Accessed August 5, 2013).

Fiandaca, G., Auken, E., Christiansen, A.V., Gazoty, A., 2012. Time-domain-induced polarization: full-decay forward modeling and 1D laterally constrained inversion of Cole–Cole parameters. Geophysics 77 (3), E213–E225 (Available at: http://library.seg.org/doi/abs/10.1190/geo2011-0217.1).

Fiandaca, G., Ramm, J., Binley, A., Gazoty, A., Christiansen, A.V., Auken, E., 2013. Resolving spectral information from time domain induced polarization data through 2-D inversion. Geophys. J. Int. 192 (2), 631–646 (Available at: http://gji.oxfordjournals.org/cgi/doi/10.1093/gji/ggs060. Accessed August 5, 2013).

Flores Orozco, A., Williams, K.H., Long, P.E., Hubbard, S.S., Kemna, A., 2011. Using complex resistivity imaging to infer biogeochemical processes associated with bioremediation of an uranium-contaminated aquifer. J. Geophys. Res. Biogeosci. 116 (3), 1–17.

Flores Orozco, A., Kemna, A., Oberdörster, C., Zschornack, L., Leven, C., Dietrich, P., et al., 2012. Delineation of subsurface hydrocarbon contamination at a former hydrogenation plant using spectral induced polarization imaging. J. Contam. Hydrol. 136–137, 131–144 (Available at: http://www.ncbi.nlm.nih.gov/pubmed/22784635 Accessed May 13, 2014).

LaBrecque, D., Daily, W., 2008. Assessment of measurement errors for galvanic-resistivity electrodes of different composition. Geophysics 73 (2), F55–F64.

Leroy, P., Revil, A., 2009. A mechanistic model for the spectral induced polarization of clay materials. J. Geophys. Res. Solid Earth 114 (B10).
Leroy, P., Revil, A., Kemna, A., Cosenza, P., Ghorbani, A., 2008. Complex conductivity of water-saturated packs of glass beads. J. Colloid Interface Sci. 321 (1), 103–117 (Available at: http://www.ncbi.nlm.nih.gov/pubmed/18272167, Accessed May 29, 2013).
Lesmes, D.P., Frye, K.M., 2001. Influence of pore fluid chemistry on the complex conductivity and induced polarization responses of Berea sandstone. J. Geophys. Res. 106 (B3), 4079–4090.
Lesmes, D.P., Morgan, F.D., 2001. Dielectric spectroscopy of sedimentary rocks. J. Geophys. Res. 106 (B7), 13329–13346.
Marinova, K.G., Alargova, R.G., Denkov, N.D., Velev, O.D., Petsev, D.N., Ivanov, I.B., et al., 1996. Charging of oil–water interfaces due to spontaneous adsorption of hydroxyl ions. Langmuir 12 (8), 2045–2051.
Marshall, D.J., Madden, T.R., 1959. Induced polarization, a study of its causes. Geophysics XXIV (4), 790–816.
Martinho, E., Almeida, F., Senos Matias, M.J., 2006. An experimental study of organic pollutant effects on time domain induced polarization measurements. J. Appl. Geophys. 60 (1), 27–40 (Available at: http://linkinghub.elsevier.com/retrieve/pii/S092698510500100X, Accessed November 14, 2014).
Naudet, V., Gourry, J.C., Girard, F., Mathieu, F., Saada, A., 2014. 3D electrical resistivity tomography to locate DNAPL contamination around a housing estate. Near Surf. Geophys. 12 (3), 351–360 (Available at: http://nsg.eage.org/publication/publicationdetails/?publication=75347, Accessed November 14, 2014).
Nordsiek, S., Weller, A., 2008. A new approach to fitting induced-polarization spectra. Geophysics 73 (6), F235–F245 (Available at: http://library.seg.org/doi/abs/10.1190/1.2987412).
Olhoeft, G.R., 1985. Low frequency electrical properties. Geophysics 50 (12), 2492–2503 (Available at: http://library.seg.org/doi/abs/10.1190/1.1441880).
Pelton, W.H., Ward, S.H., Hallof, P.G., Sill, W.R., Nelson, P.H., 1978. Mineral discrimination and removal of inductive coupling with multifrequency IP. Geophysics 43 (3), 588–609.
Power, C., Gerhard, J.I., Tsourlos, P., Soupios, P., Simyrdanis, K., Karaoulis, M., 2015. Improved time-lapse electrical resistivity tomography monitoring of dense non-aqueous phase liquids with surface-to-horizontal borehole arrays. J. Appl. Geophys. 112 (January 2015), 1–13 (Available at: http://linkinghub.elsevier.com/retrieve/pii/S0926985114003164).
Revil, A., Florsch, N., 2010. Determination of permeability from spectral induced polarization in granular media. Geophys. J. Int. 1480–1498 (Available at: http://gji.oxfordjournals.org/cgi/doi/10.1111/j.1365-246X.2010.04573.x, Accessed March 15, 2013).
Revil, A., Schmutz, M., Batzle, M.L., 2011. Influence of oil wettability upon spectral induced polarization of oil-bearing sands. Geophysics 76 (5), A31–A36 (Available at: http://library.seg.org/doi/abs/10.1190/geo2011-0006.1).
Schmutz, M., Revil, A., Vaudelet, P., Batzle, M., Viñao, P.F., Werkema, D.D., 2010. Influence of oil saturation upon spectral induced polarization of oil-bearing sands. Geophys. J. Int. 183 (1), 211–224 (Available at: http://gji.oxfordjournals.org/cgi/doi/10.1111/j.1365-246X.2010.04751.x, Accessed April 28, 2014).
Schmutz, M., Blondel, A., Revil, A., 2012. Saturation dependence of the quadrature conductivity of oil-bearing sands. Geophys. Res. Lett. 39 (3) (Available at: http://doi.wiley.com/10.1029/2011GL050474, Accessed June 11, 2013).
Schwarz, G., 1962. A theory of the low-frequency dielectric dispersion of colloidal particles in electrolyte solution. J. Phys. Chem. 66 (12), 2636–2642.
Scott, J.B.T., Barker, R.D., 2003. Determining pore-throat size in Permo-Triassic sandstones from low-frequency electrical spectroscopy. Geophys. Res. Lett. 30 (9) (Available at: http://doi.wiley.com/10.1029/2003GL016951, Accessed June 11, 2013).
Seigel, H.O., 1959. Mathematical formulation and type curves for induced polarization. Geophysics XXIV (3), 547–565.
Shefer, I., Schwartz, N., Furman, A., 2013. The effect of free-phase NAPL on the spectral induced polarization signature of variably saturated soil. Water Resour. Res. 49 (10), 6229–6237 (Available at: http://doi.wiley.com/10.1002/wrcr.20502 Accessed October 7, 2013).
Slater, L., 2002. Electrical-hydraulic relationships observed for unconsolidated sediments. Water Resour. Res. 38 (10), 1–13 (Available at: http://www.agu.org/pubs/crossref/2002/2001WR001075.shtml).
Slater, L., 2007. Near surface electrical characterization of hydraulic conductivity: from petrophysical properties to aquifer geometries—a review. Surv. Geophys. 28 (2–3), 169–197 (Available at: http://link.springer.com/10.1007/s10712-007-9022-y, Accessed May 2, 2013).
Slater, L., Lesmes, D.P., 2002a. Electrical-hydraulic relationships observed for unconsolidated sediments. Water Resour. Res. 38 (10), 1–13 (Available at: http://www.agu.org/pubs/crossref/2002/2001WR001075.shtml).
Slater, L.D., Lesmes, D., 2002b. IP interpretation in environmental investigations. Geophysics 67 (1), 77–88 (Available at: http://link.aip.org/link/GPYSA7/v67/i1/p77/s1&Agg=doi).
Titov, K., Komarov, V., Tarasov, V., Levitski, A., 2002. Theoretical and experimental study of time domain-induced polarization in water-saturated sands. J. Appl. Geophys. 50 (4), 417–433.
Titov, K., Kemna, A., Tarasov, A., Vereecken, H., 2004. Induced polarization of unsaturated sands determined through time domain measurements. Vadose Zone J. 3 (4), 1160–1168.
Titov, K., Tarasov, A., Ilyin, Y., Seleznev, N., Boyd, A., 2010. Relationships between induced polarization relaxation time and hydraulic properties of sandstone. Geophys. J. Int. 180 (3), 1095–1106 (Available at: http://gji.oxfordjournals.org/cgi/doi/10.1111/j.1365-246X.2009.04465.x, Accessed June 14, 2013).
Van Voorhis, G.D., Nelson, P.H., Drake, T.L., 1973. Complex resistivity spectra of porphyry copper mineralization. Geophysics 38 (1), 49–60.
Vanhala, H., 1997. Mapping oil-contaminated sand and till with the spectral induced polarization (SIP) method. Geophys. Prospect. 45 (2), 303–326.
Vanhala, H., Soininen, H., Kukkonen, I., 1992. Detecting organic chemical contaminants by spectral induced polarization method in glacial till environment. Geophysics 57 (8), 1014–1017 (Available at: http://library.seg.org/doi/abs/10.1190/1.1443312).
Vinegar, H.J., Waxman, M.H., 1984. Induced polarization of shaly sands. Geophysics 49 (8), 1267–1287 (Available at: http://library.seg.org/doi/abs/10.1190/1.1441755).
Zinszner, B., Pellerin, F.M., 2007. A Geoscientist's Guide to Petrophysics. Editions Technip, Paris.

Paper II

Johansson, S., Sparrenbom, C., Fiandaca, G., Lindskog, A., Olsson P.I, Dahlin, T. and Rosqvist, H.

Investigations of a Cretaceous limestone with spectral induced polarization and scanning electron microscopy

Submitted for publication (Geophysical Journal International)

Investigations of a Cretaceous limestone with spectral induced polarization and scanning electron microscopy

Johansson, S.[1,4], Sparrenbom, C.[2], Fiandaca, G.[3], Lindskog, A.[2], Olsson, P.I.[1], Dahlin, T.[1], Rosqvist, H[4]

[1]Division of Engineering Geology, Lund University, Lund, Sweden. Email: sara.johansson@tg.lth.se
[2]Department of Geology, Lund University, Lund, Sweden
[3]Department of Geoscience, Aarhus University, Denmark
[4]Tyréns AB, Malmö, Sweden

SUMMARY

Characterization of varying bedrock properties is a common need in various contexts, ranging from large infrastructure pre-investigations to environmental protection. A direct current resistivity and time domain induced polarization (IP) survey aiming to characterize varying properties of a Cretaceous limestone was carried out in the Kristianstad basin, Sweden. The time domain IP data was processed and inverted for spectral Cole-Cole parameters. The inverted sections showed variations within the limestone that are probably caused by variations in texture and composition. Spectral IP anomalies in limestones have not been frequently investigated in previous research, and the aim of this paper is to investigate which kinds of largescale structures and microgeometrical properties that are likely to result in the observed variations within the limestone. Samples from a deep drilling in the Kristianstad basin were investigated with Scanning Electron Microscopy and Energy Dispersive X-ray Spectroscopy. The results showed that varying amounts of pyrite, glauconite and clay matrix were present at different levels in the limestone. These minerals could explain local high IP anomalies in the limestone, in which the IP responses otherwise are generally weak. There were also differences in the texture of the limestone at different levels, governed by fossil shapes and composition, proportions of calcite cement and micritic matrix as well as amount of silicate grains. Textural variations may have implications on the variation in Cole-Cole relaxation time and frequency factor. However, more research is needed in order to directly connect microgeometrical properties in limestone to spectral IP responses. The results from this study show that it is possible to recover useable spectral information from early decay times. We also show that under certain conditions (e.g. relatively short relaxation times in the subsurface), it is possible to extract spectral information from time domain IP data measured with as short on-off times as 1s.

Key words: Microstructures; Electrical Properties; Tomography; Geomorphology

INTRODUCTION

Characterization of varying bedrock properties is a common need in various contexts, ranging from large subsurface infrastructure investigations to various concerns regarding environmental protection. Rock quality estimations and mapping of the bedrock topography are examples of important geotechnical considerations, while porosity, bedrock fracturing, permeability and groundwater salinity are some of the parameters needed for groundwater modelling and hydrogeological analyses.

Due to the sensitivity of the resistivity method to variations in groundwater content and groundwater salinity, the method has proven to be a useful tool to map variations in bedrock properties (e.g. Danielsen & Dahlin 2009; Ganerød et al. 2006; Cavinato et al. 2006). Additional information on materials or structures in the bedrock, which might not display a variation in resistivity, can be obtained by measurements of induced polarization (IP). In contrast to resistivity, IP is sensitive to microgeometrical surface properties and to certain kinds of minerals (e.g. Slater & Lesmes 2002b; Kemna et al. 2012), and the measurements can in a convenient way be performed simultaneously with the resistivity surveying. For example, previous measurements on crystalline bedrock or sandstones have shown that anomalies of low resistivity and high chargeability can correspond to clay weathered fracture zones (Marescot et al. 2008; Magnusson et al. 2010).

A direct current resistivity and time domain induced polarization (DCIP) survey aiming to characterize varying bedrock properties was carried out in the vicinity of a highly contaminated site in Kristianstad, southern Sweden (herein referred to as the main survey area). The main purpose of the DCIP bedrock characterization was to obtain a hydrogeological conception of the surroundings and identify possible preferential pathways for migration of contaminated water. The investigated site is situated upon a regional depression in the Precambrian gneiss and granite bedrock, where glauconitic sand and limestone have been deposited during the Cretaceous period. In a limestone bedrock, preferential paths for groundwater transport may be due to either fractured zones, karst formation or porosity variations caused by differences in the genesis of the limestone. However, in contradiction

to many other types of sedimentary and crystalline rocks mainly consisting of silicates, clay mineral precipitation is naturally limited in the weathering of limestone.

The time domain IP data were processed and inverted for spectral Cole-Cole parameters. The inverted sections showed variations within the limestone, which are probably caused by variations in texture and composition. The aim of the current study is to investigate which kinds of largescale structures and microgeometrical properties that are likely to result in the observed variations in the limestone. Spectral IP anomalies in limestones have not been frequently investigated in previous research, and it is therefore of interest to examine probable sources of the variations observed within the limestone bedrock in this survey. Since little is known about spectral IP responses and mechanisms in different kinds of limestones, the results presented in this study can enhance the interpretation of future IP surveys in similar geological environments.

METHODS AND MATERIALS

Regional geology

The investigated site is situated in a region in the northeastern part of the province Skåne in southern Sweden, where Cretaceous limestone has been deposited in a depression within the Precambrian gneiss and granite bedrock. The depression, referred to as the Kristianstad basin (Figs 1 and 2), was formed by weathering and kaolinization in the Jurassic period and is bounded towards the southwest by horst structures. The weathering led to a highly uneven topography of the Precambrian gneiss and granite bedrock, which can be found at depths down to around 300 meters (Christensen 1984; Kornfält et al. 1978).

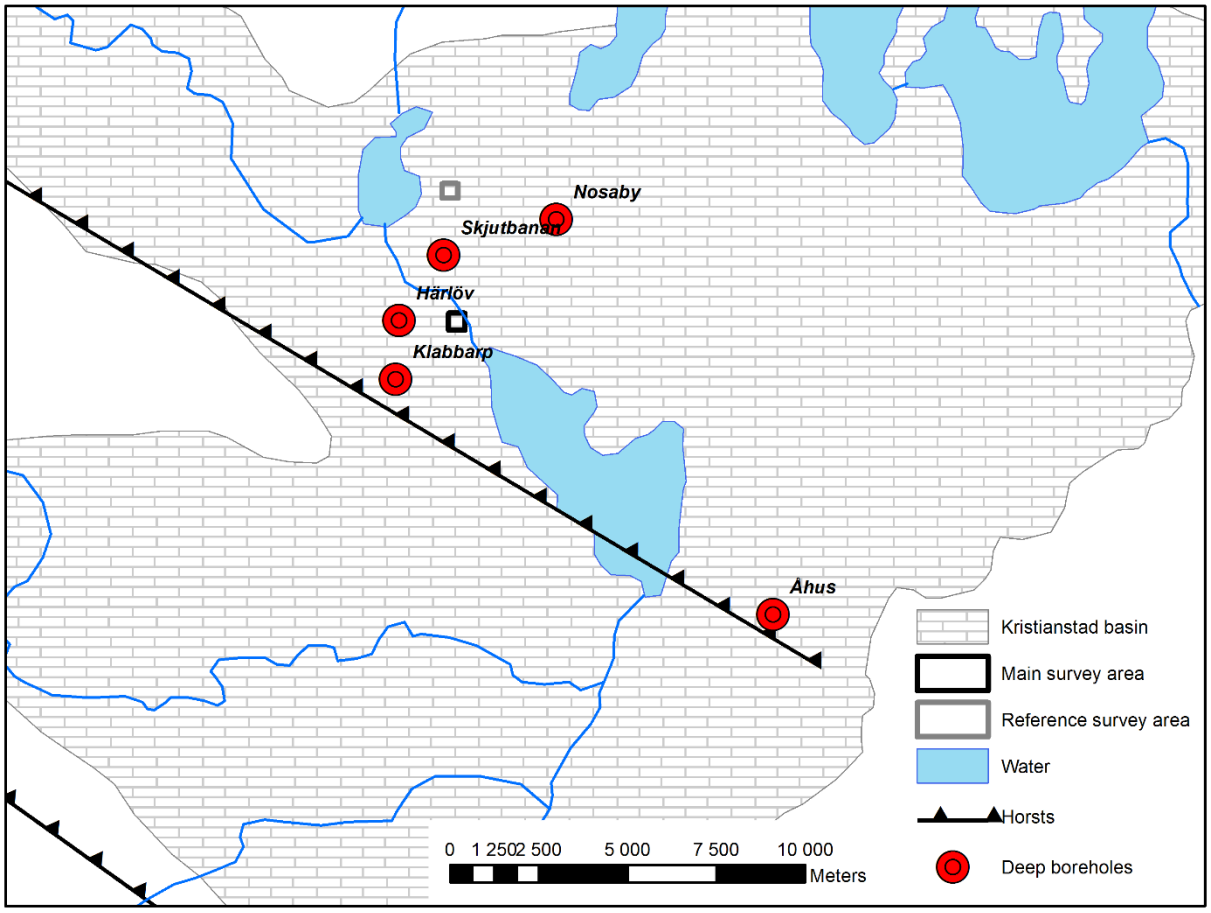

Figure 1. A horizontal map of the Kristianstad basin with horsts according to Christensen (1984). The locations of the main and reference survey areas are drawn in the map together with the deep drilled reference data available in literature (Kornfält et al. 1978) and accessed from the Åhus drilling.

A conceptual geological profile of the region is shown in Fig. 2. Considerable relief for the different bedrock surfaces have been observed all over the Kristianstad basin, and the thicknesses of the different formations show large local variations (Gustafsson et al. 1979).

A poorly lithified and often glauconite rich sandstone rest upon the Precambrian bedrock. The glauconitic sandstone has been formed in a sea bottom environment with relatively high water levels (Kornfält et al. 1978), and it is overlain by the Cretateous limestone. Several transgressions and regressions occurred during the Upper Cretateous period, and the limestone consists to a large degree of carbonate fossil fragments that have been deposited in mainly shallow marine environments. The limestone deposits vary between sandy limestone to calcareous sandstone, with skeletal carbonate grain sizes ranging from silt and sand to coarser material (Christensen 1984). On top of the Cretaceous limestone Quaternary deposits are found. These consist of Quaternary tills, glacial clay, glacifluvial sand and gravel and postglacial sand.

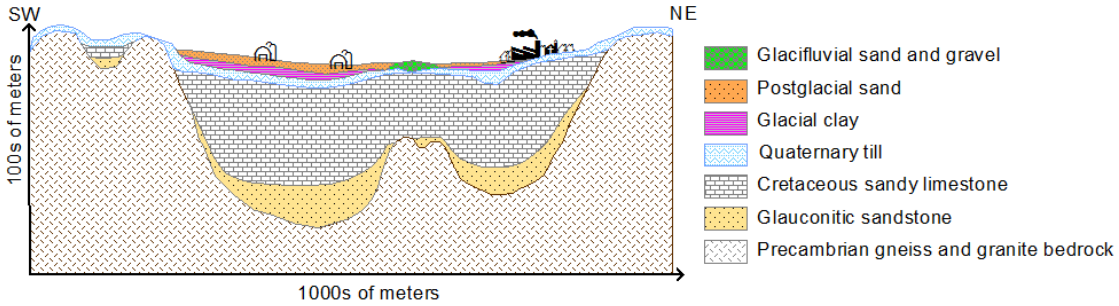

Figure 2. A Conceptual sketch of the main geological units in the area. Drawn freely from SW towards NE.

DCIP survey

In an extended area surrounding the former dry cleaning facility, four 205m long 2D DCIP sections were measured (Fig. 3). The aim was to provide a geological interpretation including possible preferential pathways for contaminated groundwater. The electrode configuration pole-dipole was used here, motivated by the fact that it provides a large depth penetration in combination with a good spatial resolution (Dahlin & Zhou 2004).

The actual dry cleaning facility with the source contamination was located in the area between Lines 2 and 3 (red area in Fig. 3). The source contamination was also investigated with DCIP during the same field campaign, but with a different objective and a different measurement arrangement, i.e., a small scale survey. The aim of the small scale survey was to investigate the possibilities of detecting the source contamination, and results from these measurements are reported in Johansson et al. (2015). The boreholes marked with yellow dots in Fig. 3 were drilled down to 10-30 meters below the ground surface prior to the DCIP investigation. The main purpose of the drilling was to determine groundwater contamination levels and the level of the limestone bedrock surface, although the latter was unsuccessful at many locations due to difficult drilling conditions. The limestone surface was interpreted as weathered at locations where it was difficult to determine.

A separated cable layout for injecting current and measuring potential was used (Dahlin & Leroux 2012) in order to reduce capacitive coupling effects, and a low electrode contact resistance was assured. Acid grade stainless steel electrodes were installed with an in-line spacing of 2.5m, and electrode contact resistance was reduced when necessary by adding a starch-water mixture to the soil next to the electrodes. An ABEM Terrameter LS was used for transmitting current and measuring potentials, and the switching capability of the instrument was increased by using the ES10-64 external relay switch. The on- and off times of the current pulses were 1s, corresponding to a square wave fundamental frequency of 0.25Hz. Full waveform data was collected with a sample rate of 1000Hz.

As can be seen in Fig. 3, the site has an urban character that makes measurements with electrical methods challenging. Power line and train traffic noise at frequencies of 50Hz and 16 2/3Hz were identified in the DCIP raw data. In addition to problems with noise affected data, urban structures such as buried infrastructure pipes and buildings can lead to anomalies and 3D-effects in the inverted data models. During the interpretation it was therefore important to be able to separate urban from geological sources for the anomalies.

In addition to the DCIP sections measured in the main survey area, a reference DCIP section was also measured with the same measurement setup and settings. The reference line was located at a distance of approximately 4 km north of the main survey area, in a rural environment that was assumed to be free from both urban noise and groundwater contamination. The locations of the main and reference survey areas in the Kristianstad basin are shown in Fig. 1. Also shown in this Fig. 1 are deep drillings which have been used as reference data for the interpretation of the DCIP results.

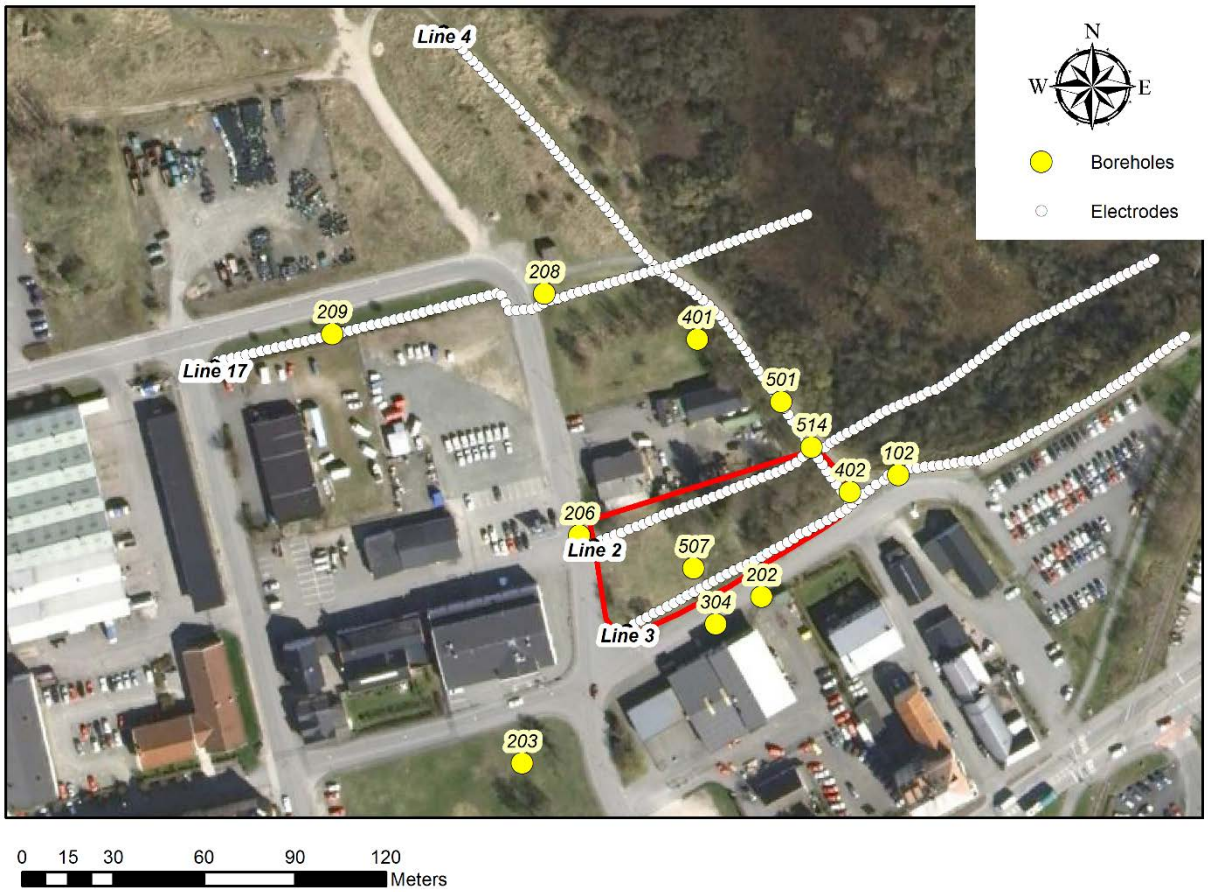

Figure 3. Satellite image showing the investigated surroundings of the dry cleaning site, which is situated between Line 2 and Line 3 (red area).

Data processing and inversion

The chosen IP gates of the acquired data were multiples of 60ms in order to supress the periodic noise from the power line and train traffic frequencies. A drawback of this method is that data from early decay times (<40ms) are removed, which might reduce the magnitude of the inverted chargeability. A recently developed processing scheme (Olsson et al. 2016) was used to recover IP decay data from early times and increase the spectral IP information content. This processing scheme applies a model based harmonic denoising for supressing the periodic noise which reduces the need for long (60ms) gates and makes it is possible to retrieve the decay information from one to two milliseconds after the current pulse. Furthermore, the processing applies a despiking algorithm and an improved estimate of the background drift which can handle also non-linear drift cases such as electrode polarization effects. This improved drift estimate ensures a more accurate recovery of the IP decay shape (and thus spectral IP content) at late times compared to the normally used linear background drift estimate.

Signal processed IP decay data in the time range of 0.009-0.974s were used for the inversions, which can be compared to a frequency range of 1-111Hz. The decay data were processed in Aarhus Workbench (Auken et al. 2009) prior to the inversions. For many decays, the early time gates seemed to be well retrieved, while they probably were affected by coupling effects in others. All time gates or decay curves that seemed affected by coupling effects, measurement errors or aperiodic noise were removed.

The processed DCIP data were inverted for spectral Cole-Cole model parameters in AarhusInv (Auken et al. 2014; Fiandaca et al. 2012; Fiandaca et al. 2013). The Cole-Cole model is a commonly used phenomenological model in which the parameters resistivity ρ (Ωm), chargeability m_0 (mV/V), relaxation time τ (s) and frequency factor c $(dimensionless)$ describe the shapes of the decay curves (Pelton et al. 1978). The Cole-Cole model assumes a sharp drop in polarization m_0 at a decay time τ, where c describe the pace of the main decrease in polarization. The Cole-Cole relaxation time is generally considered to be proportional to the characteristic length scale over which the charges polarize. The characteristic length scale is dependent on microgeometrical characteristics, e.g. the main grain or pore size in the material. A wider distribution of length scales generally leads to a lower frequency factor (and a less pronounced drop in the polarization at the relaxation time).

SEM and EDS analysis

Although no limestone cores are available from the field site, lithological descriptions of cores in the vicinity were accessible in literature (Kornfält et al. 1978) and from a borehole drilling in Åhus in the Kristianstad basin (Fig. 1). The latter was carried out by an entrepreneur after the DCIP survey, who permitted access to samples from different levels. The samples consist of drill cuttings collected from seven different borehole levels from in between 80-250m depth below the ground surface. The material was stored in cool conditions before it was oven dried at 105°C for 18h. Samples from all seven borehole levels were gently ground in a mortar and the powders were mounted on glass plates with carbon tape. The samples were coated with a thin layer of carbon in a vacuum evaporator (Cressington Carbon Coater 108carbon/A). The samples were then examined with Scanning Electron Microscopy (SEM, Hitachi S-3400N) and Energy Dispersive X-ray Spectroscopy (EDS, Oxford instruments Inca X-sight). The electron source is a tungsten hairpin filament, and the probe current 60.9μA and the acceleration voltage 15kV were used for the scanning. The main elements in the sample were indicated by an analysis of the spectra collected in selected scan areas. A backscatter electron (BSE) detector was used to scan the samples for high-density minerals. The chemical composition of high density minerals were examined by acquiring a spectra in a spot scanning mode.

Following a review of the results, samples from three levels were selected for a more detailed thin section analysis. Dried rock samples were embedded in epoxy resin, and thin sections were made according to the method described in Houssaye et al. (2013). The relative proportion of constituents in the thin sections were calculated based on 300 points per thin section. The thin sections were examined at 10x magnification in an optical microscope with a 0° polarization filter (Nikon Eclipse E400 POL), before they were coated with a thin layer of carbon and examined in the SEM. A secondary electron (SE) detector was used to obtain images of the samples at a working distance of 11.6mm and in a low vacuum mode (60Pa). Chemical mapping was made in the spectrum range 0-10keV with a map resolution of 256x192 pixels. The exposure time for the mappings was around 1500s.

RESULTS

DCIP results

Fig. 4 shows the inverted resistivity, Cole-Cole chargeability and normalized chargeability results from lines 2 and 3. These lines run parallel to each other at a distance 20-30m and are intersected by line 4 around the distance 75m (see Fig. 3). Both lines begin in the urban site (~0-90m) and end in the wetland east of the site (~90-200m). The resistivity results show a quite clear transition at a level that is interpreted as the limestone bedrock surface (black dashed line). Two of the boreholes along profiles 2 and 3 reaches down into the limestone bedrock, where the transition between sandy Quaternary deposits and the consolidated limestone is in agreement with the transition in resistivity. The unconsolidated materials (mainly silty clay) generally have low resistivity values (often below 50 Ωm).

The chargeability sections (Fig. 4b) generally indicate low values in the limestone bedrock, with the exception of a deep anomaly at ~60-100m in Line 2. The strength of chargeability signals are dependent on both capacitive and conductive properties of the subsurface materials. Normalized chargeability is often more effective to use in order to visualize surface polarization properties, since this parameter is normalized against the ground conductivity (Slater & Lesmes 2002a). The normalized chargeability sections (Fig. 4c) also indicate low values in Line 3, while they are slightly elevated in the southwestern half of Line 2.

Above the bedrock in the eastern part of the site, the Quatenary deposits (mostly silty clay) gives rise to well defined zone high normalized chargeability (~50-200m in Fig. 4c). In the southwest (~0-50m), the normalized chargeability sections show a more varying pattern and sometimes an unclear transition between the Quatenary deposits (sandy till) and the consolidated limestone.

Close to the edges of the inverted profiles, the values in the deeper parts of the sections should not be over interpreted due to the low data coverage. It is also important to be aware that urban structures may affect the inverted models and give rise to 3D-effects. The gray and black markers in Fig. 4 show locations where small paths or roads with buried pipes or cables are crossed. The shallow chargeability anomaly in Line 3, located around 130m, may be caused by a gas and/or water pipe. The pipe runs at a shallow depth below the road parallel to the Line 3 from 0-130m, where after it bends south and continue perpendicular to the line (compare with Fig. 3). Therefore, it probably cause a 3D-effect in the chargeability section.

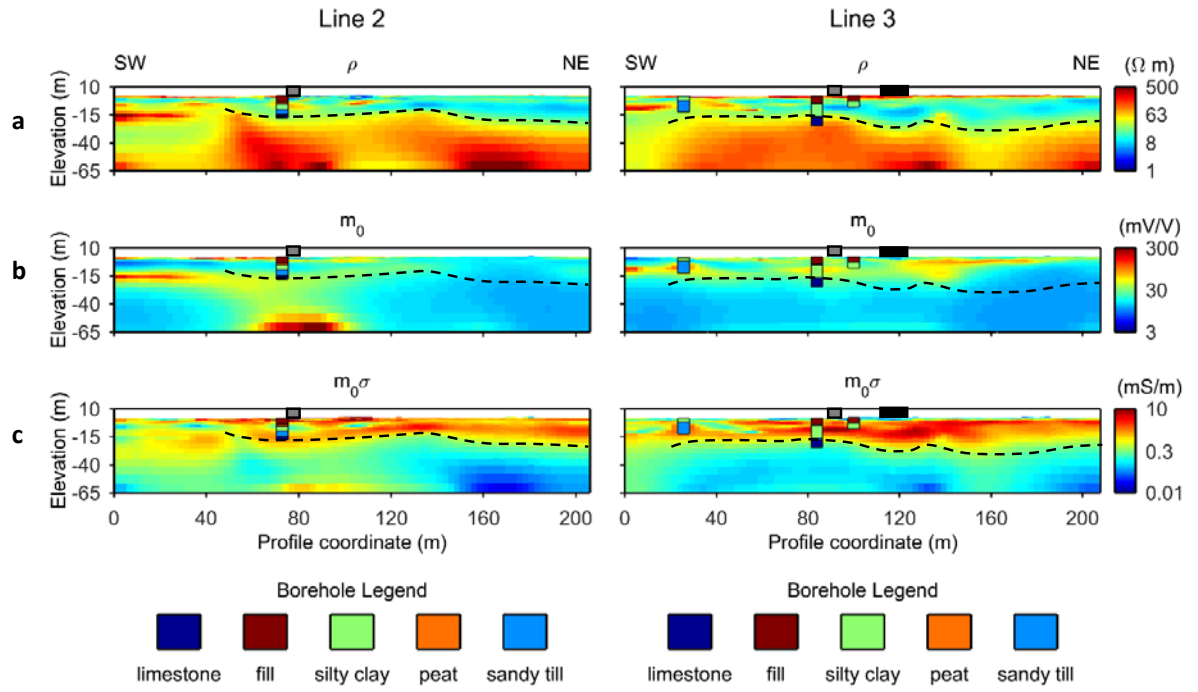

Figure 4. Resistivity, Cole-Cole chargeability and normalized chargeability models of Lines 2 and 3 with reference borehole data (compare with Fig. 3). The gray markers show locations were small paths are crossed, while the black markers show where roads with buried pipes or cables are crossed. **a)** The bedrock level indicated by the deeper borehole corresponds to transition from low to high resistivity, which is interpreted as the limestone bedrock surface (black dashed line). **b)** The chargeability values are generally low in the limestone bedrock, with the exception of a deep anomaly at ~60-100m in Line 2. c**)** The normalized chargeability values are low in Line 3, while they are slightly elevated in the southwestern half of Line 2.

Fig. 5 shows the inverted resistivity, Cole-Cole parameters and normalized chargeability sections from lines 4 and 17. These lines were placed perpendicular to each other and intersect each other at 100m in Line 4 and 150m in Line 17. Three of the boreholes in Line 4 reaches down into the bedrock, where they match the transition from low to high resistivity (Fig. 5a). In Line 4, there is a zone of lower resistivity in the bedrock at distance ~115-150m according to the resistivity model. The normalized chargeability model (Fig. 5e) also indicate an anomalous zone in the bedrock, which coincides with the low resistivity zone. No obvious sources of urban 3D-effects which could explain this zone in the limestone could be identified, as no larger roads with buried pipes or cables were crossed. The environment around the anomaly is also free from buildings (see Fig. 3). A similar pattern was observed in line 17, where a zone of lower resistivity (Fig. 5a) coincides with elevated normalized chargeability (Fig. 5e). The location of this zone is beneath a larger road where pipes and cables are located at shallow depths. This means that possibility of the resistivity and normalized chargeability anomalies being 3D-effects cannot be excluded. However, well delimitated resistivity and chargeability anomalies at ~10m depth (~100-115m), corresponding to probable effects of the road and/or pipes, are clearly visible in the resistivity and chargeability sections (Fig. 5a-b). These anomalies do not extend to deeper depths as could be expected in the case of 3D-effects.

Two anomalies with high Cole-Cole chargeability and slightly elevated relaxation time can be observed in the bedrock in Line 4 (Fig. 4b-c). One of the anomalies is deeply located (~160-170m) while the other can be found at a shallower depth (~80-120m). The frequency factor section (Fig. 4d) indicate lower values close to the ground surface, but no variation in this parameter can be resolved below the bedrock surface.

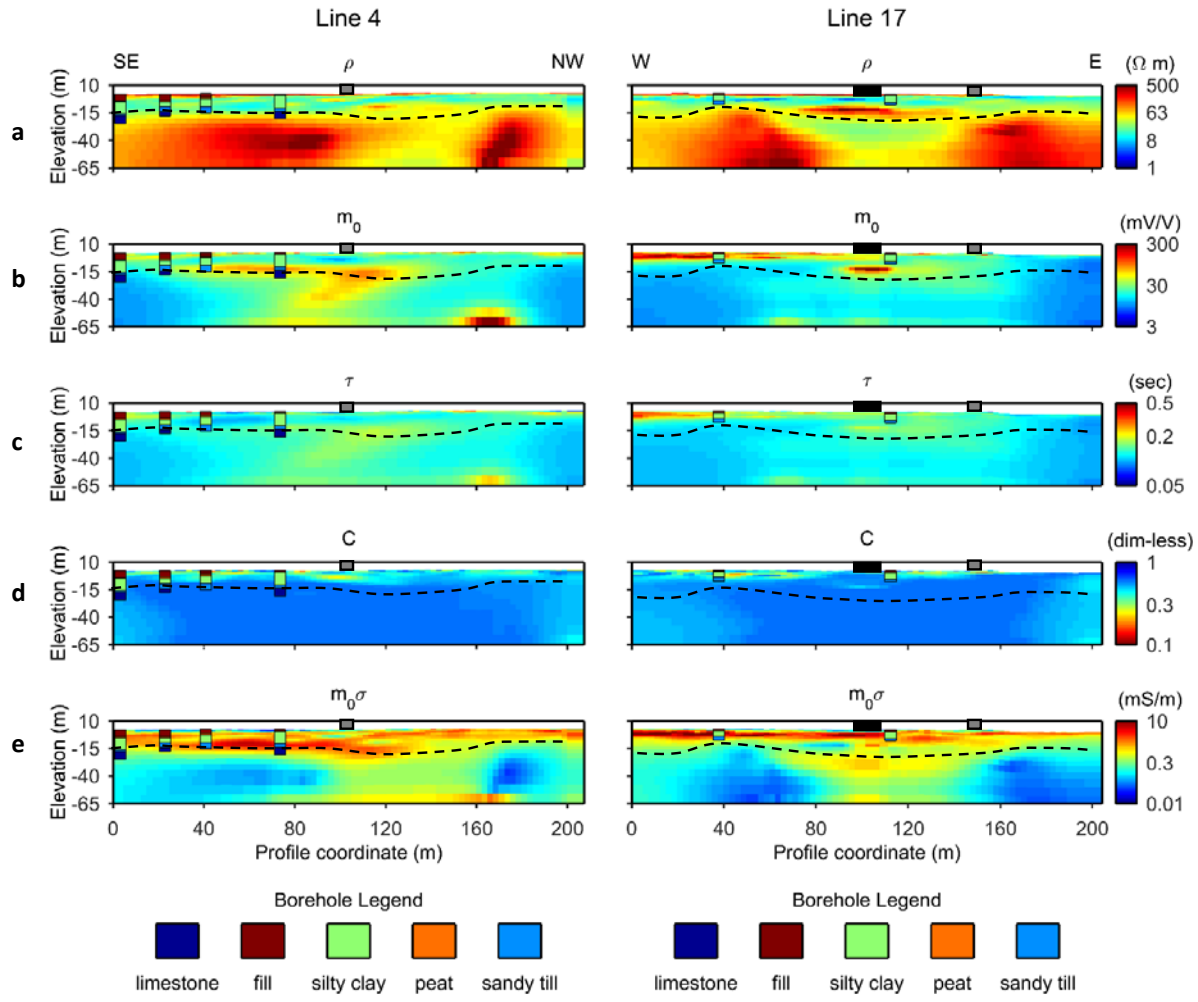

Figure 5. Resistivity, normalized chargeability and Cole-Cole inverted models of Line 4 and Line 17 with reference borehole data and the interpreted bedrock level (black dashed line) **a)** The resistivity models shows lower values in the limestone bedrock at 90-160m in Line 4 and 80-140m in Line 17 **b)** The chargeability values are generally low in the limestone bedrock with the exception of anomalies at 80-120m and 160-170m in Line 4 **c)** The relaxation time is generally below 0.2s in the bedrock, except at the locations of the chargeability anomalies in Line 4 where it is slightly more elevated compared to the surroundings **d)** The distributions in frequency factor do not indicate a heterogeneous bedrock **e)** The normalized chargeability is elevated in the bedrock at approximately 80-150m in both lines.

The Cole-Cole inverted results and normalized chargeability measured in the reference line are shown in Fig. 6. The depth the limestone bedrock surface seem much shallower compared to the main survey area; only a thin layer of lower resistivity can be found close to the ground surface (Fig. 6a). The resistivity range in the consolidated limestone is of the same order of magnitude as in the main survey area or slightly higher. A major zone of higher Cole-Cole chargeability can be observed at 80-160m (Fig. 6b). The zone in also visible in the normalized chargeability section (Fig. 6e), but with weaker values and less pronounced compared to the low chargeability of the surrounding bedrock. In the reference line, the relaxation time and frequency factor sections (6c-d) also show interesting patterns that might indicate textural variations within the bedrock. In the reference line, no man-made constructions or installations are present in the vicinity, which means the variations in IP response can be linked to variations in the limestone composition or structure.

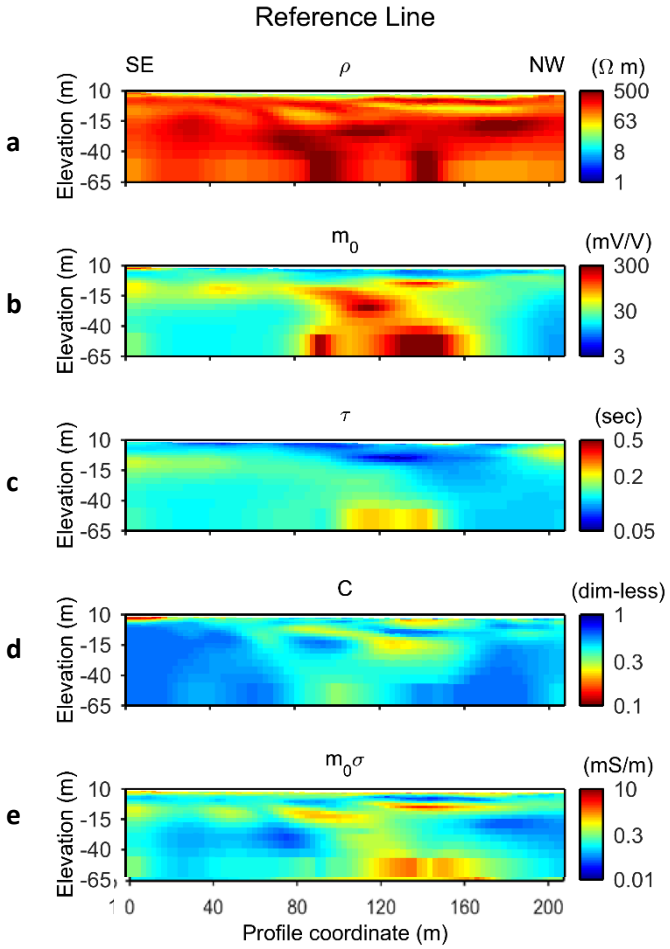

Figure 6. Resistivity, chargeability and normalized chargeability models of the reference line measured in a rural area at a distance of 4km from the main survey area. The resistivity model (a) shows high resistivity beneath a shallow low resistive till layer. The chargeability and normalized chargeability values (b and e) are generally low except for a well-defined anomaly. The Cole-Cole relaxation time (c) and frequency factor (d) sections show interesting variations that might reflect textural variations within the limestone.

The resistivity and normalized chargeability sections of the four profiles in the main survey area are visualized in a fence diagram in Fig. 7. Despite the noise problems related to the urban environment, the data in the models are in agreement with each other which confirm a certain degree of accuracy in the results.

It can be concluded that the resistivity values of Quaternary deposits are generally low in the main survey area. The fill, silty clay and peat layers give rise to high normalized chargeability in all profiles. The resistivity in the limestone bedrock generally varies in the range 100-500Ωm. The main low resistivity anomalies with elevated normalized chargeability that were observed in Line 4 and 17 (Fig. 5) are geometrically connected, as shown in Fig. 7. The anomalous zone might also extend into the southwestern most parts of Lines 2 and 3 (even though the data coverage is low here and the values in the bedrock should be interpreted with care). The 3D visualized data thus indicate a geological structure running through the main survey area in a north-south direction.

Lithological variations in cores

The sedimentary bedrock in the Kristianstad area is generally described as made up of relatively well consolidated limestone, loose sandstone or mixes thereof. In addition, layers of glauconitic sand are also present. The limestones are made up by sand- or finer grained shell- and skeletal particles. Chert and flint are not generally common regionally, but have been observed at depths of 16-40 m beneath Kristianstad (Kornfält et al. 1978).

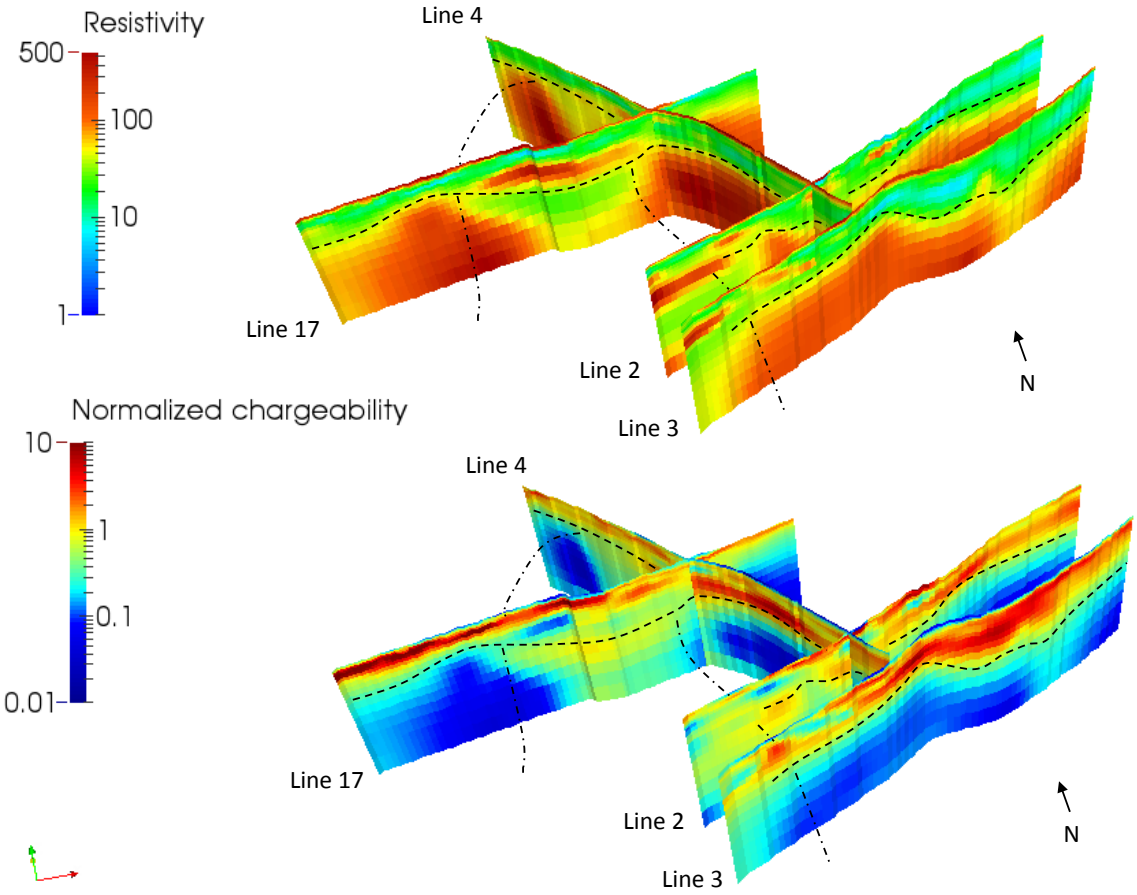

Figure 7. 3D visualization of the resistivity and normalized chargeability results from the main survey area showing a good agreement between the different DCIP profiles. The interpreted bedrock surface is marked with black dashed lines. While the transition to the bedrock is clear in most parts of the site, there are indications of a geological structure with lower resistivity and higher normalized chargeability running through the survey area in a north-south direction.

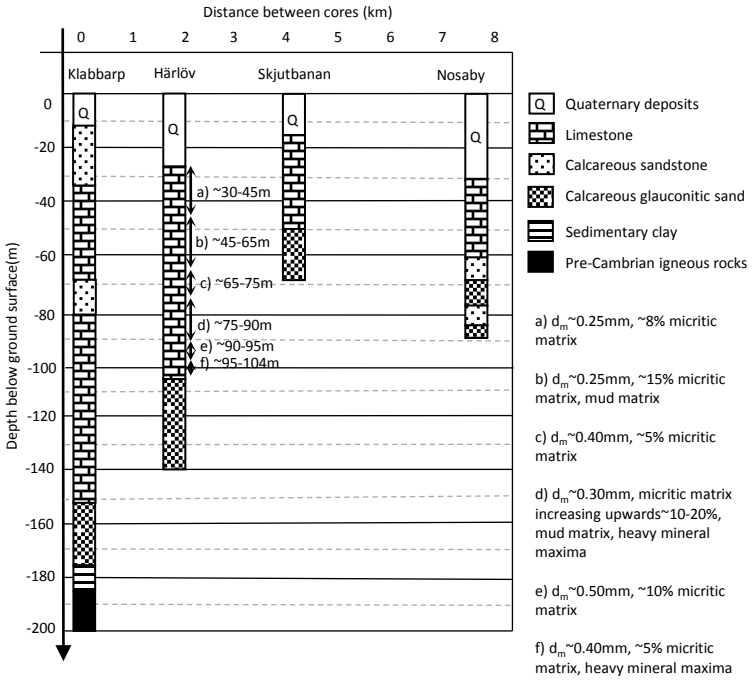

Figure 8. Visualization of the main geological units in the reference cores shown in Fig. 3 (modified from Kornfält et al. 1978).

The stratigraphy of the cores close to the main survey area (shown in Fig. 1) have been described by the Geological Survey of Sweden (Kornfält et al. 1978). The main geological units in these cores are visualized in Fig. 8, and the varying depths to the different units can be followed between the boreholes. The depth and thickness of the limestone is largest in the core from Klabbarp, which is located close to the horst (see Fig. 1). From here to Skjutbanan, the depth to the glauconitic sand layer decrease from ~155m to ~50m. As can be seen in Fig. 1, the main survey area is most closely located to the Härlöv and Skjutbanan sites. The most probable depth to the upper surface of the glauconitic sand layer is therefore, based on the available reference cores, somewhere between 50-100m in the main survey area and around 50m in the reference survey area. While the thickness of the limestone is almost 75m in Härlöv, it is limited to approximately 35 m in the Skjutbanan core.

For the Härlöv core (the one closest to the main survey area), a detailed lithological analysis of the limestone has been carried out (Kornfält et al. 1978). At this location, the glauconitic sandstone appears at levels deeper than 100 m below the ground surface. Above this layer is the approximately 70 meters thick sandy limestone consisting of 70-80% calcium carbonate. The mean particle size changes from coarser particles at depths around 90-95 m to finer and then coarser again around 65-75 m. The coarser levels are generally less sorted compared to the fine grained section. In the fine grained and well sorted section around 75-90 meters, there is a local maximum of heavy minerals that do not frequently occur at other levels in the core. Heavy minerals tend to accumulate close to shorelines, and the data together indicate sediment environments going from deeper water levels to shallower and then deeper again. Another transition from deep to shallow water levels is reflected in the section of the sandy limestone at approximately 45-65 m below the ground surface. Here, the amount of heavy metals increase upwards and the particles are embedded in a muddy matrix. Although the maximum mud content is found at the level 45-65 m, there are varying amounts occurring in the sandy limestone throughout the core. From the transition between the Quaternary deposits and the sandy limestone at approximately 30 meters below the ground surface, the mean particle size is relatively fine to the depth of 65 m. The amount of glauconite in the core does not show any clear correlation with the other lithological data; small amounts are present at certain levels and absent at others. The amounts increase however at depths below 90 m (Kornfält et al. 1978).

Structure and mineral content of drill cutting samples

The Åhus borehole is located close to the horst in the Kristianstad basin (Fig. 1). The thickness of the limestone is around 190m, and the surface of the glauconitic sandstone is located around 220m below the ground surface. The samples that were analysed with SEM and EDS represent the transition between the deeper part of the limestone and the glauconitic sandstone, see Fig. 9. It was assumed that similar properties could be found at shallower depths in the main and reference survey areas, since the upper surface of the glauconitic sand likely occurs at 50-100m depth at these locations.

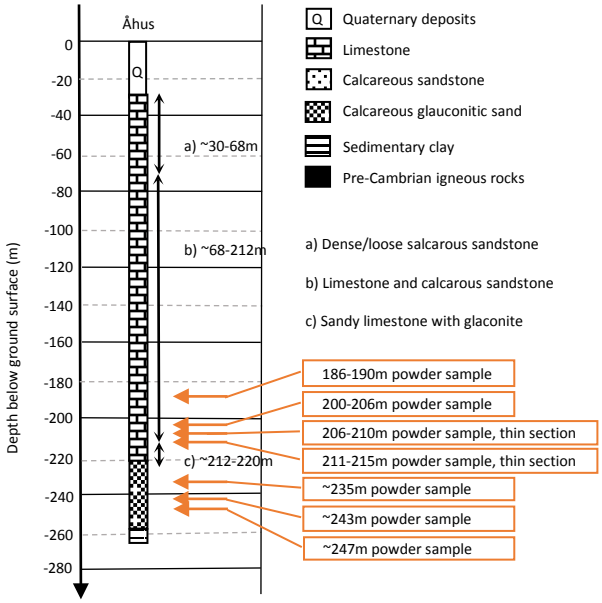

Figure 9. The main geological units in the Åhus core (personal communication, Martin Ekvy, Malmberg Borrning, June 2015). The levels where samples were collected and analyzed with SEM and EDS are shown.

The texture, degree of consolidation and color varied among the seven borehole samples. Qualitative observations are summarized in Table 1. The SEM and EDS analyses of thin sections enabled both structural and quantitative

results, while the grinded powder samples gave a qualitative estimate of the mineralogical content in the samples. An overview of the results from the SEM and EDS analyses of the grinded powder samples are also reported in Table 1. In addition to Ca, Si, K, Al and Mg, which were found in varying amounts in most of the samples, traces of metallic elements were also found. Iron was found in most of the samples, often in the form of pyrite (Fig. 10) but also in other compounds, probably iron oxides. In addition, Ti, Cr, Ni and W were found in several samples but the possible mineral form of these elements were difficult to determine. It is possible that some of these elements originates from the drilling equipment.

Table 1. Description of the samples and overview of the results from the powder SEM and EDS analysis.

Borehole depth (m)	Description	Photograph (dried sample)	Main elemental constituents	Other elements
186 - 190	Whitegray chalk, high water content		Ca, Si. Very small amounts of K, Al and Mg	
200 - 206	Browngray chalk, lumpy with high water content		Ca, Si. Higher proportion of Si, K, Al and Mg compared to the above core level.	Fe, S, Zr
206 - 210	Whitegray chalk, consolidated with low water content		Almost pure Ca. Small amounts of Si.	Fe, S
211 - 215	Greenwhite chalk, high water content		Ca, Si. Small amounts of K, Al and Mg Similar composition as level 186-190m	Fe, S, Ti, Fe, Cr, Ni, W
~235	Green glauconitic sand, high water content		Si with relatively small amounts of Ca, K, Al and Mg.	Fe, S, Ti
~243	Green glauconitic sand, high water content		Si with relatively small amounts of Ca, K, Al and Mg. Significant amounts of Fe.	Fe, S, Ti
~247	Light green glauconitic sand, high water content		Si with relatively small amounts of Ca, K, Al and Mg. Less amount of Fe compared to the level above.	Fe, S, Cr, Ni, Zr, P

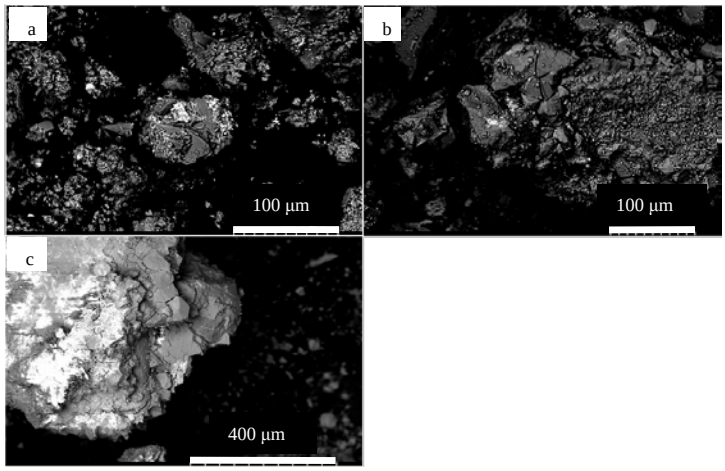

Figure 10. a) Pyrite minerals found in the limestone sample from level 200-206m. Small amounts of Ca, K, Al and Mg was also detected at the mineral surface. **b)** Pyrite mineral found in the limestone sample from level 206-210m. Small amounts of Ca and Si was also detected at the mineral surface. **c)** Pyrite mineral found in the limestone sample from level 211-215m. Small amounts of Ca and Ti was also detected.

Limestone at 206-210m depth

A photograph of the thin section from borehole level 206-210m is shown in Fig. 11. The material is almost exclusively made up of sand-sized carbonate grains (fossil fragments/skeletal grains, relatively well sorted) and calcite cement. This observation was confirmed by the SEM and EDS-analysis, which showed that the major part of the thin section consisted of calcium carbonate, although a few silica grains (quartz) were also found in the sample (Fig. 13). The calcium carbonate in the thin section consist of 55% grains, 34% cement and 11% micritic matrix. According to the widely used Dunham classification system for carbonate textures, the sample can be described as a grainstone with subordinate packstone. Grain- and packstones have a grain-supported microstructure in contrast to e.g. mudstones, and the different textures can have implications on rock properties such as e.g. groundwater permeability and porosity (Dunham 1962).

Most grains in the sample are indeterminable abraded/rounded carbonate grains. Still, a variety of fossil types are recognized in the grain assemblage, including fragments of echinoderms (Fig. 12b), foraminifera and putative coralline algae and plant debris (Fig. 12a). Small curved shells, likely ostracode valves (see e.g. Adams et al. 1984, figures 104 and 105), are relatively common at this core level (Fig. 11).

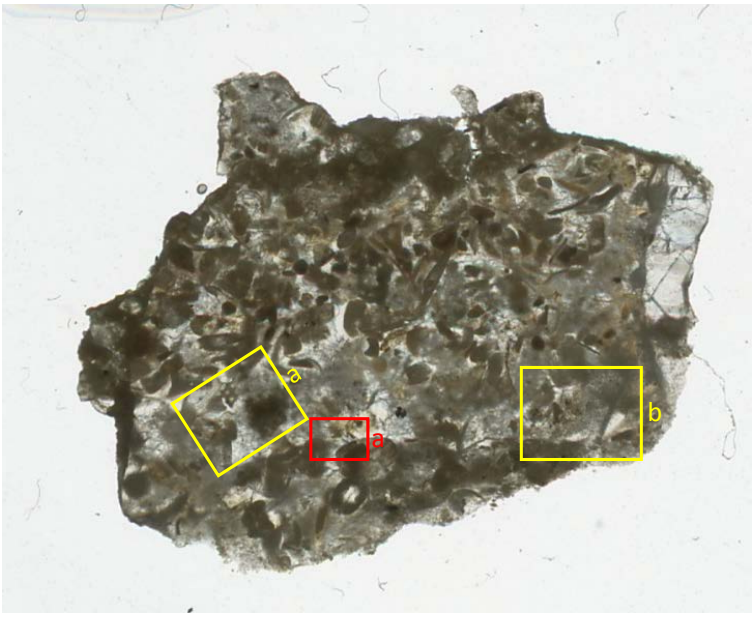

Figure 11. Photograph of the thin section from core level 206-211m. Microscopic photographs of the yellow framed subareas are shown in Fig. 12, and chemical mapping of the red subarea is shown in Fig. 13.

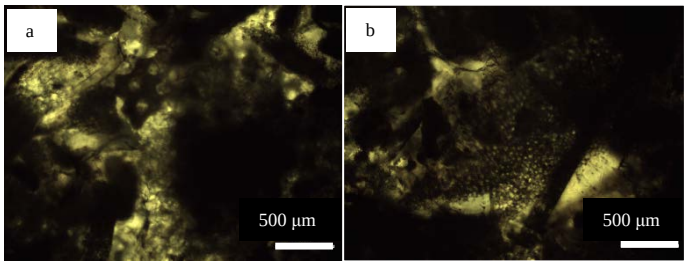

Figure 12. Photographs taken with a polarized optical microscope, showing details of the calcite structure in selected (yellow) subareas of the thin section in Fig. 11 (level 206-211m). No silica based grains are visible.

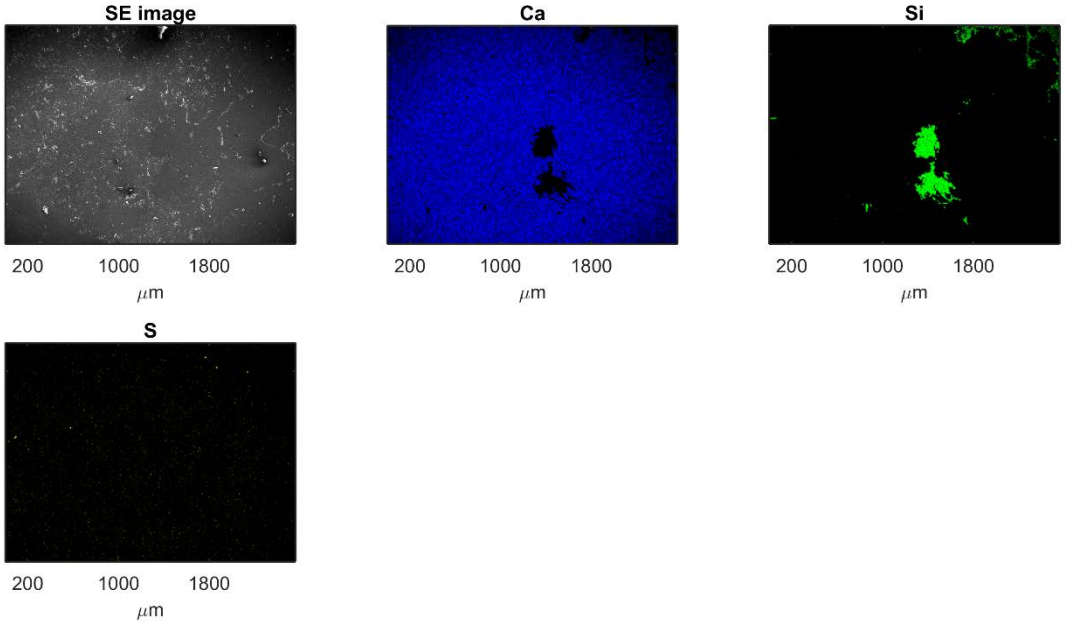

Figure 13. Chemical mapping of the red subarea in Fig. 11. The limestone sample (level 206-211m) almost exclusively consist of calcium carbonate.

Limestone at 211-215m depth

The limestone sample from borehole level 211-215m consists mainly of sand-sized carbonate grains (fossil fragments/skeletal grains, relatively well sorted) interspersed by calcite cement, but the structure and composition of the material differs from the borehole level above. The grains contain a larger proportion of relatively well-preserved grains, typically elongate in shape (Fig. 14). Fossil types include echinoderm debris (e.g., crinoid stems; Fig. 15b), putative bivalves and coralline algae, and ostracode-like valves. Microbioerosion is extensive and many grains contain numerous minute borings. The carbonate texture varies between packstone and grainstone (Dunham 1962). The calcium carbonate in the thin section consist of 62% grains, 23% cement and 15% micritic matrix.

Also in contrast to the borehole level above, a significantly larger amount of quartz and feldspar grains are found in this sample. Grains of apatite (Ca, P) and pyrite (Fe, S) were also identified with the SEM and EDS-analysis, as well as glauconitic grains (Fe, Si), see Figs 16-18. The average proportion of siliclastic and glauconitic grains in the thin section are 8% and 1.6% respectively. The chemical mappings from the SEM and EDS-analysis imply a combination of calcite cement and clay matrix surrounding the sand sized grains. The distribution of pyrite and glauconitic grains vary in different subsections, as can be seen in Figs 17 and 18.

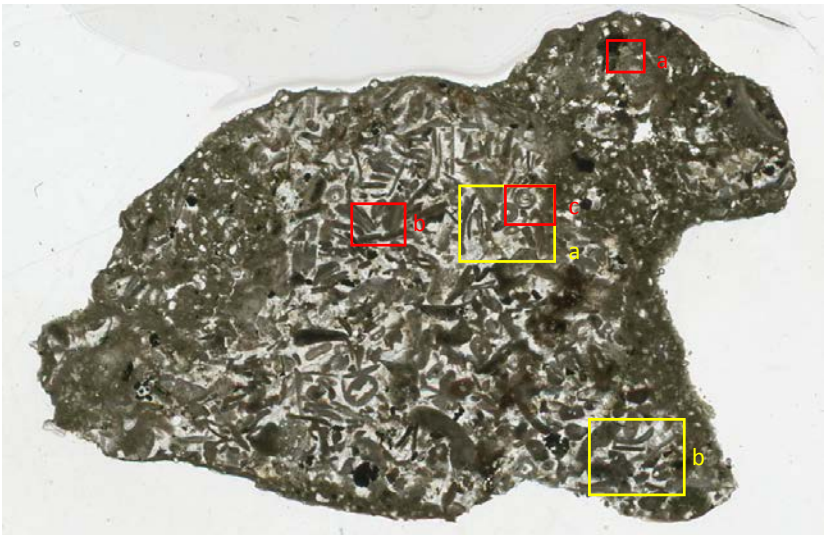

Figure 14. Photograph of the thin section from core level 211-216m. Microscopic photographs of the yellow framed subareas are shown in Fig. 15, and chemical mappings of the red subareas are shown in Figs 16-18.

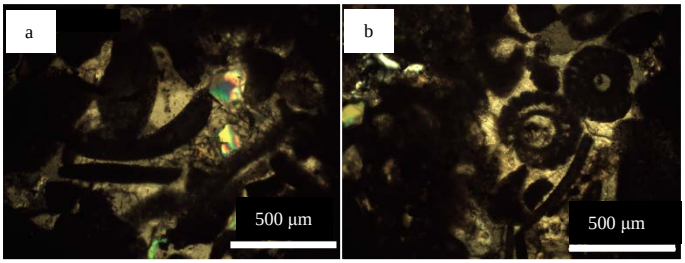

Figure 15. Photographs taken with a polarized optical microscope, showing details of the calcite structure in selected subareas of the thin section in Fig. 14 (level 211-215m). Silicate grains are visible due to the refracted polarized light.

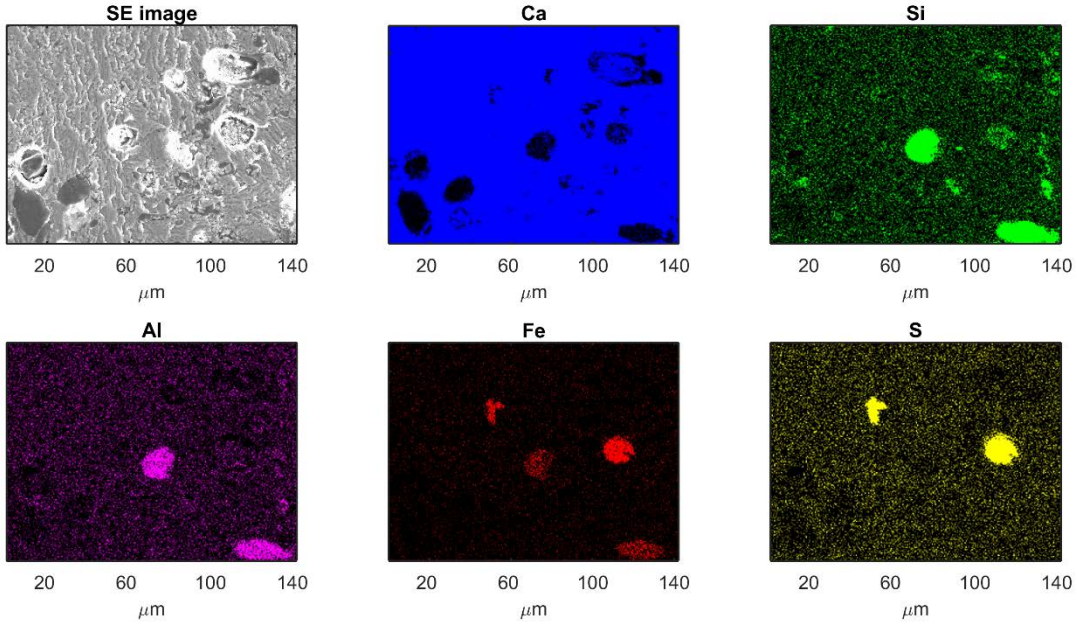

Figure 16. Area a in Fig. 14. The chemical mapping indicate pyrite grains (Fe, S) and glauconitic feldspar grains (Fe, Al, Si) interspersed in the limestone (Ca).

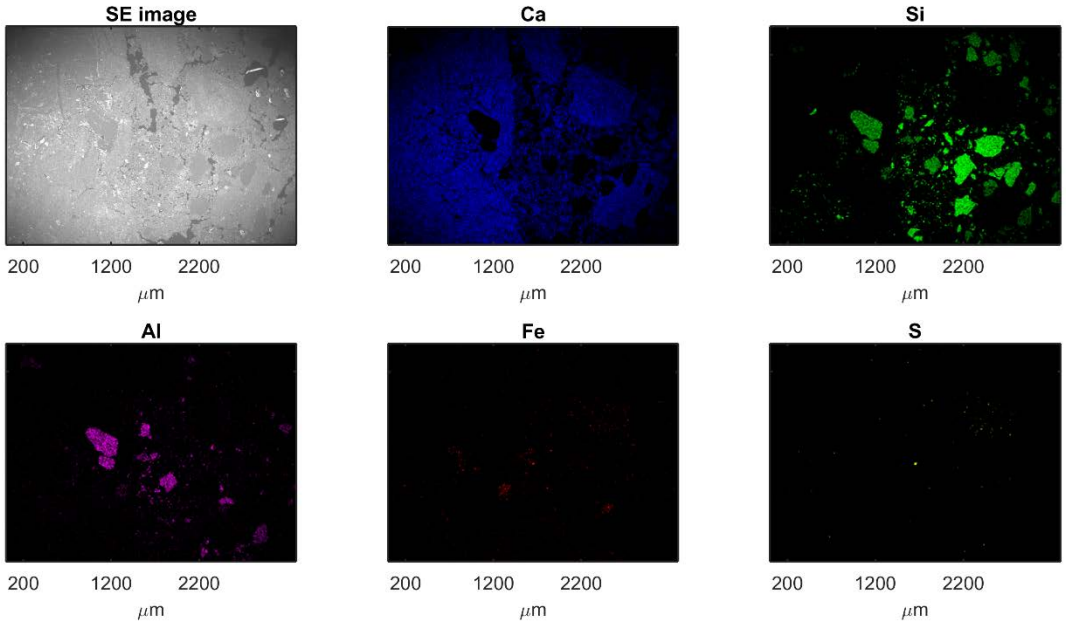

Figure 17. Area b in Fig. 14**.** This part of the sample mainly contain calcium carbonate together with quartz and feldspar grains. Fe and S is present but the concentration and grain sizes are small.

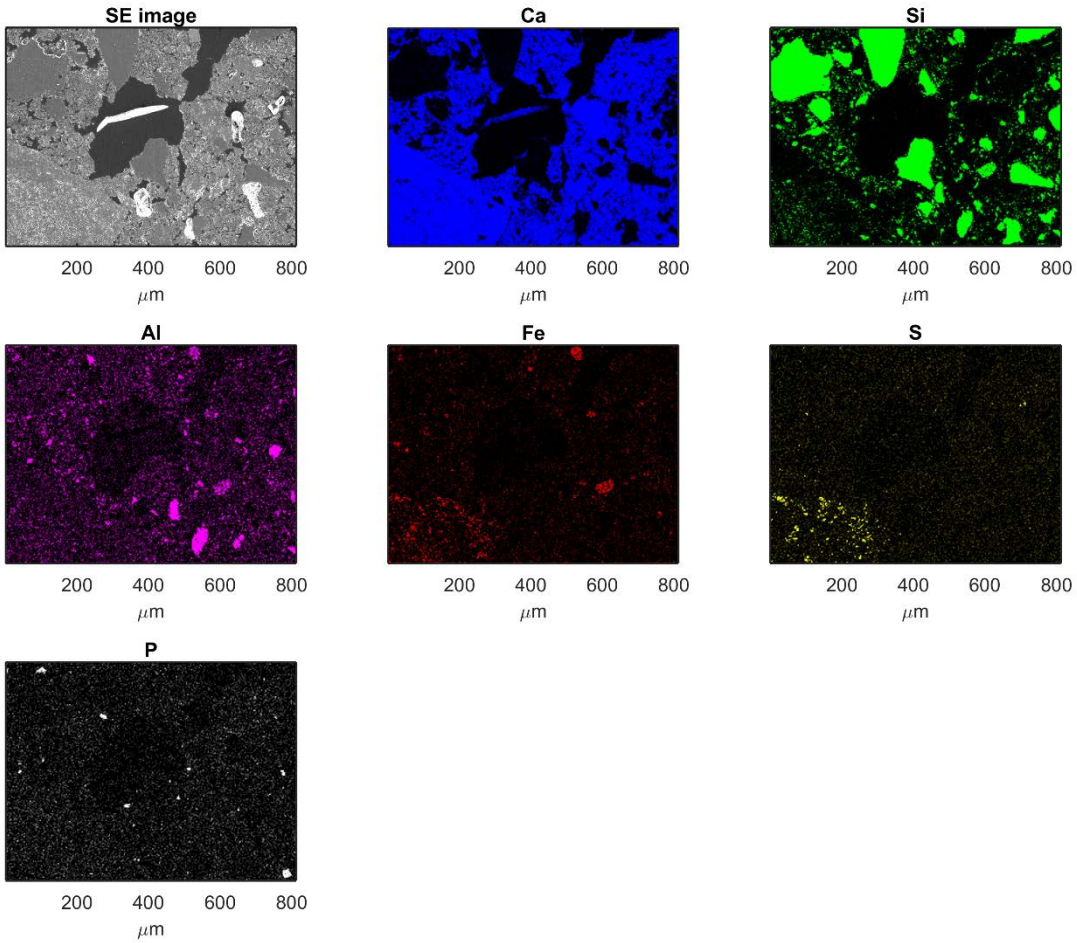

Figure 18. Area c in Fig. 14. High concentration of pyrite can be observed in the lower left corner (as indicated by Fe and S). The high and widely distributed Al and Si concentrations indicate clay matrix surrounding the grains of calcium carbonate (Ca), quarts (Si), feldspar (Si and Al) and apatite (Si and P). A few of the grains are probably glauconitic (Fe in combination with Si and/or Al). The dark parts in the SE image probably represent cavities in the material (or possibly organic carbon).

Glauconitic sand at 247m depth

Fig. 19 shows the thin section of the glauconitic sandstone sample. The material seems to consist of larger and smaller silicate grains embedded in finer material with a greenish to blackish color. The chemical mapping (Fig. 20) shows that the larger grains are mainly composed of quartz and feldspar, although a larger probable apatite grain is also visible (indicated by high amounts of Ca and P). Glauconitic grains are indicated by Fe in combination with Si or K. Fe, Ca and P generally seem to be present both as small grains and as finer material in between the large silicate grains.

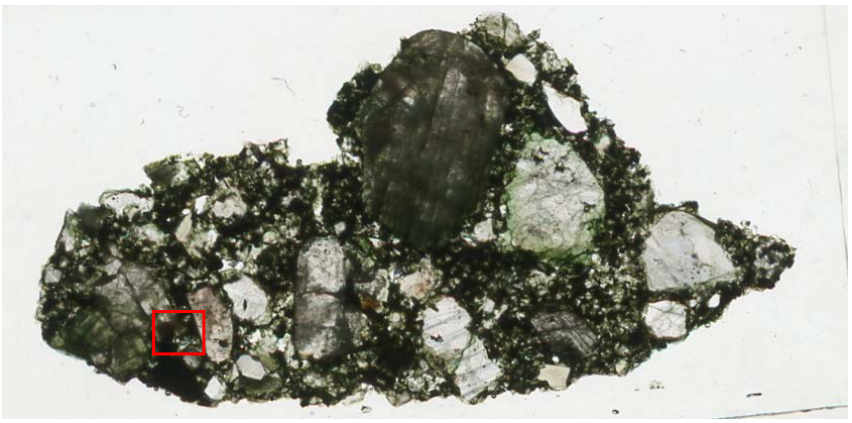

Figure 19. Photograph of the thin section from core level ~247. The red frame show the subarea corresponding to the chemical mapping in Fig. 20.

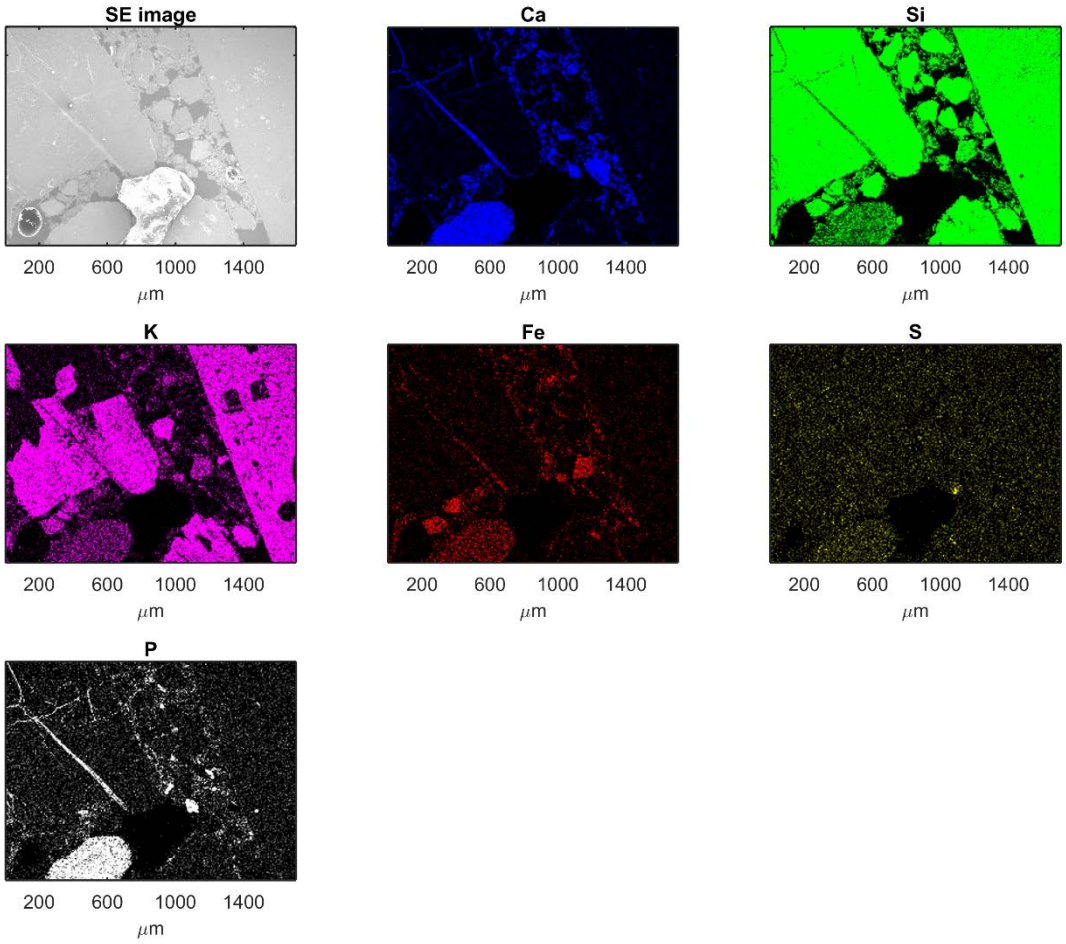

Figure 20. SEM and EDS results in a subarea of the thin section from the glauconitic sand at core level ~247m. The larger grains consist of quartz (Si), feldspar (K and Si) and apatite (Ca and P). With the exception of the bottom left grain, the apatite and the calcium carbonate is mainly distributed in cracks and as finer material in between the larger grains. The Fe distribution show that some of the larger grains are glauconitic and that glauconitic fine material is also present in the sample.

DISCUSSION

DCIP results

Some of the previous difficulties in characterizing the geological setting around the main survey area were resolved with the DCIP survey. While it was difficult to estimate the transition between the till and the bedrock surface based on drilling data, the resistivity models often show clear transitions between the low resistivity Quaternary deposits and high resistivity limestone bedrock. In Fig. 7, the interpreted bedrock surface is marked with black dashed lines, and it can be seen that the bedrock level is easily distinguished in the north-eastern part of the site. Through the center areas of the site, however, the resistivity results consistently indicate a discontinuation of the bedrock surface forming a geological structure running in an approximately north-south direction.

The measured resistivity values varied in both the main and reference survey areas and were generally in the range 100-500Ωm, except in the low resistivity anomalies where the values were below 100Ωm. At some locations the resistivity values also reached well above 500Ωm (see Figs 4-6). Resistivity values ranging from 800-1500 Ωm in fractured zones to up to 4000 Ωm in unfractured zones were measured by Gélis et al. (2010) in Jurassic limestones and dolomites deposited in a Mesozoic marine basin in France. The presence of dolomite, which is more compact than limestone, might explain the higher resistivity values obtained in their study (Gélis et al. 2010).

The low resistivity measured in the anomalous geological structure in our study indicates either fractured or porous bedrock with higher water content, locally higher water conductivity or a difference in the lithology. Degradation and dissolution of chlorinated hydrocarbons may induce changes of the groundwater conductivity. However, chlorinated hydrocarbons are resistive compounds and it is unlikely that the degradation products would lead to a strong decrease in resistivity of the magnitude observed here. Furthermore, the elevated normalized chargeability in the low resistivity zone do not support the interpretation of higher water content as the only

explanation, since this more likely leads to decreased IP effects (see e.g. Titov et al. 2004). That is, with regards to the IP results, it is more likely that low resistivity anomalies in the bedrock are caused by a local variation in the geological material. Because of the challenging urban environment in the main survey area, it cannot be excluded that some of the chargeability variations are caused by unidentified buried infrastructures or 3D-effects. However, the variations in Cole-Cole parameters found in the reference survey area show that natural IP variations within the limestone are probable.

High IP and low resistivity in fractured bedrock have in previous research been observed in silicate bedrock, where they were interpreted as a result of clay weathering (Marescot et al. 2008; Magnusson et al. 2010). However, the weathering processes in pure limestone usually results in dissolution of calcium carbonate into the groundwater without any significant precipitation of clay minerals. Thus, IP anomalies in the bedrock were unexpected at this site.

Microgeometrical variations

Pure limestone is generally expected to be a non-polarizable geological material in the low frequency range. The surface charge on calcium carbonate minerals is weaker compared to the surface charge of e.g. silica minerals (Zhang et al. 2012), and the absence of IP effects have been observed during laboratory SIP measurements on rock samples (Ghorbani et al. 2009). However, since IP effects are dependent on pore geometry, it could be possible that fossil shapes, limestone texture or changes induced by calcium carbonate dissolution and precipitation processes in the rock could affect the signals. Laboratory studies have shown indications of either increased or decreased polarization responses due to calcium carbonate precipitation in granular media. The precipitated calcium carbonate minerals change microgeometrical properties of the pore space, and the polarization response seem dependent on whether the calcium carbonate precipitates on grain surfaces or as small discrete particles in the pore space (Zhang et al. 2012).

In the higher frequency range of 100Hz – 100kHz, variations in the dielectric constant among different limestone and dolomite samples have been measured with dielectric spectroscopy. The dielectric constant and its frequency variation was attributed to both electrochemical and interfacial polarization mechanisms, which appeared dependent on the chemical composition, density, porosity, water content and inhomogeneity of the samples (Sengwa & Soni 2006). It cannot be excluded that interfacial polarization mechanisms are present in the early decay times of our data, and that interfacial variations in the rock could influence the results.

The SEM and EDS-analyses of samples from the Åhus borehole showed that both the structure and the chemical composition of the limestone varied at different levels in the borehole. While the limestone at level 206-211 can be classified as a grainstone, the texture varies between packstone and grainstone at level 211-215m. Varying amounts of clay matrix in the limestone could probably give rise to varying IP responses. At the borehole level 206-211m, the limestone sample was almost exclusively composed of calcium carbonate. In contrast, clay matrix and a significant amount of silicate minerals were indicated at level 211-215m.

It has been known for a long time that certain minerals e.g. magnetite and many sulfides produce IP effects when they are disseminated in a host rock (e.g. Pelton et al. 1978). These minerals have in common that they are electrically conductive; other minerals containing similar elements do not give rise to IP effects due to their low electrical conductivity (e.g. Bertin & Loeb 1976). Varying heavy mineral occurrence has been observed in the Härlöv core, but details about the composition of different types of heavy minerals were not reported by Kornfält et al. (1978). The SEM and EDS-analysis of samples from the Århus borehole showed that varying amounts of iron and sulfide were found in most of the investigated borehole levels. Presence of pyrite (or possibly pyrrohotite, both conductive minerals) was confirmed in the limestone at borehole levels between 200-215m and in the glauconitic sandstone at levels ~243m and ~247m. The chemical mapping of the thin section from 211-215m indicated relatively high concentrations of pyrite in some subareas (Figs 16 and 17). Pyrite mineral impurities in calcium carbonate have resulted in measureable IP anomalies in previous research. In a study by Okay et al. (2013), calcite-filled cracks in a clay rock formation with 16% (by weight) pyrite gave rise to IP anomalies larger than 10-20mV/V. In the same formation, calcareous nodules with 5-6% pyrite also produced IP effects of almost the same order of magnitude (~10-20mV/V). Even smaller amounts of sulfides can give significant IP responses. Chargeability values of 100-500mV/V corresponding to 0.2-2% disseminated sulfides in porphory were reported by Pelton et al. (1978).

The detected iron in the Åhus samples was not only present as pyrite. High Fe concentrations corresponding to the locations of silicates indicated presence of glauconitic sand in the limestone at level 211-215m (see e.g. Fig. 16). Glauconite is an iron-rich micaceous clay mineral (iron potassium phyllosilicate), but glauconite is also used as a morphological term for sand sized grains in which other mineral types may also be present. In morphological glauconite sand, the mineral glauconite exist as e.g. pellets (aggregates) or a as a pigment in cracks and on surfaces of other minerals (McRae 1972). In the glauconite sample investigated here, the glauconite appeared to be present both as pellets/grains and as fine material on grain surfaces and in cracks in between larger quartz and feldspar grains (Fig. 20).

Glauconite usually contain around 15-30% iron, and although most of the iron is in the ferric state Fe_2O_3, glauconite also contain iron in the ferrous state FeO (Thompson & Hower 1975; McRae 1972; Carroll 1958). The amount of ferrous iron in relation to the total iron content in glauconite is usually in the range 10-20%, but the ratio is also dependent on the redox conditions (Fanning 1989; McRae 1972). Iron oxides in the ferrous state (magnetite and wüstite) have high conductivity and can thus produce high IP effects (Bertin & Loeb 1976), while iron oxides in the ferric (oxidized) state (hematite) have lower conductivity values (Tannhauser 1962; Vella & Emerson 2012). It is known from the Härlöv core that glauconitic sand is present at different levels throughout the limestone. It is likely that high presence of glauconite can lead to enhanced IP effects, either due to high conductivity of the iron oxides or due to high cation exchange capacity of the phyllosilicate sheets.

Geological processes

Microgeometrical structure and mineral content in the bedrock are important factors governing the measured IP signals. According to the Härlöv core, there are variations in the microgeometrical characteristics of the limestone originating from variations of the depositional environment during the formation of the limestone. If a local depression in the limestone has been present at some point, it is reasonable that a deeper depositional environment would exist in the depression while shallower conditions prevail in the surroundings. With a local deep sedimentation environment, deposition of smaller grain sizes and larger amounts of mud matrix are probable.

Local depressions in the limestone bedrock surface could be the result of depressions or weakness zones in the underlying granite bedrock, leading to vertical differences in the sedimentation history of the limestone. It is known that in the Kristianstad area, the grain sizes and constituents of the sandy limestones and calcareous sandstones vary dramatically in both horizontal and vertical directions. These differences have arisen due to a varying depositional environment, with both shallower and deeper marine periods and periods of land.

Another possible cause of local limestone variations is calcium carbonate dissolution and karst formation at some point in time. When karst cavities collapse, they can be filled with surrounding soil or with limestone material from a higher level. Low resistive zones corresponding to clay-filled karst cavities in a limestone formation have been detected in previous research (Park et al. 2014).

Although the limestone in the Kristianstad basin is estimated to contain 70-80% calcium carbonate, it is still possible that clay weathering of the silicate grains occur. However, if weathering in fracture zones occurred in this limestone, it is likely that the increased chargeability would be cancelled by the increased porosity due to the calcium carbonate dissolution in the fractures.

Uncertainties

A general consideration with DCIP surveys is the reliability of the inverted models. The exact shape of the inverted anomalies are not resolved due to inversion effects and decreasing data resolution with depth. In particular IP data can be difficult to resolve at great depths, since the signal-to-noise ratio of the potential measurements becomes weaker. Lower signal-to-noise ratio increase the risk of inverted models which are dominated by effects caused by inversion constraints (Fiandaca et al. 2015).

The urban character of the site and the noise that affected data complicated the data processing, inversion and interpretation in this study. The signal processing scheme successfully reduced periodic noise and allowed retrieval of data from early decay times. Use of early decay times increases the risk of coupling effects in the data superimposed on the information arising from the geological target (Dahlin & Leroux 2012). However, many of the decays appeared to be unaffected by such effects and all early decay times that were suspected to contain coupling effects were removed from the data set during the processing.

The short current pulses used during the measurements (1s on-off times) can lead to lower signal-to-noise ratio than what would be achievable with longer current pulses (Olsson et al. 2015). Another implication might be a reduction of spectral information in the decays, especially in the case of long relaxation times in the subsurface. The retrieval of early decay times increased the spectral content of the IP decays in this study, and the Cole-Cole model could be used to fit the data.

CONCLUSIONS

Discrimination between the sandy chalk till and the consolidated limestone had previously been difficult to establish using only drilling in the main survey area. Our results shows that the DCIP survey provides an effective imaging of the upper surface of the Cretaceous limestone here.

The normalized chargeability responses of the limestone are low in the major part of the bedrock. However, zones of elevated normalized chargeability are also present. The main survey was performed in a technically challenging urban area, whereas a reference survey performed in a rural area confirmed the presence of natural IP variations within the limestone bedrock. In the reference line, interesting variations in Cole-Cole relaxation time and frequency factor were resolved that probably reflect textural variations within the limestone.

The SEM and EDS analysis of limestone samples from the Kristianstad basin confirmed variations in terms of structure and of chemical composition at different levels in the borehole, both. It was concluded that varying amounts of clay matrix, pyrite minerals and glauconite within the limestone could provide an explanation to the observed variations in chargeability. Varying textural properties, such as e.g. fossil shapes and composition and the proportion of calcite cement and micritic matrix might induce variations in Cole-Cole relaxation time and frequency factor. However, more research is needed in order to better connect spectral IP responses to different microstructural properties of limestone.

The observed low resistivity and high normalized chargeability anomalies in the main survey area do not specifically indicate zones of higher water conductivity. The dissolution of calcium carbonate in weathered limestone zones would more likely result in low resistive anomalies without any enhanced chargeability. Therefore, we conclude that the anomalous structure more likely origin in a local variation in limestone structure or composition. Vertical variations in microgeometrical properties within a limestone could appear due to local depressions in the Precambrian rock surface, collapsed karst structures or other morphological processes. More research is needed to confirm this interpretation.

The results from this study show that it is possible to recover useable spectral information from early decay times. We also show that under certain conditions (e.g. relatively short relaxation times in the subsurface), it is possible to extract spectral information from time domain IP data measured with as short on-off times as 1s. Short on-off times significantly reduce the survey time, but longer on-off times are generally recommended if it longer relaxation times can be suspected in the subsurface.

ACKNOWLEDGEMENTS

We would like to thank Johan Lindgren and Leif Johansson at Department of Geology at Lund University for help, assistance and guiding of SEM and thin section preparation, Martin Ekvy at Malmberg Borrning AB for providing drill samples from Åhus and Mikael Lumentzberger and Carl-Henrik Månsson for field work assistance. Funding for the work was provided by Formas - The Swedish Research Council for Environment, Agricultural Sciences and Spatial Planning, (ref. 2012-1931), BeFo - Swedish Rock Engineering Research Foundation, (ref. 331), SBUF - The Development Fund of the Swedish Construction Industry, (ref. 12719) and Sven Tyréns Stiftelse. The project is part of the Geoinfra-TRUST framework (http://trust-geoinfra.se/).

REFERENCES

Adams, A.E., MacKenzie, W.S. & Guilford, C., 1984. *Atlas of sedimentary rocks under the microscope*, Essex: Longman Group Limited.

Auken, E., Christiansen, A. V., Kirkegaard, C., Fiandaca, G., Schamper, C., Behroozmand, A. A., Binley, A., Nielsen, E., Effersø, F., Christensen, N.B., Sørensen, K., Foged, N. & Vignoli, G., 2014. An overview of a highly versatile forward and stable inverse algorithm for airborne, ground-based and borehole electromagnetic and electric data. *Exploration Geophysics*, 46(3), pp.223–235.

Auken, E., Viezzoli, A. & Christiansen, A.V., 2009. A singlesoftware for processing, inverting, and presentation of AEM data of different system: The Aarhus Workbench. In *Australian Society of Exploration Geophysics Geophysicist (ASEG) 2009, Sydney, Australia, Expanded Abstract, 1-5*.

Bertin, J. & Loeb, J., 1976. *Experimental and Theoretical Aspects of Induced Polarization*, Berlin Stuttgart: Gebrüder Borntraeger.

Carroll, D., 1958. Role of clay minerals in the transportation of iron. *Geochimica et Cosmochimica Acta*, 14, pp.1–28.

Cavinato, G. P., Di Luzio, E., Moscatelli, M., Vallone, R., Averardi, M., Valente, A., & Papale, S., 2006. The new Col di Tenda tunnel between Italy and France: Integrated geological investigations and geophysical prospections for preliminary studies on the Italian side. *Engineering Geology*, 88(1), pp.90–109.

Christensen, W.K., 1984. The Albian to Maastrichtian of Southern Sweden and Bornholm, Denmark: a Review. *Cretatceous Research*, 5, pp.313–327.

Dahlin, T. & Leroux, V., 2012. Improvement in time-domain induced polarization data quality with multi-electrode systems by separating current and potential cables. *Near Surface Geophysics*, 10, pp.545–565.

Dahlin, T. & Zhou, B., 2004. A numerical comparison of 2D resistivity imaging with 10 electrode arrays. *Geophysical Prospecting*, 52(5), pp.379–398.

Danielsen, B.E. & Dahlin, T., 2009. Comparison of geoelectrical imaging and tunnel documentation at the Hallandsås Tunnel, Sweden. *Engineering Geology*, 107(3-4), pp.118–129.

Dunham, R.J., 1962. Classification of carbonate rocks according to texture. *Classification of carbonate rocks*, 1, pp.108–121.

Fanning, D.S., 1989. Oxidation State of Iron in Glauconite from Oxidized and Reduced Zones of Soil-Geologic Columns. *Clays and Clay Minerals*, 37(1), pp.59–64.

Fiandaca, G. et al., 2013. Resolving spectral information from time domain induced polarization data through 2-D inversion. *Geophysical Journal International*, 192(2), pp.631–646.

Fiandaca, G., Auken, E., Christiansen, A. V., & Gazoty, A., 2012. Time-domain-induced polarization: Full-decay forward modeling and 1D laterally constrained inversion of Cole-Cole parameters. *Geophysics*, 77(3), pp.E213–E225.

Fiandaca, G., Ramm, J., Binley, A., Gazoty, A., Christiansen, A. V., & Auken, E., 2015. Depth of Investigation for Multi-parameters Inversions. *Proc. Near Surface Geoscience 2015, 21st European Meeting of Environmental and Engineering Geophysics, Turin, Italy.*

Ganerød, G. V., Rønning, J. S., Dalsegg, E., Elvebakk, H., Holmøy, K., Nilsen, B., & Braathen, A., 2006. Comparison of geophysical methods for sub-surface mapping of faults and fracture zones in a section of the Viggja road tunnel, Norway. *Bulletin of Engineering Geology and the Environment*, 65(3), pp.231–243.

Gélis, C., Revil, a., Cushing, M. E., Jougnot, D., Lemeille, F., Cabrera, J., De Hoyos, A. & Rocher, M., 2010. Potential of electrical resistivity tomography to detect fault zones in limestone and argillaceous formations in the experimental platform of Tournemire, France. *Pure and Applied Geophysics*, 167(11), pp.1405–1418.

Ghorbani, A., Cosenza, P., Revil, a., Zamora, M., Schmutz, M., Florsch, N., & Jougnot, D., 2009. Non-invasive monitoring of water content and textural changes in clay-rocks using spectral induced polarization: A laboratory investigation. *Applied Clay Science*, 43(3-4), pp.493–502.

Houssaye, A., Lindgren, J., Pellegrini, R., Lee, A. H., Germain, D., & Polcyn, M. J., 2013. Microanatomical and Histological Features in the Long Bones of Mosasaurine Mosasaurs (Reptilia, Squamata) - Implications for Aquatic Adaptation and Growth Rates. *PLoS ONE*, 8(10), pp.1–12.

Johansson, S., Fiandaca, G. & Dahlin, T., 2015. Influence of non-aqueous phase liquid configuration on induced polarization parameters: Conceptual models applied to a time-domain field case study. *Journal of Applied Geophysics*, 123, pp.295–309.

Kemna, A., Binley, A., Cassiani, G., Niederleithinger, E., Revil, A., Slater, L., Williams, K.H., Flores Orozco, A., Haegel, F.-H., Hördt, A., Kruschwitz, S., Leroux, V., Titov, K &Zimmermann, E. (2012). An overview of the spectral induced polarization method for near-surface applications., 2012. An overview of the spectral induced polarization method for near-surface applications. *Near Surface Geophysics*, 10, pp.453–468.

Kornfält, K.-A., Bergström, J., Carserud, L., Henkel, H., & Sundquist, B., 1978. Description to the map of solid rocks and the aeromagnetic map Kristianstad SO. In *Swedish Geological Survey*.

Magnusson, M.K., Fernlund, J.M.R. & Dahlin, T., 2010. Geoelectrical imaging in the interpretation of geological conditions affecting quarry operations. *Bulletin of Engineering Geology and the Environment*, 69(3), pp.465–486.

Marescot, L., Monnet, R. & Chapellier, D., 2008. Resistivity and induced polarization surveys for slope instability studies in the Swiss Alps. *Engineering Geology*, 98(1-2), pp.18–28.

McRae, S.G., 1972. Glauconite. *Earth-Science Reviews*, 8(4), pp.397–440.

Okay, G., Cosenza, P., Ghorbani, A., Camerlynck, C., Cabrera, J., Florsch, N., & Revil, A., 2013. Localization and characterization of cracks in clay-rocks using frequency and time-domain induced polarization. *Geophysical Prospecting*, 61(1), pp.134–152.

Olsson, P. I., Fiandaca, G., Dahlin, T., & Auken, E., 2015. Impact of Time-domain IP Pulse Length on Measured Data and Inverted Models. *Proc. Near Surface Geoscience 2015, 21st European Meeting of Environmental and Engineering Geophysics, Turin, Italy.*

Olsson, P.-I., Fiandaca, G., Larsen, J. J., Dahlin, T., & Auken, E. (2016). Doubling the spectrum of time-domain induced polarization: removal of non-linear self-potential drift, harmonic noise and spikes, tapered gating, and uncertainty estimation. *Submitted for publication (Geophysical Journal International)*.

Park, M. K., Park, S., Yi, M. J., Kim, C., Son, J. S., Kim, J. H., & Abraham, A. A., 2014. Application of electrical resistivity tomography (ERT) technique to detect underground cavities in a karst area of South Korea. *Environmental Earth Sciences*, 71, pp.2797–2806.

Pelton, W. H., Ward, S. H., Hallof, P. G., Sill, W. R., & Nelson, P. H., 1978. Mineral discrimination and removal of inductive coupling with multifrequency IP. *Geophysics*, 43(3), pp.588–609.

Sengwa, R.J. & Soni, A., 2006. Low-frequency dielectric dispersion and microwave dielectric properties of dry and water-saturated limestones of the Jodhpur region. *Geophysics*, 71(5), pp.G269–G277.

Slater, L. & Lesmes, D.P., 2002a. Electrical-hydraulic relationships observed for unconsolidated sediments. *Water Resources Research*, 38(10), pp.1–13.

Slater, L.D. & Lesmes, D., 2002b. IP interpretation in environmental investigations. *Geophysics*, 67(1), p.77.

Tannhauser, D.S., 1962. Conductivity in iron oxides. *Journal of Physics and Chemistry of Solids*, 23(1-2), pp.25–34.

Thompson, G.R. & Hower, J., 1975. The mineralogy of glauconite. *Clays and Clay Minerals*, 23(4), pp.289–300.

Titov, K., Kemna, A., Tarasov, A., & Vereecken, H., 2004. Induced Polarization of Unsaturated Sands Determined through Time Domain Measurements. *Vadose Zone Journal*, 3(4), pp.1160–1168.

Vella, L. & Emerson, D., 2012. Electrical Properties of Magnetite- and Hematite-Rich Rocks and Ores. *Proc. 22nd*

ASEG Conference & Exhibition.

Zhang, C., Slater, L., Redden, G., Fujita, Y., Johnson, T., & Fox, D., 2012. Spectral induced polarization signatures of hydroxide adsorption and mineral precipitation in porous media. *Environmental Science and Technology*, 46(8), pp.4357–4364.